MOLECULAR DYNAMICS AND ESR SPECTRA OF A NITROXIDE SPIN LABEL AT SOLVENT-EXPOSED SURFACE SITES IN PROTEINS

A Dissertation

Presented to the Faculty of the Graduate School

of Cornell University

in Partial Fulfillment of the Requirements for the Degree of

Doctor of Philosophy

by

Deniz Sezer

January 2008

MOLECULAR DYNAMICS AND ESR SPECTRA OF A NITROXIDE SPIN LABEL AT SOLVENT-EXPOSED SURFACE SITES IN PROTEINS

Deniz Sezer, Ph.D.

Cornell University 2008

Using atomistic molecular dynamics (MD) simulations in the interpretation of multifrequency electron spin resonance (ESR) spectra is desirable but challenging. In this thesis, some of the conceptual and computational tools that are required to rigorously pursue this task are developed and applied. First, an efficient numerical scheme for simulating ESR spectra in the time domain is established, followed by an exact and efficient integrator for an anisotropic, restricted, rotational Brownian diffusion. These two integrators provide a flexible structure that can easily incorporate additional dynamics coming from MD trajectories or other stochastic models of motion. Second, force field parameters for nitroxide spin labels are developed and critically evaluated against *ab initio* calculations. Third, the spin label MTSSL, most widely used in studies of proteins, is simulated on a solvated poly-alanine alpha helix, to gain insight into its conformational dynamics at solvent exposed helix sites in proteins. Fourth, a systematic framework for constructing discrete-state Markov jump models of the internal spin label dynamics from many, relatively short MD trajectories is developed in the context of MTSSL on the poly-alanine helix. Finally, MTSSL is simulated at several solvent-exposed sites on the protein T4 Lysozyme. The simulations reveal extensive interactions of the spin label with the local protein environment, which significantly affect the ordering and dynamics of the spin label. Spectra at three different magnetic field strengths, calculated from the MD trajectories, show remarkable agreement with experiment.

BIOGRAPHICAL SKETCH

Deniz was born in Razgrad, Bulgaria in 1976. His family emigrated to Turkey in 1989, where they settled in Istanbul. He came to the States for a Ph.D. in 2000, and spent two and a half years in Ithaca, two and a half years in New York City, and two years in Chicago. He is going to Frankfurt for a postdoc.

Derin'e.

На майка, тако и кака.

ACKNOWLEDGEMENTS

This thesis comes at the end of a long Ph.D. during which many people have supported me in one way or another. Since mentioning each individual is going to be a formidable task, I would like to explicitly name only some and thank all the others for being there to chat over beer, lunch or dinner, for discussing science, for listening about my frustrations or telling me about theirs. To facilitate my navigation among all the names, I start with my stay in Ithaca and then proceed to my years in New York City and Chicago.

In Ithaca I felt an organic part of two overlapping communities: the Turkish students, with whom I interacted on a regular basis, and my fellow physics students. I am grateful to Aycan Yurtsever, Ömer Ilday, Hande Üstünel, Özhan Özatay and Taner Akgün for offering a caring friendship, who made my acclimatization to the US much smoother and less painful. Saswat Sarangi and Saikat Gosh were great friends, who were always ready to talk about anything deep (including physics), and to have fun (sometimes too crazy for my liking). Special thanks go to Gerod S. Hall, with whom I shared an apartment during all of the time I was in Ithaca. I consider myself lucky to have met a person as open and sincere as him upon my arrival to Ithaca.

From the professors in the Physics Department, Carl Franck was a great advisor during my years in Ithaca. He was very empathetic when I expressed interest in taking classes about the history/sociology of science. He made sure that I met the requirements in physics but never treated me as academically worthless just because my interest was not properly restricted to physics. Later, when I was moving to the Medical School of Cornell in New York City, he was not only extremely supportive and encouraging but very efficient in putting the right kind of pressure to make sure that I was going to be properly taken care of. I would also

like to acknowledge Piet Brouwer for playing a crucial role in the later formation of my scientific interests. After taking his class Solid State Physics II, I expressed interest in joining his lab and working with him. After considering the issue for six months, and waiting to see my performance in Solid State Physics I, he informed me that he can not take me as his student. Of course, it is impossible to know exactly what my weak points were (since I did well in both of the Solid State classes), but I suspect that having taken the classes in history/sociology of science did not help. For me, this rejection served as a turning point, since it motivated me to look for an advisor beyond the boundaries of the Physics Department. At this point, being in a place like Cornell, which houses scientific research in many diverse areas, helped tremendously. Shortly after I expanded my search, I joined the lab of David Shalloway at the Department of Molecular Biology and Genetics. Without doubt, I can say that David Shalloway was the most important person responsible for awakening my interest in computational biophysics and physical chemistry. His work was a wonderful introduction to the Smoluchowski equation and the statistical mechanics of protein folding. In addition, he made sure that I took the undergraduate Biochemistry class from Jerry Feigenson, who was an amazing teacher.

In New York I felt very isolated scientifically. As a physics student (who had taken only two classes in biochemistry) I was out of place in a medical school. There was no one with whom I could discuss the day-to-day details of my project, especially since I did not do any MD simulations during the first year or so. The frustration and stagnation I experienced with my project all those years in New York, was compensated by the excitement of living in Manhattan. For more than half of the time I lived on the Upper East Side I shared an apartment with Guillaume Lamoreux. Always calm, accommodating and understanding, he was a per-

fect flatmate. In the lab, I was extremely fortunate to share the same office with Janice Robertson and Marta Murcia, the two most caring lab members. Talking to them made the days of sitting and staring at the computer screen much more tolerable. Later, when everybody in the lab moved to the same room, in addition to Janice and Marta I started bothering Vishwanath Jogini and Yanxiang Zhao on a regular basis. My New York experience would have been completely different without the lunches at the Rockefeller University with Ali O. Güre, who has been a great friend, always ready to listen to my problems and excitements.

I would imagine that I benefited from moving to the University of Chicago more than anybody else in the group. No matter how unpleasant it was to move to Hyde Park from Manhattan, the school-neighborhood-weather combination at the U of C was perfect for getting the job done and finishing the Ph.D. Even more important was the presence of Albert C. Pan, who joined the group at this time. For the first time, there was a person in the group with whom I was able to discuss all the technicalities of my project and who, very nicely and systematically, exposed me to new and exciting aspects of theoretical physical chemistry. For me it was a very painful loss when Albert and I practically stopped talking, as a result of me becoming a second author in his string paper. It was a great pleasure to discuss things scientific and nonscientific with José Faraldo Goméz and Janice Robertson, the two people who, I think, made most of the effort to keep the lab cohesive. I also learned a lot by talking to Ed Harder and Bernhard Egwolf.

During the last 4.5 years of my Ph.D. my scientific experience was dominated by my interaction with my advisor Benoît Roux. I am grateful to him for bringing together an exceptionally good group of people and for giving me the chance to be a part of this group. It is due to him that I never felt the shortage of technical and financial resources and had infinite time at my disposal to explore any topic

I was interested in. The opportunity to observe him at the center of an exciting scientific subfield taught me a great deal about the tacit aspects of science. Crucial for the last year or so of my Ph.D. was the active involvement of Jack H. Freed with my project. I am tremendously grateful to him not only for his scientific input to the work reported in this thesis, but also for exposing me to the broader ESR community and seamlessly helping me to establish interactions with other people in the field. I would also like to thank the chair of my committee Tomás Arias, for his sincere interest in my work and for his encouragement and availability during the last months of my Ph.D. when I started planning my defense.

For me, the Ph.D. process has been a period during which personal and family life has been largely compromised. It is impossible to articulate my gratitude to my families (both unchosen and created) for their support and encouragement during all those years. In 7.5 years, their faith in me was gradually replaced by increasing frustration, but not at the expense of their love. To them I dedicate this thesis, hoping to manifest a tiny part of my thankfulness: To my parents and sister, who have always been there for me, and to my wife, who not only helped me grow up, but who has been bringing up our son all by herself.

TABLE OF CONTENTS

LIST OF TABLES

LIST OF FIGURES

CHAPTER 1

INTRODUCTION AND OVERVIEW OF THE THESIS

1.1 The nitroxide spin label as a biophysical reporter

Understanding how proteins perform their function in atomistic detail is one of the greatest challenges currently facing biological and physical scientists. Tremendous advance has already been achieved over the last half a century by determining tens of thousands of protein structures at atomic resolution. At the same time, it is well appreciated that dynamical excursions away from the static structures are necessary for proper protein function. Biophysical techniques capable of probing not only the structural characteristics but also the dynamics of proteins are, therefore, indispensable. Many such techniques, based on different physico-chemical principles, exist. Some of them utilize mechanical means to interact with the biomolecule of interset, e.g. atomic force microscopy and its variants, others rely on the interaction of matter with electromagnetic waves, e.g. nuclear magnetic resonance (NMR), electron spin resonance (ESR), fluorescence, and other ensemble- or single-molecule-based spectroscopic methods. Certainly, the method of choice depends on the nature of the system under examination. In the studies of protein function, taking place at physiological temperature in solvated, heterogeneous environements, spectroscopic methods might have some advantage over the more invasive mechanical ones.

In general, to interact with the molecular system spectroscopically a reporter group has to be chemically attached to it. Nitroxide spin labels, which contain an unpaired electronic spin, and chromofores, the electrons of which can be excited to higher energy leves, are two examples of reporters used in ESR and flourescence,

respectively. It is not necessary to introduce additional chemical groups in NMR, since the nuclear spins of the atoms themselves serve as reporters. Employing a molecule distinct from the protein as a reporter has its advantages and disadvantages. Whereas in NMR all the hydrogen nuclei in the protein, for example, contribute to the measured signal, there are usually only one or a few reporters per protein in ESR and flourescence, making them applicable independently of the size of the protein. In addition, the signal from the reporter is spatially localized, which, in principle, can be used to study the local protein dynamics. Unfortunately, the molecular reporter usually has its own conformational freedom and dynamics, the effect of which has to be filtered out from the signal. Compared to fluorescence, ESR benefits from utilizing relatively small spin labels as reporters. When chemically attached to a cysteine, the nitroxide spin label MTSSL, most commonly employed in studies of proteins, forms the "side chain" R1, which is somewhat bigger than the side chains of the naturally occuring amino acids arginine and trytophan.

When used with extensive site-directed spin lableing (SDSL) [26, 41, 58], ESR can provide rich information about the spin labeled protein of interest: The full breadth of the spectrum and the peak-to-peak width of the central line are directly correlated with the mobility of the spin label, allowing one to easily recognize sites in which the spin label is burried or exposed. The variation of these features as a function of the position of the spin label along the protein sequence can, therefore, be used to infer secondary structure—periodicity of 2 indicates a β-sheet, whereas periodicity of 3-4 signifies an α-helix. The recovery of the ESR signal from saturation can be used to measure the exposure of the spin label to either water- or lipid-soluble paramagnetic species, thus, one can determine how proteins, or their functional parts, are positioned in a lipid bilayer [29, 104]. The paramagnetic

coupling of two spin labels can be used to measure the distance between their unpaired electrons in the range of 10 to 70 Å [12,15–17], providing crucial distance constraints necessary for the structural determination of proteins that are hard to crystalize or too large for their structure to be solved with NMR. The variation of all these signals upon changing the environment of the protein (e.g. changing the temperature or the pH, applying a voltage or introducing a ligand) can be used to identify and study the response of the protein to external stimuli [57,104,132]. As evident from the cited references, SDSL has been sucessfully employed to study a wide variety of proteins, including membrane proteins, like ion channels [29, 104, 132] and transporters [26,41,57], which function in the heterogeneous environment of the cell membrane.

In spite of the enormous insight one can gain from comparing the ESR spectra from many different sites in the protein, under several different experimental conditions, the interpretation of the individual spectra in terms of the conformation and dynamics of the spin labeled protein remains largely qualitative. Oftentimes, the proposed connection between certain features of a given spectrum and the atomic interactions and dynamics causing them is based on intuition and previous experience rather than on complete understanding of the causal link. The reason is that it is impossible to perform some sort of an "inverse transformation" on the ESR spectrum, which will automatically yield the structural and dynamical features of the spin label and its local molecular environment. A practical alternative is to address the problem in reverse: Starting with a physically motivated model of the classical spin label dynamics and calculating spectra from this model, is it possible to reproduce the experimental spectra? In case of success, one can attempt to establish a connection between the parameters of the model and the underlying molecular picture. Furthermore, the model and its parameters can be varied either

to improve the agreement between the calculated and experimantal specta or to assess the degree to which the spectra are sensitive to such changes.

The existing approaches for modeling the spin label dynamics can be grouped into two classes. The first category contains the phenomenological models in which the label is assumed to undergo Brownian rotational diffusion. In the most general case the rotational diffusion can be anisotropic (i.e. the diffusion tensor is symmetric but anisotropic) and restricted (i.e. there is an underlying potential energy which favors certain orientations and penalizes others). The only, major constraint of such models is their analytical or numerical tractability. The second class of models are based on a completely different philosophy. Rather than postulating a phenomenological diffusive dynamics for the spin label, its dynamics are simulated using a classical, molecular-mechanics force field. For spin labels at protein-surface sites, which, potentially, may interact with the rugged protein surface, these models are expected to provide a more realistic picture of the non-trivial protein and solvent environment.

1.2 Synopsis of the chapters

The scope of this disertation is limited to nitroxide free radicals, which are extensively used as spin labels in studies of proteins [13, 57], lipids [13] and nucleic acids [116]. More specifically, the conformational dynamics of the spin label side chain R1 is studied at several slovent-exposed sites on the surface of the protein T4 Lysozyme, by performing MD simulations with the CHARMM molecular mechanics force field. As a stringent check of the fidelity of the simulations, multifrequency ESR spectra are calculated using the simulated spin label dynamics and compared

Table 1.1: Methodological developments listed according to the chapter in which they are first developed. The checkmarks indicate their usage in later chapters. In parenthesis are the systems for which MD simulations are performed.

Ch. 2	Ch. 3	Ch. 4	Ch. 5
Integrators	✓	✓	✓
	Force field parameters		✓
	(poly-alanine α-helix)	✓	
		Markov chain analysis	✓
			(T4 Lysozyme)

with the available experimental spectra. The MD simulations of R1 at several sites on T4 Lysozyme, together with the analysis of the spin label dynamics and the calculations of the resulting ESR spectra are presented in Ch. 5. In the three chapters preceeding it, namely Chs. 2, 3 and 4, the required computational tools are developed, as summarized in Table 1.1. Somewhat more detail is provided in the following overviews.

Ch. 2: Numerical integrators

Simulating electron spin resonance spectra of nitroxide spin labels from models of their motion is necessary for the quantitative analysis of experimental spectra. We present a framework for modeling the spin label dynamics by combining trajectories, such as those from molecular dynamics (MD) simulations with stochastic treatment of the global protein tumbling. This is achieved in the time domain after two efficient numerical integrators are developed: one for the quantal dynamics of the spins, the other for the classical rotational diffusion. In the former, we

propagate the relevant part of the spin density matrix in Hilbert space. Working with quaternions in the latter, we are able to treat anisotropic diffusion in a potential expanded as a sum of spherical harmonics. Time-averaging arguments are invoked to bridge the gap between the smaller time step of the MD trajectories and the larger time steps appropriate for the rotational diffusion and/or quantal spin dynamics.

Ch. 3: Force field parameters and MD simulations of a spin label on a poly-alanine α-helix

The nitroxide spin label MTSSL, commonly used in SDSL of proteins, is studied by performing MD simulations. After developing force field parameters for the nitroxide moiety and the spin label linker, we simulate MTSSL on a poly-alanine α-helix in explicit solvent to elucidate the factors affecting its conformational dynamics at solvent-exposed sites on the surface of α-helices. ESR spectra at 9 and 250 GHz are simulated in the time domain using the MD trajectories and including global rotational diffusion appropriate for the tumbling of T4 Lysozyme in water. Analysis of the MD simulations reveals the presence of significant hydrophobic interactions of the spin label with the alanine side chains.

Ch. 4: Building Markov chain models of the spin label dynamics from the MD trajectories

Simulating ESR spectra directly from trajectories of the spin label dynamics necessitates many (hundreds or thousands), relatively long (hundreds of ns) trajectories. To meet the challenge of using all-atom MD simulations of spin labeled proteins in the interpretation of their spectra, we explore the possibility of con-

structing stochastic models of the spin label dynamics from atomistic trajectories. A systematic, two-step procedure, based on the probabilistic framework of hidden Markov models, is developed to build a discrete-time Markov chain process that faithfully captures the internal dynamics of the spin label on time scales longer than about 150 ps. The constructed Markov jump model is used both to gain insight into the long-lived conformations of the spin label and to generate as many and as long stochastic trajectories as necessary for the simulation of ESR spectra.

Ch. 5: Spin label dynamics and ESR spectra of solvent-exposed sites in T4 Lysozyme

Multifrequency electron spin resonance (ESR) spectra contain extremely rich information about the structure and dynamics of the local environment of the spin label (SL). Relating the features of the spectra to the molecular motion and interactions that cause them has proven to be rather challenging. Extensive molecular dynamics simulations of fully solvated T4 Lysozyme, spin labeled at positions 72, 131 and 82, are performed. The atomistic trajectories are utilized to construct stochastic Markov chain models of the internal SL dynamics. Combined with stochastic treatment of the global protein tumbling, the Markov jump trajectories are used to simulate multifrequency ESR spectra in quantitative agreement with experiment. The conformations of the most probable Markov states and the energies of their interaction with the protein surface are examined to gain insight into the behavior of the SL at solvent-exposed surface sites in proteins.

CHAPTER 2

SIMULATING ESR SPECTRA OF NITROXIDE SPIN LABELS FROM MD AND STOCHASTIC TRAJECTORIES

2.1 Introduction

Nitroxide spin labels are extensively used in electron spin resonance (ESR) studies of proteins [13, 57], nucleic acids [116] and lipid bilayers [13]. The ability to simulate ESR spectra from models of the spin label dynamics is indispensable for the quantitative analysis and interpretation of experimental spectra. Conceptually, the problem can be divided into two complementary parts: classical and quantum. The dynamics of the coupled electronic-nuclear spin system necessitates quantum mechanical treatment, whereas the rotational dynamics of the spin label can be treated classically. The choice of the (stochastic) model for the classical motion determines the time-dependence of the spin Hamiltonian. The latter is used to calculate the relaxation of the transverse magnetization. As usual when dealing with dynamical stochastic processes, it is possible to work either directly with the probability density, or with explicit realizations of the process (trajectories). In the former case the coupled classical-quantum evolution is described by the stochastic Liouville equation (SLE) due to Kubo [74–76]. This approach constitutes the basis of the sophisticated theory and spectral simulation/fitting software developed by Freed and co-workers over the last four decades [18, 46, 80, 94, 106–108]. In this chapter, we pursue the second alternative and work with dynamical trajectories.

While the idea of using trajectories to simulate ESR spectra is not new [101, 117, 120], it has become increasingly attractive for two main reasons. On the one hand, it is feasible to generate trajectories for more complicated stochas-

tic models than can readily be handled with the SLE formalism. This has been suggested by Westlund and co-workers [53,105], although they employ models still tractable with the SLE [80,106,107]. On the other hand, it is possible to simulate spectra directly from molecular dynamics (MD) trajectories [7, 39, 54, 133, 134], without postulating any stochastic model. The prospect of using atomically detailed MD trajectories to simulate ESR spectra is even more attractive with the recent development of high-field ESR [45]. Increased sensitivity to dynamics on a subnanosecond time scale at high fields holds the promise of establishing a tighter connection between MD simulations and experimental spectra, hopefully resulting in the detailed interpretation of the latter and more stringent validation of the former.

A major challenge to this effort is that many, long trajectories, far beyond what can be routinely achieved with straightforward MD, are necessary for the convergence of the spectra [40, 54, 117, 134]. As an alternative, MD trajectories can be used to estimate the parameters of a pre-selected Markovian model [7,19,133]. ESR spectra are then calculated by either solving the SLE [19] or generating trajectories [7,133] for the model. In principle, once the stochastic model and its parameters are established, either the SLE approach or the trajectory-based approach are applicable. In practice, spectra from more sophisticated rotational dynamics models like MOMD and SRLS, developed within the SLE formalism [80, 94, 106, 107], have not been simulated using the trajectory-based approach. Previous work in which rotational diffusion trajectories were employed to simulate ESR spectra was restricted to free isotropic diffusion [101, 117] or isotropic diffusion in a cone [42]. The lack of a rigorous formalism to simulate trajectories for anisotropic diffusion in a potential has prevented the trajectory-based approach to be exploited to its fullest.

Here we address two separate questions pertaining to the simulation of ESR spectra from trajectories: First, what is the most efficient and rigorous way of propagating the quantal spin dynamics and calculating the transverse magnetization, given as many and as long trajectories as necessary? Several quantum integrators achieving this have already been proposed in the literature [40, 133, 139]. They range from the *ad hoc* manipulation of the eigenvalues of the instantaneous Hamiltonian [133] (disregarding the eigenvectors), to the rigorous propagation of the state vector in Hilbert space [40] or the density matrix in Liouville space [139]. We show that, once the high-field approximation is introduced, the most efficient choice is to propagate the density matrix in Hilbert space. Second, how can MD trajectories, necessarily missing information about the global macromolecular dynamics, be utilized in a meaningful way to simulate experimentally relevant ESR spectra? We propose to use the MD trajectories in combination with trajectories from stochastic models, which can account for the dynamical events that are poorly sampled in the MD simulations, such as the tumbling of the spin labeled macromolecule. This raises two additional questions: How to simulate trajectories of sophisticated rotational diffusion models like MOMD and SRLS? How to bridge the gap between the small time step at which the MD snapshots are available and the longer time steps appropriate for the numerical propagation of the stochastic or quantal dynamics?

The chapter is organized as follows: Quantal spin dynamics and classical anisotropic Brownian diffusion in a potential are the subject of Sec. 2.2. The former is reviewed in Sec. 2.2.1, in which we illustrate how to numerically propagate the relevant part of the density matrix in Hilbert space. The latter is developed in Sec. 2.2.2, in which an accurate and efficient numerical integrator for this general rotational diffusion model is presented. Lastly, spectra for free and restricted ro-

tational diffusion models simulated using the developed time-domain integrators and the SLE are compared. Section 2.3 contains our proposal for combining MD and stochastic trajectories. Time-averaging arguments are invoked to bridge the gap between the various integration time steps. Multifrequency spectra simulated using a combination of rotational diffusion/MD trajectories are presented. A concluding discussion is given in Sec. 2.4. Further detail about some expressions used in the numerical work is provided in Sec. 2.5.

2.2 Numerical integrators

2.2.1 Integrating the quantal spin dynamics

The formal equivalence between continuous-wave (cw) and free induction decay (FID) spectra [1] is exploited to simulate the latter instead of the former. The efficient numerical simulation of FID ESR spectra is addressed after reviewing the relevant theoretical background.

The spin Hamiltonian and the interaction picture

A nitroxide has an unpaired electron with spin $\hat{\boldsymbol{S}}$ ($S = \frac{1}{2}$) and an ^{14}N nucleus with nuclear spin $\hat{\boldsymbol{I}}$ ($I = 1$). (Throughout, bold letters are used to denote vectors in physical space, Hilbert space operators are indicated with a caret.) The spin Hamiltonian of a nitroxide, in units of angular frequency, is

$$\hat{H}(t) = \gamma_{\mathrm{e}}\Big(\boldsymbol{B}\cdot\mathsf{G}(t)\cdot\hat{\boldsymbol{S}} + \hat{\boldsymbol{I}}\cdot\mathsf{A}(t)\cdot\hat{\boldsymbol{S}}\Big), \tag{2.1}$$

where γ_e is the electronic gyromagnetic ratio, A is the hyperfine tensor (expressed in units of magnetic field) and

$$\mathsf{G}(t) \equiv \mathsf{g}(t)/g_e \tag{2.2}$$

is the electronic g-tensor $\mathsf{g}(t)$ divided by the free electron g-factor g_e. The coupling tensors G and A are typically diagonal in the same coordinate frame $\mathtt{N}$, attached to the nitroxide. Their explicit time dependence in Eq. (2.1) is due to the dynamics of this frame with respect to the stationary laboratory frame $\mathtt{L}$, in which the external magnetic field $\boldsymbol{B} = (0, 0, B_0)$ is applied. All the vector and tensor components in Eq. (2.1) are with respect to $\mathtt{L}$. The nuclear Zeeman as well as the quadrupolar interactions are typically neglected, but they can be included in the methodology described below, when needed.

We denote the quantal state of the electronic and nuclear spins localized on a single spin label by $|\psi(t)\rangle$. The dynamics of this state vector are governed by the spin Hamiltonian through the Schrödinger equation. Let us write the Hamiltonian from Eq. (2.1) in the form

$$\hat{H}(t) = \hat{H} + \hat{V}(t), \tag{2.3}$$

where the first part

$$\hat{H} \equiv \gamma_e G_0 B_0 \hat{S}_z = \omega_0 \hat{S}_z, \tag{2.4}$$

with

$$G_0 \equiv \frac{1}{3}\mathrm{Tr}\{\mathsf{G}\}, \tag{2.5}$$

isolates a large but constant portion of $\hat{H}(t)$. The remaining time-dependent part is contained in $\hat{V}(t)$. In the absence of $\hat{V}(t)$, the state vector oscillates at the Larmor precession frequency ω_0. In its presence, the instantaneous frequency of precession varies around ω_0 by a time-dependent modulation, which is typically much smaller than ω_0.

Explicit treatment of the Larmor precession is inconvenient when the quantum dynamics are integrated numerically, since resolving the fast oscillations requires the use of a small integration time step. This difficulty is readily dealt with by transforming to a coordinate frame rotating at the Larmor frequency (i.e. the interaction picture). In the interaction picture, where

$$|\psi'(t)\rangle \equiv \mathrm{e}^{\mathrm{i}\hat{H}t}|\psi(t)\rangle, \qquad \hat{V}'(t) \equiv \mathrm{e}^{\mathrm{i}\hat{H}t}\hat{V}(t)\mathrm{e}^{-\mathrm{i}\hat{H}t}, \tag{2.6}$$

the Schrödinger equation is

$$|\dot{\psi}'(t)\rangle = -\mathrm{i}\hat{V}'(t)|\psi'(t)\rangle. \tag{2.7}$$

Using the relations

$$\hat{S}'_z = \hat{S}_z, \qquad \hat{S}'_+ = \hat{S}_+\mathrm{e}^{+\mathrm{i}\omega_0 t}, \qquad \hat{S}'_- = \hat{S}_-\mathrm{e}^{-\mathrm{i}\omega_0 t}, \tag{2.8}$$

the time-dependent part of the Hamiltonian in the interaction picture can be written as

$$\hat{V}'(t) = \hat{V}_z(t) + \sum_{\kappa=\pm} \hat{V}_\kappa(t)\mathrm{e}^{\mathrm{i}\kappa\omega_0 t}. \tag{2.9}$$

Here, the operators

$$\hat{V}_\nu(t) \equiv \big(b_\nu(t) + \hat{a}_\nu(t)\big)\hat{S}_\nu, \qquad \nu = z, \pm, \tag{2.10}$$

are defined in terms of the operators

$$\begin{aligned} \hat{a}_z(t) &\equiv \gamma_\mathrm{e} \sum_{i=x,y,z} A_{iz}(t)\hat{I}_i \\ \hat{a}_\pm(t) &\equiv \gamma_\mathrm{e} \sum_i \frac{1}{2}\big(A_{ix}(t) \mp \mathrm{i}A_{iy}(t)\big)\hat{I}_i, \end{aligned} \tag{2.11}$$

which act only on the nuclear spin state, and the scalars

$$\begin{aligned} b_z(t) &\equiv \gamma_\mathrm{e} B_0 G'_{zz}(t) \\ b_\pm(t) &\equiv \gamma_\mathrm{e} B_0 \frac{1}{2}\big(G'_{zx}(t) \mp \mathrm{i}G'_{zy}(t)\big), \end{aligned} \tag{2.12}$$

expressed in terms of the traceless tensor

$$\mathsf{G}'(t) \equiv \mathsf{G}(t) - G_0\mathsf{E}. \tag{2.13}$$

(Above, E denotes the identity matrix, to distinguish it from the nuclear spin operator $\hat{I}$.)

By going to the interaction picture the magnitude of the Hamiltonian has been decreased: $\hat{V}_\nu(t)$ are smaller than $\hat{H}(t)$. This leads to variation of $|\psi'(t)\rangle$ on a time scale that is usually longer than the Larmor precession time scale, allowing for the use of a larger integration time step. At the same time, in the rotating frame, parts of the Hamiltonian acquire fast oscillations at the Larmor frequency: the exponents $\mathrm{e}^{\mathrm{i}\kappa\omega_0 t}$ in Eq. (2.9). If the magnetic tensors $\mathsf{G}(t)$ and $\mathsf{A}(t)$, and thus the coefficients $\hat{V}_\nu(t)$, fluctuate on a time scale much slower than the Larmor precession time scale, then these fast fluctuations could average out the effect of the terms $\hat{V}_\pm(t)$. A slowly changing observable, like the transverse magnetization, can then be calculated by considering only the slowly varying part, $\hat{V}_z(t)$, of the Hamiltonian (2.9). This leads to the high-field approximation, to which we turn now.

The high-field approximation

Assume that the operators $\hat{V}_\nu(t)$ in Eq. (2.9) are slowly varying in comparison with the fast time scale of Larmor precession. In this section, we introduce the small parameter $\epsilon = 1/\omega_0$ and perform an expansion of the Schrödinger equation (2.7) in powers of ϵ. The high-field approximation is derived as the zeroth order term in the expansion. The first order term is analyzed to assess the range of validity of the approximation.

We seek a solution of Eq. (2.7) in the form

$$|\psi'(t)\rangle = |\psi^0(t)\rangle + \epsilon \sum_{\kappa=\pm} |\psi^\kappa(t)\rangle \mathrm{e}^{\mathrm{i}\kappa t/\epsilon}, \tag{2.14}$$

where $|\psi^0(t)\rangle$ and $|\psi^\kappa(t)\rangle$ are slowly varying. The goal is to derive an equation of motion for $|\psi^0(t)\rangle$, since the rest of the state vector is averaged out by the fast precession. Substituting Eqs. (2.14) and (2.9) into Eq. (2.7) leads to

$$\begin{aligned} &|\dot{\psi}^0(t)\rangle + \sum_{\kappa=\pm} \left(\epsilon|\dot{\psi}^\kappa(t)\rangle + \mathrm{i}\kappa|\psi^\kappa(t)\rangle\right) \mathrm{e}^{\mathrm{i}\kappa t/\epsilon} = \\ &-\mathrm{i}\hat{V}_z(t)|\psi^0(t)\rangle - \epsilon\mathrm{i} \sum_{\mu,\kappa=\pm} \hat{V}_{-\mu}(t)|\psi^\kappa(t)\rangle \mathrm{e}^{\mathrm{i}(\kappa-\mu)t/\epsilon} \\ &-\mathrm{i}\sum_{\kappa=\pm} \left(\hat{V}_\kappa(t)|\psi^0(t)\rangle - \epsilon\hat{V}_z(t)|\psi^\kappa(t)\rangle\right) \mathrm{e}^{\mathrm{i}\kappa t/\epsilon}, \end{aligned} \tag{2.15}$$

which contains slowly varying terms, proportional to $\mathrm{e}^{0t/\epsilon}$, and small terms, proportional to ϵ. Collecting the slowly varying terms only, which survive after time averaging, the desired slow equation of motion is obtained:

$$|\dot{\psi}^0(t)\rangle = -\mathrm{i}\hat{V}_z(t)|\psi^0(t)\rangle - \epsilon\mathrm{i}\sum_{\kappa=\pm} \hat{V}_{-\kappa}(t)|\psi^\kappa(t)\rangle. \tag{2.16}$$

This is an equation for $|\psi^0(t)\rangle$ but it depends on $|\psi^\kappa(t)\rangle$. Since the dependence on $|\psi^\kappa(t)\rangle$ is suppressed by the presence of ϵ, determining these functions to zeroth order in ϵ is enough to have an equation for $|\psi^0(t)\rangle$ correct to first order in ϵ. Matching the rapidly oscillating terms of order ϵ^0 on both sides of Eq. (2.15) yields

$$|\psi^\kappa(t)\rangle = -\frac{1}{\kappa}\hat{V}_\kappa(t)|\psi^0(t)\rangle, \tag{2.17}$$

to zeroth order in ϵ. Using this approximation in Eq. (2.16), leads to an equation for the slowly varying part of the state vector, correct to first order in ϵ:

$$|\dot{\psi}^0(t)\rangle = -\mathrm{i}\hat{H}_\mathrm{S}(t)|\psi^0(t)\rangle, \tag{2.18}$$

where the effective, slow Hamiltonian is

$$\hat{H}_\mathrm{S}(t) \equiv \hat{V}_z(t) + \epsilon[\hat{V}_+(t), \hat{V}_-(t)]. \tag{2.19}$$

The state vector is of interest only in the context of calculating expectations of Hilbert space operators. Therefore, before proceeding, it is important to check that the expectation values calculated using $|\psi^0(t)\rangle$ are correct to first order in ϵ up to time averaging. To first order, the expectation value of an operator $\hat{O}$ in the interaction picture is

$$\begin{aligned}\langle\psi'(t)|\hat{O}'|\psi'(t)\rangle = \langle\psi^0(t)|\hat{O}'|\psi^0(t)\rangle \\ + \epsilon\sum_{\kappa=\pm}\Big(\langle\psi^0(t)|\hat{O}'|\psi^\kappa(t)\rangle \mathrm{e}^{\mathrm{i}\kappa t/\epsilon} \\ + \langle\psi^\kappa(t)|\hat{O}'|\psi^0(t)\rangle \mathrm{e}^{-\mathrm{i}\kappa t/\epsilon}\Big),\end{aligned} \tag{2.20}$$

where Eq. (2.14) was used to write the right hand side of the equality. Indeed, the first order term is oscillatory and vanishes after time averaging, indicating that to this order $|\psi'\rangle$ and $|\psi^0\rangle$ are interchangeable.

Written explicitly, the slow Hamiltonian in Eq. (2.19) is

$$\begin{aligned}\hat{H}_{\mathrm{S}}(t) &= \big(b_z(t) + \hat{a}_z(t)\big)\hat{S}_z \\ &+ \frac{1}{\omega_0}\big(b_+(t)b_-(t) + b_+(t)\hat{a}_-(t) + b_-(t)\hat{a}_+(t)\big)\big[\hat{S}_+, \hat{S}_-\big] \\ &+ \frac{1}{\omega_0}\big(\hat{a}_+(t)\hat{a}_-(t)\hat{S}_+\hat{S}_- - \hat{a}_-(t)\hat{a}_+(t)\hat{S}_-\hat{S}_+\big).\end{aligned} \tag{2.21}$$

The perturbational terms in this expression are suppressed by $1/\omega_0$. To assess their magnitude let us look at some typical values for the nitroxide magnetic tensors:[1]

$$\begin{aligned}\mathsf{g}^{\mathtt{N}} &= \mathrm{diag}(2.00809, 2.00585, 2.00202) \\ \mathsf{A}^{\mathtt{N}} &= \mathrm{diag}(6.2, 4.3, 36.9)\ \mathrm{G}.\end{aligned} \tag{2.22}$$

Since the $b_\pm$ are proportional to the traceless part of g (cf. Eq. (2.12)), while its trace is proportional to ω_0, the second term on the right hand side of Eq. (2.21) is about a thousand times smaller than the first term. Similarly, the entries of A are on the order of 30 G while ω_0 (in units of G) is more than 3 KG at 9 GHz going

[1] Ziwei Zhang and Jack H. Freed, unpublished results.

up to 130 KG at 360 GHz (see Table 2.1), rendering the last term from a hundred to a few thousand times smaller than the first. Neglecting these latter terms and retaining only the $\hat{V}_z$ part of the Hamiltonian is therefore justified. This leads to the high-field approximation with effective Hamiltonian

$$\hat{H}_{\mathrm{HF}}(t) = \gamma_{\mathrm{e}}\big(B_0 G'_{zz}(t) + \hat{\boldsymbol{I}} \cdot \boldsymbol{a}(t)\big)\hat{S}_z, \tag{2.23}$$

where the components of the vector $\boldsymbol{a}$ are defined as

$$a_i(t) \equiv A_{iz}(t). \tag{2.24}$$

An equivalent form of Eq. (2.23) is the starting point for the SLE analysis of slow motion for the unsaturated line shapes [18, 46, 80, 94, 106–108].

The first order terms neglected when going from Eq. (2.21) to Eq. (2.23) correspond to double flips of the z-component of the electronic spin (as indicated by the presence of $\hat{S}_{\pm}\hat{S}_{\mp}$). Thus, what has been neglected is the contribution of spin flips to the decay of the transverse magnetization. Both the slow Hamiltonian (2.21) and its zeroth order approximation (2.23) are diagonal in the electronic Hilbert space and do not account for the possibility of spin flips. Because the equilibration of the longitudinal magnetization is entirely due to such spin flips, neither of these Hamiltonians can be used when phenomena leading to T_1 relaxation are of interest. In such cases, explicit treatment of the fast dynamics at the time scale of the Larmor precession is necessary.

As a result of the high-field approximation, the spin dynamics of the $m_S = \frac{1}{2}$ $(+)$ and $m_S = -\frac{1}{2}$ $(-)$ sectors of the Hilbert space decouple. This is clearly seen once the state vector

$$|\psi'(t)\rangle = \begin{pmatrix} |\psi'^{+}(t)\rangle \\ |\psi'^{-}(t)\rangle \end{pmatrix} \tag{2.25}$$

Table 2.1: Larmor precession frequencies, $f = \omega_e/2\pi$, and associated periods for various magnetic field strengths.

B_0 (T)	0.34	1.21	3.39	6.07	8.92	12.8
f (GHz)	9.5	34	95	170	250	360
T (ps)	100	30	10	6	4	3

and the Hamiltonian (2.23) are introduced in Eq. (2.18):

$$\begin{pmatrix} |\dot{\psi}'^{+}(t)\rangle \\ |\dot{\psi}'^{-}(t)\rangle \end{pmatrix} = -\mathrm{i} \begin{pmatrix} \hat{H}_{\mathrm{HF}}^{++}(t) & 0 \\ 0 & \hat{H}_{\mathrm{HF}}^{--}(t) \end{pmatrix} \begin{pmatrix} |\psi'^{+}(t)\rangle \\ |\psi'^{-}(t)\rangle \end{pmatrix}. \tag{2.26}$$

(The slow state vector $|\psi^0\rangle$ was replaced by the state vector in the interaction picture $|\psi'\rangle$.) Numerical integration of the quantum dynamics can therefore be achieved by separately updating the two parts $|\psi'^{\pm}\rangle$ of the state vector, according to the short-time propagation scheme

$$|\psi'^{\pm}(t + \Delta t)\rangle = \mathrm{e}^{\mp \mathrm{i}\Delta t \hat{H}_{\mathrm{HF}}^{++}(t)} |\psi'^{\pm}(t)\rangle, \tag{2.27}$$

where the equality $\hat{H}_{\mathrm{HF}}^{--} = -\hat{H}_{\mathrm{HF}}^{++}$, valid for the high-field Hamiltonian, was used.

The quantum integrator summarized by Eq. (2.27) is the one used by Eviatar and Levine [40]. Their vectors $\boldsymbol{P}$ and $\boldsymbol{Q}$ correspond to $|\psi'^{\pm}\rangle$.

The spectrum and the reduced density operator

The FID spectrum, which we aim to simulate, is the Fourier-Laplace transform of the transverse magnetization $M_+ = M_x + \mathrm{i}M_y$:

$$\tilde{M}_+(\omega) = \int_0^\infty \mathrm{e}^{-\mathrm{i}\omega t} M_+(t)\, \mathrm{d}t. \tag{2.28}$$

Here $M_+(t) = \langle \hat{M}_+(t) \rangle$ is the quantum mechanical expectation of the operator $\hat{M}_+ \propto \hat{S}_+$. (The proportionality constant is neglected, since the absolute value of the measured spectrum depends on the instrumental factors and is not very relevant.) Two consequences follow from the proportionality of $\hat{M}_+$ to $\hat{S}_+$. First, from Eq. (2.8), $M_+(t)$ satisfies

$$M_+(t) = \langle \psi'(t) | \hat{M}'_+ | \psi'(t) \rangle = \mathrm{e}^{\mathrm{i}\omega_0 t} \langle \psi'(t) | \hat{M}_+ | \psi'(t) \rangle. \tag{2.29}$$

Therefore, one can sandwich the operator $\hat{M}_+$ in the Schrödinger picture with the state vector in the interaction picture and simply shift the resulting spectrum by the Larmor frequency:

$$\tilde{M}_+(\omega + \omega_0) = \int_0^\infty \mathrm{e}^{-\mathrm{i}\omega t} \langle \psi'(t) | \hat{M}_+ | \psi'(t) \rangle \, \mathrm{d}t. \tag{2.30}$$

Second, since $\hat{S}_+$ is a raising operator, for the expectation in Eq. (2.30) one has

$$\langle \psi'(t) | \hat{M}_+ | \psi'(t) \rangle = \langle \psi'^{+}(t) | \hat{M}_+ | \psi'^{-}(t) \rangle. \tag{2.31}$$

This last equality motivates the introduction of the (reduced) density matrix

$$\rho'^{-+}(t) \equiv |\psi'^{-}(t)\rangle \langle \psi'^{+}(t)| \tag{2.32}$$

in terms of which

$$\langle \psi'(t) | \hat{M}_+ | \psi'(t) \rangle = \mathrm{Tr}\big\{ \hat{M}_+ \rho'^{-+}(t) \big\}. \tag{2.33}$$

In the high-field approximation, the dynamics of ρ'^{-+} are decoupled from the dynamics of the other sectors of the spin density matrix (ρ'^{++}, ρ'^{+-} and ρ'^{--}, defined analogously to Eq. (2.32)). From the propagation scheme in Eq. (2.27) and the definition of ρ'^{-+}, its short-time dynamics follow automatically:

$$\rho'^{-+}(t + \Delta t) = \mathrm{e}^{\mathrm{i}\Delta t \hat{H}^{++}_{\mathrm{HF}}(t)} \rho'^{-+}(t) \mathrm{e}^{\mathrm{i}\Delta t \hat{H}^{++}_{\mathrm{HF}}(t)}. \tag{2.34}$$

Note that the same matrix acts on both sides of ρ'^{-+} in this last equation, which is different from the propagation of the density matrix in the full Hilbert space.

Equation (2.34) forms the basis of our integrator for the (relevant sector) of the quantum spin dynamics. Its numerical efficiency depends on the possibility to rapidly calculate the matrix exponential

$$\mathrm{e}^{\mathrm{i}\Delta t\hat{H}_{\mathrm{S}}^{++}(t)} = \mathrm{e}^{\mathrm{i}\Delta t\frac{1}{2}\gamma_{\mathrm{e}}\left(B_0 G'_{zz}(t)+\boldsymbol{a}(t)\cdot\hat{\boldsymbol{I}}\right)} \tag{2.35}$$

at each time step. Since the first term in the parenthesis leads to a simple, time-dependent phase factor, the problem reduces to the evaluation of the matrix exponential due to the second term. Straightforwardly, this can be achieved by first diagonalizing the matrix $\boldsymbol{a}(t)\cdot\hat{\boldsymbol{I}}$ in the nuclear spin space with a similarity transformation, exponentiating its eigenvalues, and performing the similarity transformation in reverse. A more efficient alternative is possible due to the relation between the nuclear spin matrices and the three dimensional representation of the rotation group [2]. For the latter, it is known that the matrix

$$\hat{N} = \sum_i n_i \hat{I}_i, \tag{2.36}$$

where $\underline{\boldsymbol{n}} = (n_x, n_y, n_z)$ is a unit vector, satisfies

$$\mathrm{e}^{-\mathrm{i}\theta\hat{N}} = \hat{E}_I - \mathrm{i}(\sin\theta)\hat{N} - (1-\cos\theta)\hat{N}^2. \tag{2.37}$$

Here, to prevent confusion with the nuclear spin operator, $\hat{E}_I$ denotes the identity operator in the three dimensional Hilbert space of the nuclear spin. (Equation (2.37) can be easily verified using $\hat{N}^3 = -\hat{N}$.) As a result, solving the eigenvalue problem of $\boldsymbol{a}(t)\cdot\hat{\boldsymbol{I}}$ at each time step is avoided. Instead, the magnitude a and direction $\underline{\boldsymbol{n}}$ of the vector $\boldsymbol{a}(t)$ are calculated. The rotation angle $\theta = \gamma_{\mathrm{e}}\Delta t\frac{1}{2}a$ and the unit vector $\underline{\boldsymbol{n}}$ are used to construct the short-time propagator (2.37), as shown explicitly in Eq. (2.79).

At this stage, our choice to perform the quantum propagation using Eq. (2.34) instead of Eq. (2.27) seems to be largely a matter of taste since the same short-time propagator (2.35) needs to be calculated for both. In fact, when working with ρ'^{-+} one has to keep track of a 3×3 matrix, whereas only two 3×1 vectors are updated when working with $|\psi'^{\pm}\rangle$. The advantage of the density matrix becomes apparent when the initial conditions of the quantum process are considered. Since what is accessible experimentally is the initial value of the density operator, working with the state vector requires an additional averaging over all the possible state vectors that give the correct initial magnetization [38]. Only one initial condition for the state vector was chosen by Eviatar and Levine in Ref. [40], which was corrected in a later publication, where the entries of the starting state vector were generated randomly subject to a constraint [38]. The necessity to randomly vary the initial state vector and repeat the calculation disappears if one works with the density matrix.

At equilibrium, decoupled initial conditions can be assumed for the classical and quantal processes, thus $\rho(0) = \rho^{\mathrm{eq}}$, where the equilibrium density operator is given in terms of the average Hamiltonian:

$$\rho^{\mathrm{eq}} \propto \exp(-\hbar \bar{\hat{H}} / k_{\mathrm{B}} T). \tag{2.38}$$

(Here k_{B} is Boltzmann's constant and T is temperature.) At room temperature the average Hamiltonian is typically less than one percent of $k_{\mathrm{B}}T$, so the exponential can be expanded to first order. For a sample equilibrated under the influence of a constant magnetic field in the z direction,

$$\rho^{\mathrm{eq}} \simeq a(\hat{E} - b\hat{S}_z), \tag{2.39}$$

where $\hat{E}$ is the identity operator in Hilbert space, and a and b are scalar coefficients.

At any later time the density matrix can always be written in the form

$$\rho(t) \simeq a(\hat{E} + \sigma(t)) \tag{2.40}$$

since $\hat{E}$ commutes with the Hamiltonian. Additionally, $\hat{E}$ has no effect on the expectation value of the magnetization, $\mathrm{Tr}\{\hat{\boldsymbol{M}}\hat{E}\} = 0$, because $\hat{\boldsymbol{M}}$ is proportional to $\hat{\boldsymbol{S}}$. As a result, one only needs to keep track of $\sigma(t)$, which in that sense is the relevant part of the density matrix. The initial condition of σ follows from Eq. (2.39): $\sigma(0) = \sigma^{\mathrm{eq}} \propto \hat{S}_z$. In a FID experiment, a 90° pulse rotates the magnetization about the x axis, leading to $\sigma(0^+) \propto \hat{S}_y$, which implies $\sigma^{-+}(0^+) \propto \hat{E}_I$.

2.2.2 Generating stochastic trajectories for rotational diffusion

In this section, we develop an efficient numerical integrator for the rotational Brownian diffusion of a body-fixed frame `B` with respect to a space-fixed frame `S`. The presence of an ordering potential $U(\Omega)$, where $\Omega = \{\alpha, \beta, \gamma\}$ denotes the instantaneous orientation of `B` with respect to `S` parametrized using the Euler angles α, β and γ, is also allowed. This basic model forms the basis for more sophisticated motional models like MOMD and SRLS.

Quaternions and rotational dynamics

When dealing with kinematics of rotations it is more convenient to work with quaternions rather than Euler angles. (The relation between the two sets of parameters is given in Eq. (2.80).) To keep track of the orientation of `B` with respect

to S, we use the 2×2 unitary matrices,

$$\mathcal{Q} = \begin{pmatrix} q_0 - \mathrm{i}q_3 & -q_2 - \mathrm{i}q_1 \\ q_2 - \mathrm{i}q_1 & q_0 + \mathrm{i}q_3 \end{pmatrix} = q_0\sigma_0 - \mathrm{i}\sum_i q_i\sigma_i, \tag{2.41}$$

with unit determinant,

$$q_0^2 + q_1^2 + q_2^2 + q_3^2 = 1. \tag{2.42}$$

The Pauli spin matrices σ_1, σ_2, σ_3 and the 2×2 identity matrix σ_0 should not be confused with the density matrix of the previous section. The real numbers q_i are the components of the quaternion corresponding to the transformation relating B to S. When the coordinate frame B moves with respect to S, $\mathcal{Q}$ becomes time dependent. Its equation of motion is

$$\frac{\mathrm{d}}{\mathrm{d}t}\mathcal{Q}(t) = \mathcal{W}(t)\mathcal{Q}(t), \tag{2.43}$$

where

$$\mathcal{W}(t) = -\mathrm{i}\frac{1}{2}\sum_i \omega_i(t)\sigma_i. \tag{2.44}$$

In these expressions $\boldsymbol{\omega}(t)$ is the instantaneous angular velocity of B. Its components ω_i are with respect to S. Given a time series of $\boldsymbol{\omega}(t)$, Eq. (2.43) can be integrated numerically to generate the time series of $\mathcal{Q}$, as was done by Fedchenia and Westlund in their rigorous treatment of isotropic rotational diffusion restricted to a conical region [42].

In the case of anisotropic diffusion, it becomes necessary to work with the components of $\boldsymbol{\omega}$ with respect to B (as discussed in more detail below). Denoting these by $\omega_{i'}$, and defining

$$\mathcal{W}'(t) = -\mathrm{i}\frac{1}{2}\sum_i \omega_{i'}(t)\sigma_i, \tag{2.45}$$

the equation of motion of $\mathcal{Q}$ becomes

$$\frac{\mathrm{d}}{\mathrm{d}t}\mathcal{Q}(t) = \mathcal{Q}(t)\mathcal{W}'(t). \tag{2.46}$$

Observe the algebraically trivial but important difference between Eq. (2.43) and Eq. (2.46). In the former, the components of the angular velocity of the rotating frame are with respect to the stationary frame; in the latter, they are with respect to the body-fixed frame. Equation (2.46) may be integrated numerically as

$$\mathcal{Q}(t+\Delta t) = \mathcal{Q}(t)\, \mathrm{e}^{\Delta t \mathcal{W}_{\prime}(t)}. \tag{2.47}$$

This form of propagation is very attractive because it preserves the determinant of $\mathcal{Q}$, and thus the normalization of the quaternion (Eq. (2.42)). In close similarity to the evaluation of Eq. (2.35) using Eq. (2.37), the matrix in Eq. (2.47) can be exponentiated calculating only trigonometric functions:

$$\begin{aligned} \exp\left(-\mathrm{i}\sum_i \frac{\omega_{i'}(t)\Delta t}{2}\sigma_i\right) &= \cos\theta\,\sigma_0 - \mathrm{i}\sin\theta\sum_i u_i\sigma_i \\ &= \begin{pmatrix} \cos\theta - \mathrm{i}u_z\sin\theta & -(u_y+\mathrm{i}u_x)\sin\theta \\ (u_y-\mathrm{i}u_x)\sin\theta & \cos\theta + \mathrm{i}u_z\sin\theta \end{pmatrix}. \end{aligned} \tag{2.48}$$

Here θ and $\underline{\boldsymbol{u}} = (u_x, u_y, u_z)$ denote respectively the magnitude and the direction of the vector $\boldsymbol{\omega}_{\prime}(t)\Delta t/2$. Equations (2.47) and (2.48) constitute our numerical scheme for propagating the quaternion $\mathcal{Q}_{\mathtt{SB}}$ describing the orientation of the coordinate system `B` with respect to the system `S`. What is missing so far is the physics of the orientational dynamics, to be addressed next, which determines how $\boldsymbol{\omega}_{\prime}(t)$ changes with time.

Anisotropic Brownian diffusion in external potential

Starting from this section we drop the subscript prime with the understanding that all the vector and tensor components are with respect to `B`. We are interested in describing rotational diffusion in the presence of a potential $U(\Omega)$. In the

limit of high friction, when inertial terms can be neglected, the components of the instantaneous angular velocity $\boldsymbol{\omega}(t)$ (in $\mathtt{B}$) satisfy the equation of motion [25, 70]

$$\boldsymbol{\omega}(t) = -\mathsf{D}\boldsymbol{\nabla} u\big(\Omega(t)\big) + \boldsymbol{\xi}(t). \tag{2.49}$$

The first term on the right hand side of the equality corresponds to the systematic torque due to the potential

$$u(\Omega) \equiv U(\Omega)/k_{\mathrm{B}}T, \tag{2.50}$$

whereas the second term is the random torque which leads to the orientational diffusion. The other symbols in Eq. (2.49) are the rotational diffusion tensor D (diagonal in $\mathtt{B}$) and the orientational gradient operator [2]

$$\boldsymbol{\nabla} = \left(\tfrac{\partial}{\partial\phi_x}, \tfrac{\partial}{\partial\phi_y}, \tfrac{\partial}{\partial\phi_z}\right), \tag{2.51}$$

where ϕ_i is the angle of rotation around the ith axis of $\mathtt{B}$. The components of the random torque satisfy the conditions [25, 70]

$$\mathbb{E}\{\xi_i(t)\} = 0, \quad \mathbb{E}\{\xi_i(t_1)\xi_j(t_2)\} = 2D_{ii}\delta_{ij}\delta(t_1 - t_2), \tag{2.52}$$

where $\mathbb{E}$ denotes expectation over the Gaussian probability density of $\boldsymbol{\xi}$. In this last expression D_{ii} are the components of D (wrt $\mathtt{B}$).

It is important to realize that conditions (2.52) are valid only when the components of $\boldsymbol{\xi}$ are with respect to the coordinate frame in which the diffusion tensor is diagonal. Only in this frame do the components of the diffusion tensor, and therefore the intensities of the random torque, decouple. An isotropic diffusion tensor is diagonal in any coordinate system, including the space-fixed frame, which makes it possible to express all the vector components exclusively with respect to $\mathtt{S}$. To treat the general anisotropic case, we have to work with the components of the

diffusion tensor with respect to B. Hence, as already alluded to, using Eq. (2.46) instead of Eq. (2.43) is crucial.

Writing the torque $-\boldsymbol{\nabla}u(\Omega)$ in terms of the angular momentum operator $\boldsymbol{J}$ [25, 70, 106],

$$-\boldsymbol{\nabla}u(\Omega) = -\mathrm{i}\boldsymbol{J}u(\Omega), \tag{2.53}$$

Eq. (2.49) can be rewritten in component form as

$$\omega_i(t) = -\mathrm{i}D_{ii}J_i u\big(\Omega(t)\big) + \xi_i(t), \tag{2.54}$$

where the partial differential operators corresponding to the components J_i (in B) are [9]

$$\begin{aligned} J_z &= -\mathrm{i}\frac{\partial}{\partial\gamma} \\ J_\pm &= \mathrm{e}^{\mp\mathrm{i}\gamma}\left[-\mathrm{i}\cot\beta\frac{\partial}{\partial\gamma} \pm \frac{\partial}{\partial\beta} + \frac{\mathrm{i}}{\sin\beta}\frac{\partial}{\partial\alpha}\right], \end{aligned} \tag{2.55}$$

with $J_\pm = J_x \pm \mathrm{i}J_y$. The action of the J_i's on the potential becomes analytically tractable if the latter is written as an expansion over the eigenfunctions of the former. The Wigner functions

$$\mathscr{D}^j_{nm}(\Omega) = \mathrm{e}^{-\mathrm{i}n\alpha}d^j_{nm}(\beta)\mathrm{e}^{-\mathrm{i}m\gamma} \tag{2.56}$$

are eigenfunctions of J_z that satisfy [9]

$$\begin{aligned} J_z\mathscr{D}^j_{nm}(\Omega) &= -m\mathscr{D}^j_{nm}(\Omega) \\ J_\pm\mathscr{D}^j_{nm}(\Omega) &= -\sqrt{j(j+1)-m(m\pm1)}\,\mathscr{D}^j_{nm\pm1}(\Omega). \end{aligned} \tag{2.57}$$

Therefore, it is convenient to chose the ordering potential in the form [18, 94, 106–108]

$$u(\Omega) = -\sum_{j,m} c^j_m \mathscr{D}^j_{0m}(\Omega), \tag{2.58}$$

which leads to the expressions

$$
\begin{aligned}
-\mathrm{i}J_x u &= -\frac{\mathrm{i}}{2}\sum_{j,m} c_m^j \left(C_+^{j,m}\mathscr{D}_{0m+1}^j + C_-^{j,m}\mathscr{D}_{0m-1}^j\right) \\
-\mathrm{i}J_y u &= -\frac{1}{2}\sum_{j,m} c_m^j \left(C_+^{j,m}\mathscr{D}_{0m+1}^j - C_-^{j,m}\mathscr{D}_{0m-1}^j\right) \\
-\mathrm{i}J_z u &= -\mathrm{i}\sum_{j,m} c_m^j m\mathscr{D}_{0m}^j,
\end{aligned}
\tag{2.59}
$$

where the coefficients

$$
C_\pm^{j,m} \equiv \sqrt{j(j+1) - m(m\pm 1)} \tag{2.60}
$$

have been introduced to simplify the notation. Expressions (2.59) are evaluated in Sec. 2.5.3 for some popular choices of the potential. There, the advantage of writing the differential operator (2.51) in terms of the angular momentum operators J_i becomes apparent. The action of J_z and $J_\pm$ on the Wigner rotation matrices transforms the problem of differentiation of the potential to straightforward algebraic manipulation of the components of the corresponding quaternion. The only remaining task is to account for the random term in Eq. (2.54). Given its statistical properties, Eq. (2.52), the numerical integration of Eq. (2.54) involves the generation of three random numbers $N_i(t)$ with Gaussian distribution of zero mean and unit standard deviation, which are then used to calculate

$$
\frac{\omega_i(t)\Delta t}{2} = -\mathrm{i}J_i u\big(\mathcal{Q}(t)\big)\frac{D_{ii}\Delta t}{2} + \sqrt{\frac{D_{ii}\Delta t}{2}}\,N_i(t). \tag{2.61}
$$

The combination $\omega_i(t)\Delta t/2$ was the necessary input to Eqs. (2.47) and (2.48).

Spherical grid for the initial conditions

Finally, we consider the initial conditions for the rotational diffusion, which can be generated as random orientations of `B` with respect to `S`, weighted by the Boltzmann

factor $\exp(-u(\Omega))$. In practice, systematically covering the surface of a sphere with a homogeneously distributed grid is found to be much more efficient than a random choice [110]. Different spherical grids are compared in Ref. [110], where it is conclusively demonstrated that distributing the points along a spiral that twists from the north pole to the south pole leads to the most efficient grid with high convergence rate. The spherical polar coordinates of the points along the spiral are [110]

$$\theta_i = \arccos(s_i) \qquad \phi_i = \sqrt{\pi N}\arcsin(s_i), \tag{2.62}$$

where $s_i \in (-1, 1)$, $i = 1, \ldots, N$, parametrizes the spiral and N is the number of points on the spiral. The potentials $u(\Omega)$ that we consider are proportional to $\mathscr{D}^j_{0m}(\Omega)$ (see Sec. 2.5.3). Since these Wigner functions are independent of α, the initial conditions for the Euler angles are chosen as $\alpha = 0$, $\beta = \theta_i$ and $\gamma = \phi_i$, and the corresponding quaternion is calculated using Eq. (2.80).

2.2.3 Testing the integrators

Building on the rotational dynamics discussed above, it is straightforward to generate trajectories for typical stochastic models of the spin label dynamics like Brownian rotational diffusion (BD), microscopic order macroscopic disorder (MOMD) [94] and slowly relaxing local structure (SRLS) [106, 107], which schematically can be represented as:

$$\text{BD}: \quad \mathtt{L} \xrightarrow[\text{diffusion}]{\text{free (an)isotropic}} \mathtt{M} \xrightarrow{\text{fixed}} \mathtt{N}$$

$$\text{MOMD}: \quad \mathtt{L} \xrightarrow{\text{powder}} \mathtt{D} \xrightarrow[\text{diffusion}]{\text{restricted (an)isotropic}} \mathtt{M} \xrightarrow{\text{fixed}} \mathtt{N}$$

$$\text{SRLS}: \quad \mathtt{L} \xrightarrow[\text{diffusion}]{\text{free isotropic}} \mathtt{D} \xrightarrow[\text{diffusion}]{\text{restricted (an)isotropic}} \mathtt{M} \xrightarrow{\text{fixed}} \mathtt{N}$$

Here, the molecular frame M is allowed to diffuse with respect to D. The ordering potential which restricts the diffusion of M is fixed in this latter "director" frame. In that sense M and D correspond, respectively, to the body-fixed frame B and stationary frame S of Sec. 2.2.2. D itself can be either randomly oriented (MOMD) or undergo free isotropic diffusion (SRLS) with respect to L. In the BD model there is no ordering potential, thus the intermediate director frame is skipped. The initial conditions for each of the diffusion parts in a given model are chosen from points distributed on a spherical grid.

In addition to the dynamical events explicitly present in the models, the spectral lines are typically broadened for reasons not accounted for in the simulation. Such broadening can be easily included phenomenologically in the form of Lorentzian and Gaussian relaxation times. Lorentzian broadening with relaxation time constant T_{L} is achieved by multiplying the magnetization $M_+(t)$ by $\mathrm{e}^{-t/T_{\mathrm{L}}}$. Gaussian broadening is introduced by convoluting the spectral lines with a Gaussian. Since convolution in the frequency domain is multiplication in the time domain, this can be done by multiplying $M_+(t)$ by $\mathrm{e}^{-t^2/8T_{\mathrm{G}}^2}$, where T_{G} is the derivative peak-to-peak linewidth of the Gaussian. Lastly, the trajectories are of some finite duration T. To prevent the contamination of the spectrum with high frequencies due to the abrupt termination of the trajectories, the integrand is multiplied by the Hamming window [37]

$$h_T(t) = 0.54 + 0.46\cos(\pi t/T). \tag{2.63}$$

An absorption spectrum in derivative mode is therefore calculated as

$$\frac{\mathrm{d}\tilde{M}_+(\omega)}{\mathrm{d}\omega} = \mathrm{Im}\int_0^T \mathrm{d}t\, t\, \mathrm{e}^{-\mathrm{i}\omega t} h_T(t) \mathrm{e}^{-t/T_{\mathrm{L}}} \mathrm{e}^{-t^2/8T_{\mathrm{G}}^2} M_+(t). \tag{2.64}$$

ESR spectra at $B_0 = 0.34$ T for the BD model with isotropic diffusion are presented in Fig. 2.1. Our time-domain spectra, simulated using the proposed

Table 2.2: Time scales, $\tau = 1/6D$, for the diffusion rates used in the simulation of the spectra in Figs. 2.1, 2.2 and 2.3.

D ($\times 10^6$ s^{-1})	1	3	10	30	100
τ (ns)	167	55.6	16.7	5.56	1.67

trajectory-based approach, are compared with spectra simulated using the SLE-based software of Freed and co-workers over motional regimes ranging from slow ($D = 1 \times 10^6$ s^{-1}) to fast ($D = 100 \times 10^6$ s^{-1}). The correlation time scales associated with these diffusion rates range from 1.67 ns to 167 ns (Table 2.2). Excellent agreement between the two simulation strategies is observed over the whole motional regime. The effect of the anisotropy of the diffusion tensor is illustrated in Fig. 2.2, where spectra simulated using trajectories are superimposed with spectra simulated with the SLE. Again, the agreement is excellent. As expected, fast rotational diffusion about the nitroxide z-axis ($D_{zz} > D_{yy} > D_{xx}$, top spectrum) does not mix the larger A_{zz} component with the smaller A_{xx} and A_{yy} components as efficiently as fast rotation about the x- and y-axes (bottom two spectra). Therefore the resulting spectrum is more slow-like in the former case compared with the latter two, for which the averaging of A_{zz} is more efficient. Figure 2.3 illustrates the effect of the ordering potential on the spectra. The ordering potential for the top spectrum was as given in Eq. (2.93) with $c_0^2 = 2.0$. The potential for the bottom spectrum was as in Eq. (2.95) with $c_2^2 = 2.0$. Isotropic diffusion with $D = 30 \times 10^6$ s^{-1} was used for both of the simulations. Again, the continuous lines were simulated in the frequency domain, by the SLE, and the dashed lines in the time domain. The agreement is excellent.

The values of the magnetic tensors used in the simulations in Figs. 2.1, 2.2 and 2.3 are given in Eq. (2.22). The other simulation parameters are summarized

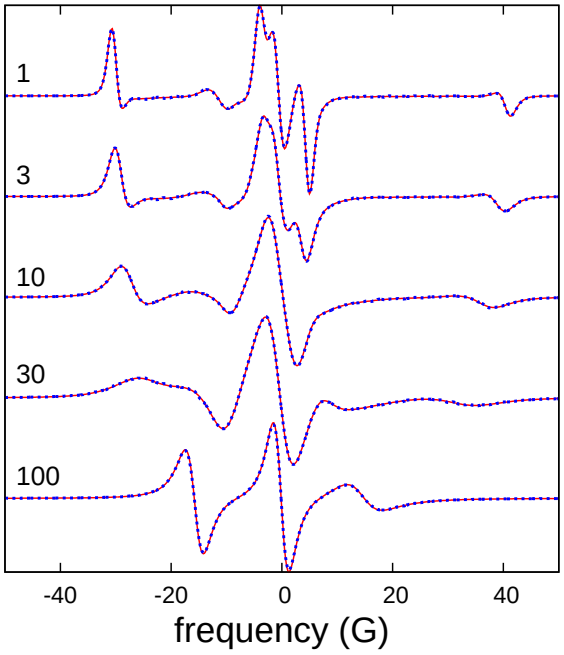

Figure 2.1: Spectra of isotropic free diffusion for various diffusion rates, in units of 10^6 s^{-1}, simulated using the trajectory-based approach (dashed lines) and the SLE (continuous lines).

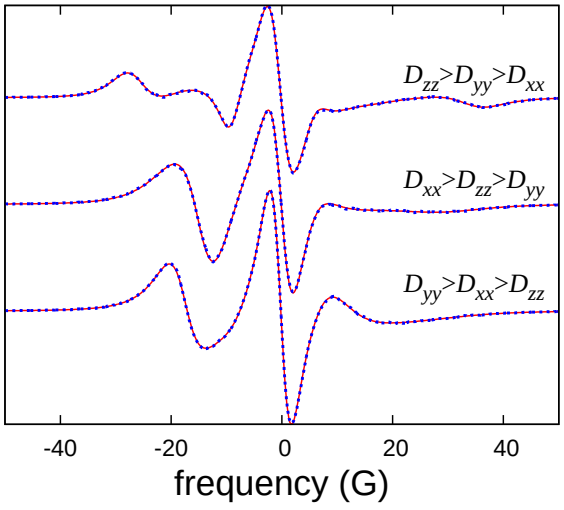

Figure 2.2: Simulated time-domain (dashed) and frequency-domain (continuous) spectra of anisotropic free diffusion. The components of the diffusion tensor, 10×, 30× and 100×10^6 s^{-1}, were assigned in the order indicated in the plot.

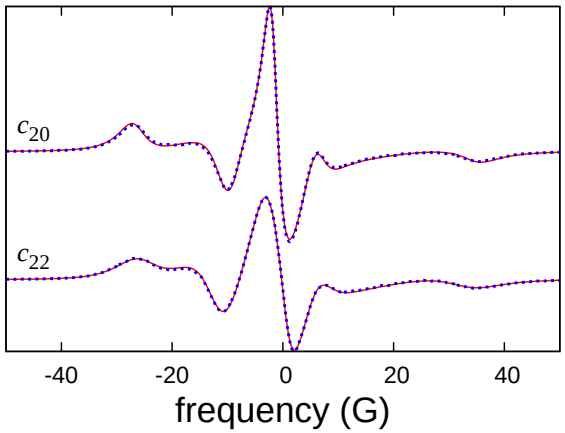

Figure 2.3: Comparison of time-domain (dashed) and SLE (continuous) spectra for two MOMD models with $(c_0^2, c_2^2) = (2.0, 0)$ and $(0, 2.0)$, respectively. The nonzero coefficient is indicated next to the spectrum. $D = 30 \times 10^6$ s^{-1}.

in Table 2.3. There, 'stpN' indicates the number of simulation steps that each stochastic trajectory lasted and Δt is the integration time step. Naturally, the duration of each trajectory is the product of these two. 'freN' and 'rstN' are the number of spherical grid points used for the two separate spherical grids. 'freN' points were used for the free diffusion of `M` (BD) and the random distribution of `D` (MOMD) with respect to `L`. 'rstN' points were used for the restricted diffusion of `M` with respect to `D` (MOMD). Since this last diffusion is not present in the BD model, 'rstN' in this case indicates the number of independent trajectories initiated from each of the 'freN' spherical grid points. Finally, the last column gives the value of the inhomogeneous Gaussian broadening introduced in the spectra by hand. Note that the integration time step used to simulate the spectra in Figs. 2.1 and 2.2 is much smaller than the correlation time scales of the rotational diffusion (Table 2.2), thus, it should be sufficient to follow the dynamics. The only exception is $D = 100 \times 10^6$ s^{-1}. The excellent agreement of our spectra with the spectra simulated using the SLE indicates that even in this case the integration time step

Table 2.3: Parameters used in the simulation of the spectra in Figs. 2.1, 2.2 and 2.3.

model	B_0 (T)	stpN	Δt (ns)	freN	rstN	T_{G}^{-1} (G)
BD	0.34	800	1.0	1600	800	1.0
MOMD	0.34	2000	0.4	3200	1600	1.0

is adequate. A smaller integration time step was chosen for the two MOMD models to ensure the faithful resolution of the gradient of the potential energy.

To the best of our knowledge, this is the first time ESR spectra simulated using trajectories of free or restricted non-isotropic rotational diffusion models show quantitative agreement with spectra simulated using the SLE. It is worth emphasizing though, that the simulation of the spectra reported in Figs. 2.1, 2.2 and 2.3 using stochastic trajectories was at least a thousand times slower than their calculation with the SLE. Using trajectories is therefore justified only when the dynamics is not amenable to treatment with the SLE, as in the case of MD simulations. When spectra of the BD, MOMD and SRLS models need to be simulated, the SLE should be the method of choice.

2.3 Combining MD and stochastic trajectories

MD simulations of a spin labeled macromolecule are expected to offer insight into the detailed dynamics of the spin label and its environment. At the same time, the simulations will most certainly fail to sample the global macromolecular dynamics, e.g. the tumbling of a protein in solution. In such cases, the MD trajectories will not reflect the experimental situation realistically and ESR spectra simulated

from them will fail to reproduce the observed spectra. Thus, for the quantitative comparison of simulated and recorded spectra, it becomes necessary to be able to introduce the effect of the rotational diffusive dynamics in addition to the dynamics of the spin label present in the MD trajectories. This can be achieved by allowing the coordinate system M, attached to the macromolecule, to undergo isotropic (or anisotropic) rotational diffusion with respect to the lab-fixed coordinate frame L:

$$\mathtt{L} \xrightarrow{\text{rot. diff.}} \mathtt{M} \xrightarrow{\text{MD traj.}} \mathtt{N}. \tag{2.65}$$

In this scheme, the dynamics of the coordinate frame N with respect to M are provided by the MD trajectories, whereas the dynamics of M with respect to L are generated using the time-domain formalism developed in the previous section. Below, we discuss a few formal issues related to putting such a stochastic/MD trajectory-based approach into use and illustrate its application using the MD trajectories of a spin labeled poly-alanine α-helix in explicit solvent (Ch. 3).

2.3.1 Coarse-graining the MD trajectories in time

The trajectories coming from all-atom MD simulations are typically sampled about every $\delta t = 1$ ps. Although it is possible to use every snapshot from the trajectories and integrate the quantum spin dynamics with this time step, this would be wasteful since the magnetization relaxes on a much longer time scale. One option is to decimate the MD trajectories and use snapshots separated by a hundred or a thousand steps. Alternatively, the magnetic tensors can be averaged over a time window Δt ($\Delta t \gg \delta t$), along each MD trajectory. The time averaging can be justified by the same arguments that led to the high-field approximation. The only complication is the possibility of resonance [130, 141] between the Larmor precession and

the variations of the magnetic tensors at the Larmor frequency. Eventually, we will neglect the effect of the resonance, but to clarify the assumptions making this possible we start by considering it.

The Fourier series decomposition of the operators $\hat{V}_{\kappa=z,\pm}(t)$, defined in Eq. (2.10), in the interval $[t, t+\Delta t)$ can be written as

$$\hat{V}_\kappa(t+\tau) = \hat{V}_\kappa^{(0)}(t) + \sum_{\mu\neq 0} \hat{V}_\kappa^{(\mu)}(t)\, \mathrm{e}^{\mathrm{i}\mu\tau/\epsilon}, \tag{2.66}$$

where $\tau \in [0, \Delta t)$, $\epsilon = \Delta t/2\pi$, and $\mu = \pm 1, \pm 2, \cdots$. The zero-frequency term $\hat{V}_\kappa^{(0)}(t)$ has been separated from the fast fluctuations which are isolated in the exponents $\mathrm{e}^{\mathrm{i}\mu\tau/\epsilon}$. The coefficients $\hat{V}_\kappa^{(\nu)}(t)$ are slowly varying. They are constant during each time interval Δt and change only when going from one interval to the next, which is the reason for their t dependence. The part $\hat{V}_\kappa^{(0)}(t)$ is the average value of the Hamiltonian in each time interval; it is the only part that we will ultimately use.

To simplify the argument and keep track of the resonance, let us choose the fast time scale, over which we intend to average, to be an integer multiple of the Larmor precession time scale: $\epsilon = n/\omega_0$. With that, the interaction Hamiltonian becomes

$$\hat{V}'(t) = \hat{V}^{(0)}(t) + \sum_{\mu\neq 0} \hat{V}^{(\mu)}(t)\mathrm{e}^{\mathrm{i}\mu t/\epsilon}, \tag{2.67}$$

where we have defined

$$\hat{V}^{(\nu)}(t) \equiv \hat{V}_z^{(\nu)}(t) + \sum_{\kappa=\pm} \hat{V}_\kappa^{(\nu-\kappa n)}(t) \tag{2.68}$$

for $\nu = 0, \pm 1, \pm 2, \cdots$ (cf. Eq. (2.9)). As before, we look for a solution of the Schrödinger equation (2.7) in the form (2.14). Again, our goal is to derive an equation of motion for $|\psi^0(t)\rangle$ only, since the fast oscillations will average out the

rest. The non-oscillating terms give

$$|\dot{\psi}^0(t)\rangle = -\mathrm{i}\hat{V}^{(0)}(t)|\psi^0(t)\rangle - \epsilon\mathrm{i}\sum_{\mu\neq 0}\hat{V}^{(-\mu)}(t)|\psi^\mu(t)\rangle, \tag{2.69}$$

whereas the oscillating terms, proportional to $\mathrm{e}^{\mathrm{i}\mu t/\epsilon}$ with $\mu \neq 0$, lead to

$$\mathrm{i}\mu|\psi^\mu(t)\rangle + \epsilon|\dot{\psi}^\mu(t)\rangle = -\mathrm{i}\hat{V}^{(\mu)}(t)|\psi^0(t)\rangle - \epsilon\mathrm{i}\sum_{\nu\neq 0}\hat{V}^{(\mu-\nu)}(t)|\psi^\nu(t)\rangle. \tag{2.70}$$

When an equation for $|\psi^0(t)\rangle$ to first order in ϵ is desired, it is enough to determine $|\psi^\mu(t)\rangle$ to zeroth order in ϵ from this last equation. To that order,

$$|\psi^\mu(t)\rangle = -\frac{1}{\mu}\hat{V}^{(\mu)}(t)|\psi^0(t)\rangle. \tag{2.71}$$

Substituting in Eq. (2.69), we obtain

$$|\dot{\psi}^0(t)\rangle = -\mathrm{i}\hat{H}_\mathrm{S}(t)|\psi^0(t)\rangle, \tag{2.72}$$

with slow Hamiltonian

$$\hat{H}_\mathrm{S}(t) \equiv \hat{V}^{(0)}(t) + \epsilon\sum_{\mu>0}\frac{1}{\mu}[\hat{V}^{(\mu)}(t), \hat{V}^{(-\mu)}(t)]. \tag{2.73}$$

Equation (2.73) is a generalization of Eq. (2.19). There, to zeroth order, one only had to consider $\hat{V}_z(t)$, which was proportional to $\hat{S}_z$, leading to the slow Hamiltonian (2.23). Here, even to zeroth order, terms proportional to $\hat{S}_\pm$, namely $\hat{V}_\pm^{(\mp n)}(t)$, are present in $\hat{V}^{(0)}(t)$ (as can be seen from Eq. (2.68) with $\nu = 0$). As a reminder, n was chosen to be the ratio between the Larmor precession frequency and the frequency for which the time averaging is performed. The terms $\hat{V}_\pm^{(\mp n)}(t)$, therefore, correspond to fast variation in the magnetic tensors at the Larmor frequency. By going to the frame rotating at the Larmor frequency, the oscillations of the magnetic tensors which rotate at the same frequency but in the "opposite sense" are seen at zero frequency. This is the resonance phenomenon that was

previously mentioned. We assume that the variation of the magnetic tensors at the time scale of the Larmor frequency is much smaller than the variation during the the time interval Δt over which the averaging is performed. This assumption seems reasonable given that the fast time scale (last row of Table 2.1) and the slow time scale (last row of Table 2.4, to be estimated below), are separated by at least an order of magnitude. Thus we neglect $\hat{V}_{\pm}^{(\mp n)}(t)$ in comparison with $\hat{V}_z(t)$. It is worth emphasizing again that neglecting the parts of the Hamiltonian which oscillate on the time scale of the Larmor precession limits our analysis to T_2 relaxation processes. The relaxation of the longitudinal magnetization is driven by $\hat{V}_{\pm}^{(\mp n)}(t)$ and is entirely missed when these terms are neglected.

Now let us estimate the magnitude of the correction to the zeroth order slow Hamiltonian. In Eq. (2.73), $1/\epsilon = 2\pi/\Delta t$, where Δt is the time window over which we want to average. $\Delta t = 1$ ns, for example, corresponds to f=1000 MHz. Variation of A on the order of 30 G is about 100 MHz. Therefore the $\mu = 1$ term containing the hyperfine tensor is suppressed by at least 1/10. For $B_0 = 1.2$ T the variation of the traceless part of g is also about 100 MHz and increases for higher fields. Thus $\Delta t = 1$ ns is a conservative time step for $B_0 = 0.34$ T and 1.21 T. When $B_0 = 12.8$ T the time step should be ten times smaller, so $\Delta t = 1/10$ ns is more appropriate. In between, one can choose $\Delta t = 1/3$ ns for $B_0 = 3.4$ T, $\Delta t = 1/5$ ns for $B_0 = 6.07$ T and $\Delta t = 1/8$ ns for $B_0 = 8.92$ T. These choices are summarized in Table 2.4. They are on the conservative side, especially for the stronger fields, since we have assumed that the magnetic tensors change by the maximum possible amount over the duration of the averaging interval Δt.

Table 2.4: Estimates for the duration of the time averaging window Δt for various magnetic field strengths B_0.

B_0 (T)	0.34	1.21	3.39	6.07	8.92	12.8
Δt (ns)	1	1	1/3	1/5	1/8	1/10

2.3.2 Averaged magnetic tensors

Finally, we discuss how to average the magnetic tensors over the desired time interval Δt. The tensors G and A, collectively denoted by T, are diagonal in $\mathtt{N}$. Their transformation to $\mathtt{L}$ is achieved as

$$T^{\mathtt{L}}_{ij}(t) = \sum_k R_{ik}(\mathcal{Q}_{\mathtt{LN}}(t)) T^{\mathtt{N}}_{kk} R_{jk}(\mathcal{Q}_{\mathtt{LN}}(t)), \tag{2.74}$$

where the rotation matrix $\mathsf{R}(\mathcal{Q}_{\mathtt{LN}}(t))$ rotates the axes of $\mathtt{L}$ to the axes of $\mathtt{N}$ at time t. (Equation (2.81) shows how the rotation matrix is calculated from the quaternion.) When nested rotational frames are considered,

$$\mathtt{L} \xrightarrow{\mathcal{Q}_{\mathtt{LM}}(t)} \mathtt{M} \xrightarrow{\mathcal{Q}_{\mathtt{MN}}(t)} \mathtt{N}, \tag{2.75}$$

the quaternion corresponding to the transformation $\mathtt{L} \to \mathtt{N}$ is obtained as the product of the quaternions of all the successive transformations: $\mathcal{Q}_{\mathtt{LN}}(t) = \mathcal{Q}_{\mathtt{LM}}(t)\mathcal{Q}_{\mathtt{MN}}(t)$. Suppose that the last of these transformations is available as an MD trajectory with fine temporal resolution δt. Assuming that the other transformations evolve on a time scale Δt much longer than δt, the time-averaging of the trajectory is performed as follows. First, the averaged magnetic tensors

$$\bar{\mathsf{T}}^{\mathtt{M}}(t) \equiv \overline{\mathsf{R}_{\mathtt{MN}}(t)\mathsf{T}^{\mathtt{N}}\mathsf{R}^{\top}_{\mathtt{MN}}(t)} \tag{2.76}$$

are calculated, where the line indicates that the quantity under it is averaged over a time window Δt. Then, for each time window, the coordinate frame in which

the averaged tensor is diagonal is determined. The similarity transformation

$$\bar{\mathsf{T}}^{\mathtt{M}}(t) = \mathsf{R}_{\mathtt{MT}}(t)\bar{\mathsf{T}}^{\mathtt{T}}(t)\mathsf{R}_{\mathtt{MT}}^{\top}(t), \tag{2.77}$$

where $\bar{\mathsf{T}}^{\mathtt{T}}$ is a diagonal matrix, defines the (instantaneous) coordinate frame $\mathtt{T}$ of the averaged magnetic tensor. It is clear that even though G and A are diagonal in the same coordinate frame $\mathtt{N}$, after the averaging the principle axes of the two frames will, in general, separate. Therefore, one needs to keep track of the frames $\mathtt{G}$ and $\mathtt{A}$ as a function of the averaging window. This is done by recording the three diagonal entries of $\bar{\mathsf{T}}^{\mathtt{T}}$ ($\mathsf{T} = \mathsf{G}, \mathsf{A}$) and the quaternion $\mathcal{Q}_{\mathtt{MT}}$ ($\mathtt{T} = \mathtt{G}, \mathtt{A}$) for each averaging window.

2.3.3 Application to R1 on a poly-alanine α-helix

We illustrate the stochastic/MD methodology presented above using a set of 18 MD trajectories of a spin-labeled, 15-residue, poly-alanine α-helix. The system was fully solvated with 686 TIP3P waters and simulated with CHARMM. The resulting system of of 2247 atoms filled a tetragonal simulation box with starting side lengths of 26.0, 26.0 and 34.0 Å. Periodic boundary conditions were used. The electrostatics were treated with particle mesh Ewald summation. Pressure and temperature pistons were used to achieve an NpT ensemble at $T = 297$ K and $p = 1$ atm. To prevent the unfolding of the helix in water the first five and the last five residues were harmonically restrained to their starting positions with force constants of 0.5 kcal/mol/Å^2. Each of the 18 trajectories extended for 100 ns. Snapshots were saved every 1 ps. Additional details about the simulations are given in Ch. 3. The viscosity of the TIP3P water model used in the simulations is about 2.86 times smaller than the experimental value [43,148]. Since the spin label

in the simulations is solvent exposed, to account for the underestimated solvent viscosity we scale the MD time axis by a factor of 2.5. As a result, the time interval between two MD snapshots becomes $\delta t = 2.5$ ps, and the effective duration of the trajectories becomes 250 ns.

Dividing the estimates of Δt from Table 2.4 by δt gives the number of MD frames one needs to average over. To assess the reliability of the estimated averaging windows, we perform the spectral simulations for two different values of Δt: half and twice the estimated value. These are listed in Table 2.5 as parameter sets A and B, respectively. The numbers in the 'avgN' column correspond to the number of $\delta t = 2.5$ ps steps one averages over to obtain the coarse-grained time step in the Δt column. Since we deal with a very limited number of MD trajectories, we use the fact that the origin of time is arbitrary and start the integration of the quantum dynamics from points along the MD trajectories separated by 2 ns. The last two columns in Table 2.5 list the number of spherical grid points 'sphN', used for the initial conditions of the isotropic diffusion, and the Gaussian broadening T_{G}^{-1} introduced in the calculation of the spectra. The values of the magnetic tensors used in the spectral simulations were given in Eq. (2.22).

Figure 2.4 shows spectra at five different field strengths simulated with parameter sets A or B. All of the simulations include the effect of isotropic tumbling with a diffusion coefficient $D = 18 \times 10^6$ s^{-1}, in addition to the dynamics coming from the MD trajectories. The diffusion coefficient was chosen as representative of the global rotational diffusion of T4 Lysozyme (T4L) in water at 22°C [4,81]. The agreement between the spectra simulated with the two sets of parameters indicates that in this particular case it is safe to use time steps Δt twice as large as the estimates in Table 2.4. Note that the number of spherical grid points necessary to

Table 2.5: Parameters used in the simulation of the spectra in Fig. 2.4. A lag time of 2.0 ns and an additional Lorentzian broadening of $T_{\mathrm{L}}^{-1} = 0.3$ G were used for all the simulations.

	A		B			
B_0 (T)	Δt (ps)	avgN	Δt (ns)	avgN	sphN	T_{G}^{-1} (G)
0.34	500	200	2.0	800	400	1.0
1.21	500	200	2.0	800	400	1.0
3.39	125	50	0.5	200	3200	1.5
6.07	100	40	0.4	160	6400	1.8
8.92	62.5	25	0.25	100	12800	2.0

obtain smooth spectra (i.e. the number of trajectories one needs to average over) increases significantly with the increase of the magnetic field strength. 32 times more trajectories were generated for the spectra at $B_0 = 8.92$ T compared to the spectra at $B_0 = 0.34$ T.

X-band (0.34 T) spectra of spin labeled T4L are often recorded in 30 wt % sucrose solution to reduce the narrowing effect of the global protein tumbling on the spectral lines [27,51,90,91]. Since this solution is about 3.3 times more viscous than an aqueous solution with no sucrose, the rotational diffusion coefficient of T4L is brought down to about $D = 6 \times 10^6$ s^{-1}. Occasionally, it has been assumed that, as far as the X-band ESR spectra are concerned, the tumbling of the protein in 30 wt % sucrose solution can be disregarded completely, justifying the use of the MOMD model to fit such spectra [26, 27]. In Fig. 2.5 we compare spectra simulated by combining the MD trajectories with stochastic rotational diffusion corresponding to $D = 0$ and 6×10^6 s^{-1}, respectively. The latter (bottom spectrum) accounts for the effect of the global tumbling, whereas the former (top spectrum) corresponds

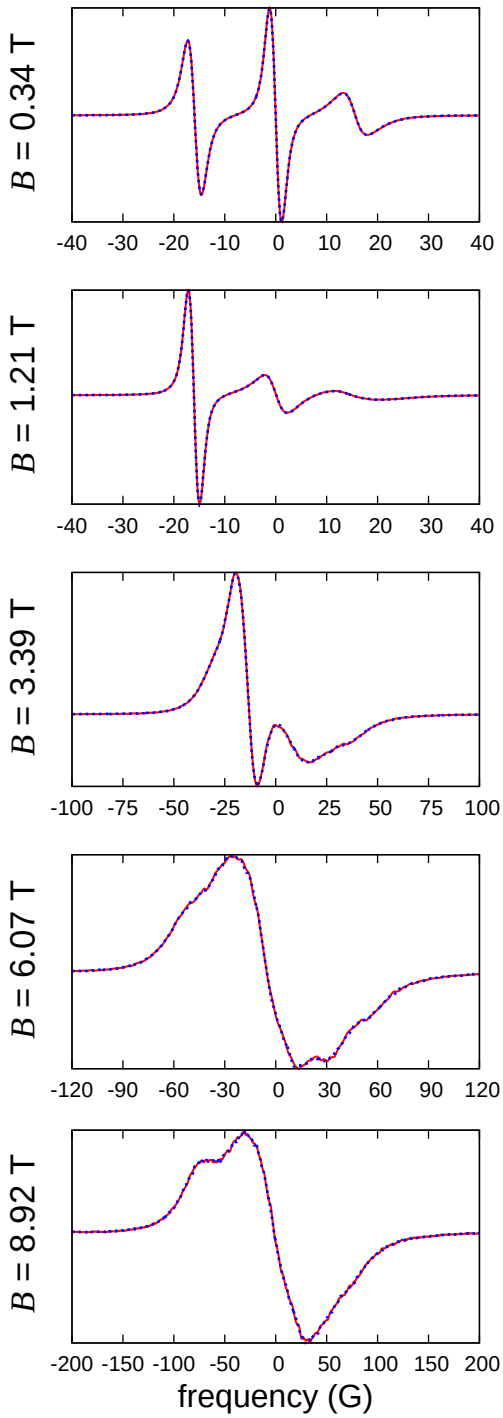

Figure 2.4: Spectra at five different field strengths simulated from the MD trajectories with additional global tumbling ($D = 18 \times 10^6$ s^{-1}) using parameters A (continuous) and B (dashed) in Table 2.5.

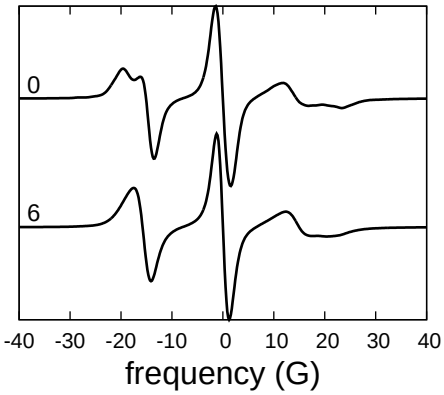

Figure 2.5: Spectra at $B_0 = 0.34$ T for rotational tumbling rates of $D = 0$ and 6×10^6 s^{-1}, simulated using parameters B.

to randomly orientated stationary molecules (powder spectrum). Clearly, the two spectra are significantly different. Explicit treatment of the tumbling appears to be crucial for the quantitative comparison of simulated and experimental spectra of T4L even in 30 wt % sucrose solution.

2.4 Concluding discussion

A methodological framework for combining MD and stochastic trajectories in the time-domain simulation of FID ESR spectra was presented. Stochastic trajectories were used to account for dynamics that are slow and poorly sampled in the MD simulations. Three methodological prerequisites were examined in detail. First, an efficient numerical scheme for propagating the quantum dynamics of the spins was proposed. This was achieved by working with the reduced density matrix in Hilbert space. Second, a rigorous and efficient numerical scheme for the treatment of rotational Brownian diffusion was developed. Using quaternions, instead of Euler angles, to parametrize the relative orientation of two coordinate systems,

allowed us to easily treat the general case of restricted anisotropic diffusion. The familiar restricting potential written as a sum of a few spherical harmonics fits naturally into this formalism. Time-domain spectral simulations performed with the developed quantal and classical integrators were compared with the well established spectral simulation methodology of Freed and co-workers based on the SLE. Excellent agreement was observed. Finally, time averaging of the magnetic tensors was introduced to bridge the gap between the fast time scale of the MD trajectories and the slow time scale of the quantum propagation. Averaging time windows appropriate for the simulations of spectra at different magnetic field strengths were estimated. The methodology of combining MD with stochastic trajectories was illustrated using MD trajectories of spin labeled poly-alanine α-helix.

Previously, three different ways of numerically integrating the spin dynamics of a nitroxide spin label have been proposed [38, 40, 54, 133, 139]. The approach of Steinhoff *et al.*, first introduced in Ref. [133] and more recently employed again in the context of using MD trajectories for spectral simulations [7], uses only the eigenvalues of the instantaneous reduced Hamiltonian. The change of the eigenvectors with time is completely disregarded. Interpolation between the eigenvalues in the high-field and the pseudo-secular approximations (in which not only the nonsecular but also the pseudo-secular terms of the Hamiltonian are neglected) is introduced in an *ad hoc* fashion [7]. Since the three eigenvalues of the Hamiltonian are read directly from its entries, the quantum propagation reduces to updating the time dependent phase of the magnetization. Presumably three different components, each one influenced by one of the eigenvalues, are propagated. The equations in Refs. [133] and [7] are written for a single, complex scalar magnetization, thus concern about a state vector or a density matrix becomes unnecessary, and is not mentioned at all.

Eviatar and Levine developed a rigorous method to simulate ESR spectra of nitroxides in the time domain [40]. They propagate two state vectors in the reduced Hilbert space, as we discussed at the end of Sec. 2.2.1. The authors were reluctant to work with the density matrix because, as they state, "each trajectory describes the motion of a single molecule, and it is therefore impossible to implement any formalism, such as the density matrix, which implies that a calculation is carried out on an ensemble of spins" [38]. In fact, one can think of the density matrix as a purely mathematical construct which emerges as a result of averaging over the initial conditions of the state vector. Eviatar and Levine perform this averaging after the classical ensemble average over the trajectories. Because the quantum propagation along each random trajectory is linear and since the classical and quantum initial conditions are decoupled, one can safely exchange the order of the two averages.

In contrast, Usova and Westlund use the density operator, which they propagate in Liouville space [139]. They do not mention the high-field approximation but in their numerical integration scheme, only the $m_S = -\frac{1}{2}$, $m'_S = +\frac{1}{2}$ subspace of the full Liouville space is considered, which effectively imposes decoupled dynamics for the σ^{-+} sub-block of the density matrix. This is equivalent to neglecting the nonsecular terms, and thus invoking the high-field approximation. The authors propagate the (reduced) density matrix in Liouville space. The disadvantage of working in Liouville space, as opposed to using our Eq. (2.34), is not only due to the larger matrix representation of the (reduced) Liouvillian (9×9) compared to the Hamiltonian (3×3). Whereas in our formulation the Hamiltonian can be easily and exactly exponentiated using Eq. (2.37), this is not the case for the Liouvillian. Instead, the nondiagonal part of the Liouvillian has to be written as a sum of three matrices, each one of which can be exponentiated using an equation similar

to Eq. (2.37) [139]. Since the exponential of the sum is not equal to the product of the separate exponentials, an approximation based on Trotter's formula has to be used [139]. As a result, evaluation of the short-time propagator in Liouville space contains five 9×9-matrix products. In comparison, using Eq. (2.34) with two 3×3-matrix products is not only exact but also more efficient.

Our treatment of rotational Brownian diffusion may be viewed as an extension of the work of Fedchenia and Westlund addressing isotropic rotational diffusion in a cone [42]. A stochastic differential equation for the quaternion was derived from what corresponds to our Eq. (2.43) [42]. While this is appropriate for isotropic diffusion, handling anisotropic diffusion necessitates working with Eq. (2.46). In addition, whereas the conical potential shows its presence only at the (reflecting) boundary, the potentials studied in this chapter act continuously during the diffusion. With all this we are able to treat anisotropic diffusion in a potential exactly. The only approximation is related to the finiteness of the integration time step. This is in contrast to Refs. [101] and [117], where jumps of constant arc length on the surface of a unit sphere are performed in the former, while the second Euler angle is discretized to start with in the latter. Both are limited to free isotropic diffusion.

Steinhoff and Hubbell developed a formalism [133] which does include anisotropic rotational diffusion in a potential. In their presentation no distinction is made between vector/tensor components referred to the body-fixed frame or the stationary frame. As we saw, this is the crucial difference between Eqs. (2.43) and (2.46). From the fact that an equation equivalent to Eq. (2.49) is used in Ref. [133], it can be assumed that all their equations are written in the body-fixed frame. At the same time, Eq. (2.49), or more specifically its short-time version (2.61), only

specifies the increments $\Delta\phi_i = \omega_i \Delta t$ of the angles of rotation about the body-fixed axis $\underline{\boldsymbol{i}}$. The finite values of these angles cannot be used to parametrize a rotation uniquely, because of the noncommuting nature of finite rotations [2]. Probably the Euler angles, or some other parameters parametrizing a finite rotation uniquely, are updated from the infinitesimal increments of the ϕ_is but this is not discussed in Ref. [133]. As a result, it is difficult to compare their mathematical formalism with ours. At the same time, the perfect agreement our spectra show with spectra simulated using the SLE (see Fig. 2.1) can be compared with a similar test for isotropic diffusion in Fig. 6 of Ref. [133]. It is hard to assess whether the reported discrepancy between the spectra in their work is due to the simplified propagation of the quantum dynamics or due to the treatment of the rotational diffusion.

Even when MD and stochastic trajectories are used together, as proposed in this chapter, the demands on the number and duration of the MD trajectories are largely unrealistic for routine MD simulations of solvated spin labeled proteins. In Ch. 4, we explore ways of building Markov chain models from the MD trajectories to simulate the ESR spectra for the models, rather than using the MD trajectories directly. If successful, such an approach will replace the stochastic/MD dynamical model (2.65) with a purely stochastic one:

$$\mathtt{L} \xrightarrow{\text{rot. diff.}} \mathtt{M} \xrightarrow[\text{chain}]{\text{Markov}} \mathtt{N}. \tag{2.78}$$

The time-domain integrators developed in Sec. 2.2 and the time-averaging arguments of Sec. 2.3 remain equally useful for this model.

2.5 Useful expressions

2.5.1 Matrix representations for Eq. (2.37)

Defining $c_\theta = (\cos\theta - 1)$ and $s_\theta = -\sin\theta$, the real and imaginary parts of (2.37) are

$$\mathrm{Re}(\mathrm{e}^{-\mathrm{i}\theta\hat{N}}) = I_3 + \begin{pmatrix} c_\theta[n_z^2 + \frac{1}{2}(n_x^2+n_y^2)] & \frac{1}{\sqrt{2}}[s_\theta n_y + c_\theta n_z n_x] & c_\theta\frac{1}{2}(n_x^2-n_y^2) \\ \frac{1}{\sqrt{2}}[-s_\theta n_y + c_\theta n_z n_x] & c_\theta(n_x^2+n_y^2) & \frac{1}{\sqrt{2}}[s_\theta n_y - c_\theta n_z n_x] \\ c_\theta\frac{1}{2}(n_x^2-n_y^2) & \frac{1}{\sqrt{2}}[-s_\theta n_y - c_\theta n_z n_x] & c_\theta[n_z^2 + \frac{1}{2}(n_x^2+n_y^2)] \end{pmatrix} \tag{2.79a}$$

and

$$\mathrm{Im}(\mathrm{e}^{-\mathrm{i}\theta\hat{N}}) = \begin{pmatrix} s_\theta n_z & \frac{1}{\sqrt{2}}[s_\theta n_x - c_\theta n_z n_y] & -c_\theta n_x n_y \\ \frac{1}{\sqrt{2}}[s_\theta n_x + c_\theta n_z n_y] & 0 & \frac{1}{\sqrt{2}}[s_\theta n_x + c_\theta n_z n_y] \\ c_\theta n_x n_y & \frac{1}{\sqrt{2}}[s_\theta n_x - c_\theta n_z n_y] & -s_\theta n_z \end{pmatrix}, \tag{2.79b}$$

where I_3 indicates the 3×3 identity matrix.

2.5.2 Euler angles, quaternions, the rotation matrix, and elements of the Wigner rotation matrices

If the orientation of `B` with respect to `S` is given in terms of the Euler angles $\Omega = \{\alpha, \beta, \gamma\}$ the components of the corresponding quaternion can be calculated as [85]

$$\begin{aligned} q_0 &= \cos(\beta/2)\cos((\gamma+\alpha)/2) \qquad & q_1 &= \sin(\beta/2)\sin((\gamma-\alpha)/2) \\ q_2 &= \sin(\beta/2)\cos((\gamma-\alpha)/2) \qquad & q_3 &= \cos(\beta/2)\sin((\gamma+\alpha)/2). \end{aligned} \tag{2.80}$$

From the components of the quaternion, the 3×3 rotation matrix is calculated as [9]

$$\mathsf{R} = \begin{pmatrix} q_0^2 + q_1^2 - q_2^2 - q_3^2 & 2q_1q_2 - 2q_0q_3 & 2q_1q_3 + 2q_0q_2 \\ 2q_1q_2 + 2q_0q_3 & q_0^2 - q_1^2 + q_2^2 - q_3^2 & 2q_2q_3 - 2q_0q_1 \\ 2q_1q_3 - 2q_0q_2 & 2q_2q_3 + 2q_0q_1 & q_0^2 - q_1^2 - q_2^2 + q_3^2 \end{pmatrix}. \tag{2.81}$$

The matrix elements of R correspond to the direction cosines between the unit vectors $\underline{\boldsymbol{i}}$ of the stationary coordinate system and the unit vectors $\underline{\boldsymbol{j}'}$ of the rotating body-fixed frame:

$$R_{ij} = \underline{\boldsymbol{i}} \cdot \underline{\boldsymbol{j}'}. \tag{2.82}$$

Therefore, the last row of R gives the components of $\underline{\boldsymbol{z}}$ with respect to the axes of $\mathtt{B}$, i.e. $R_{zx} = (\underline{\boldsymbol{z}})_{x'}$, $R_{zy} = (\underline{\boldsymbol{z}})_{y'}$ and $R_{zz} = (\underline{\boldsymbol{z}})_{z'}$. For later convenience, we find it useful to introduce the notation

$$X \equiv R_{zx}, \qquad Y \equiv R_{zy}, \qquad Z \equiv R_{zz}, \tag{2.83}$$

for these matrix elements.

From the relation

$$\mathscr{D}^{\frac{1}{2}} = \begin{pmatrix} A & B \\ -B^* & A^* \end{pmatrix} = \begin{pmatrix} q_0 - \mathrm{i}q_3 & -q_2 - \mathrm{i}q_1 \\ q_2 - \mathrm{i}q_1 & q_0 + \mathrm{i}q_3 \end{pmatrix}, \tag{2.84}$$

the matrix elements of $\mathscr{D}^1_{nm}$ and $\mathscr{D}^2_{nm}$ may be obtained, see Ref. [85]. These are presented in Table 2.6, where $Z = R_{zz} = AA^* - BB^*$. The normalization condition (A.42) implies that $AA^* + BB^* = 1$.

Observe that

$$\begin{aligned} \mathscr{D}^1_{01} &= -\sqrt{2}(q_0 - \mathrm{i}q_3)(-q_2 + \mathrm{i}q_1) = -\frac{1}{\sqrt{2}}(X + \mathrm{i}Y) \\ \mathscr{D}^1_{0-1} &= -\mathscr{D}^{1*}_{01} = \frac{1}{\sqrt{2}}(X - \mathrm{i}Y), \end{aligned} \tag{2.85}$$

Table 2.6: Matrix elements of $\mathscr{D}^1_{nm}$ and $\mathscr{D}^2_{nm}$, from Ref. [85]. The elements with $m < 0$ which are not shown may be obtained using $\mathscr{D}^2_{n-m} = (-1)^{(n-m)}(\mathscr{D}^2_{-nm})^*$. $(Z = AA^* - BB^*)$

$\mathscr{D}^1_{nm}$	$+1$	0	-1
$+1$	A^2	$\sqrt{2}AB$	B^2
0	$-\sqrt{2}AB^*$	Z	$\sqrt{2}A^*B$
-1	B^{*2}	$-\sqrt{2}A^*B^*$	A^{*2}
$\mathscr{D}^2_{nm}$	$+2$	$+1$	0
$+2$	A^4	$2A^3B$	$\sqrt{6}A^2B^2$
$+1$	$-2A^3B^*$	$A^2(2Z-1)$	$\sqrt{6}ABZ$
0	$\sqrt{6}A^2B^{*2}$	$-\sqrt{6}AB^*Z$	$\frac{1}{2}(3Z^2-1)$
-1	$-2AB^{*3}$	$B^{*2}(2Z+1)$	$-\sqrt{6}A^*B^*Z$
-2	B^{*4}	$-2A^*B^{*3}$	$\sqrt{6}A^{*2}B^{*2}$

as can be determined from Table 2.6. Furthermore,

$$\begin{aligned} \mathscr{D}^2_{0\pm1} &= \sqrt{3}\mathscr{D}^1_{0\pm1}Z = \mp\sqrt{\frac{3}{2}}(X \pm \mathrm{i}Y)Z \\ \mathscr{D}^2_{0\pm2} &= \frac{\sqrt{6}}{2}(\mathscr{D}^1_{0\pm1})^2 = \frac{\sqrt{6}}{4}(X \pm \mathrm{i}Y)^2. \end{aligned} \tag{2.86}$$

These results are used below.

2.5.3 Expressions for some potential energy functions

A few special cases of $u(\Omega)$ are treated in detail. First, let us look at

$$u(\Omega) = -c^1_0\mathscr{D}^1_{00}(\Omega) = -c^1_0 Z. \tag{2.87}$$

For positive c^1_0 this potential tries to keep the axes $\underline{\boldsymbol{z}}$ and $\underline{\boldsymbol{z}}'$ aligned, penalizing orientations in which $Z = \underline{\boldsymbol{z}} \cdot \underline{\boldsymbol{z}}'$ moves away from $Z = 1$. The expressions (2.59)

in this case reduce to

$$\begin{aligned} -\mathrm{i}J_x u &= \frac{-\mathrm{i}}{\sqrt{2}}\, c_0^1[\mathscr{D}_{01}^1 + \mathscr{D}_{0-1}^1] = -c_0^1 Y \\ -\mathrm{i}J_y u &= \frac{-1}{\sqrt{2}}\, c_0^1[\mathscr{D}_{01}^1 - \mathscr{D}_{0-1}^1] = c_0^1 X \\ -\mathrm{i}J_z u &= 0. \end{aligned} \tag{2.88}$$

where the last equalities follow from Eq. (2.85). Now we consider the potential

$$u(\Omega) = -c_{-1}^1[\mathscr{D}_{0-1}^1(\Omega) - \mathscr{D}_{01}^1(\Omega)] = -\sqrt{2}\, c_{-1}^1 X, \tag{2.89}$$

i.e. $c_1^1 = -c_{-1}^1$. Again, for positive c_{-1}^1, this potential tries to keep the $\underline{\underline{\boldsymbol{z}}}$ and $\underline{\underline{\boldsymbol{x}}}'$ axes aligned. Substitution of $u(\Omega)$ in (2.59) yields

$$\begin{aligned} -\mathrm{i}J_x u &= \frac{-\mathrm{i}}{\sqrt{2}}\, c_{-1}^1[\mathscr{D}_{00}^1 - \mathscr{D}_{00}^1] = 0 \\ -\mathrm{i}J_y u &= -\sqrt{2}\, c_{-1}^1 \mathscr{D}_{00}^1 = -\sqrt{2}\, c_{-1}^1 Z \\ -\mathrm{i}J_z u &= \mathrm{i}\, c_{-1}^1[\mathscr{D}_{0-1}^1 + \mathscr{D}_{01}^1] = \sqrt{2}\, c_{-1}^1 Y. \end{aligned} \tag{2.90}$$

Putting everything together, for the potential

$$u(\Omega) = -c_0^1 \mathscr{D}_{00}^1(\Omega) - c_{-1}^1[\mathscr{D}_{0-1}^1(\Omega) - \mathscr{D}_{01}^1(\Omega)], \tag{2.91}$$

we obtain

$$\begin{aligned} -\mathrm{i}J_x u &= -c_0^1 Y \\ -\mathrm{i}J_y u &= c_0^1 X - \sqrt{2}\, c_{-1}^1 Z \\ -\mathrm{i}J_z u &= \sqrt{2}\, c_{-1}^1 Y. \end{aligned} \tag{2.92}$$

The potential

$$u(\Omega) = -c_0^2 \mathscr{D}_{00}^2(\Omega) = -c_0^2 \frac{1}{2}(3Z^2 - 1) \tag{2.93}$$

favors orientations in which $\underline{\underline{\boldsymbol{z}}}$ and $\underline{\underline{\boldsymbol{z}}}'$ are either parallel or antiparallel ($Z = \pm 1$).

As before, using Eq. (2.86), one finds

$$\begin{aligned} -\mathrm{i}J_x u &= -\mathrm{i}\sqrt{\frac{3}{2}}\, c_0^2[\mathscr{D}_{01}^2 + \mathscr{D}_{0-1}^2] = -3\, c_0^2 YZ \\ -\mathrm{i}J_y u &= -\sqrt{\frac{3}{2}}\, c_0^2[\mathscr{D}_{01}^2 - \mathscr{D}_{0-1}^2] = 3\, c_0^2 XZ \\ -\mathrm{i}J_z u &= 0. \end{aligned} \tag{2.94}$$

Finally, we treat the potential

$$u(\Omega) = -c_2^2[\mathscr{D}_{02}^2(\Omega) + \mathscr{D}_{0-2}^2(\Omega)] = -c_2^2\frac{\sqrt{6}}{2}(X^2 - Y^2), \tag{2.95}$$

i.e. $c_2^2 = c_{-2}^2$. This potential prefers orientations in which $\underline{\boldsymbol{z}}$ is parallel or antiparallel to $\underline{\boldsymbol{x}}'$ ($X = \pm 1$) and disfavors orientations in which $\underline{\boldsymbol{z}}$ is parallel or antiparallel to $\underline{\boldsymbol{y}}'$ ($Y = \pm 1$). We find from (2.59) that

$$\begin{aligned} -\mathrm{i}J_x u &= -\mathrm{i}\, c_2^2[\mathscr{D}_{0-1}^2 + \mathscr{D}_{01}^2] = -\sqrt{6}\, c_2^2 YZ \\ -\mathrm{i}J_y u &= -c_2^2[\mathscr{D}_{0-1}^2 - \mathscr{D}_{01}^2] = -\sqrt{6}\, c_2^2 XZ \\ -\mathrm{i}J_z u &= -2\mathrm{i}\, c_2^2[\mathscr{D}_{02}^2 - \mathscr{D}_{0-2}^2] = 2\sqrt{6}\, c_2^2 XY. \end{aligned} \tag{2.96}$$

Clearly, for the general potential

$$u(\Omega) = -c_0^2\mathscr{D}_{00}^2 - c_2^2[\mathscr{D}_{02}^2(\Omega) + \mathscr{D}_{0-2}^2(\Omega)], \tag{2.97}$$

we simply need to sum the above expressions to obtain

$$\begin{aligned} -\mathrm{i}J_x u &= (-3\, c_0^2 - \sqrt{6}\, c_2^2) YZ \\ -\mathrm{i}J_y u &= (3\, c_0^2 - \sqrt{6}\, c_2^2) XZ \\ -\mathrm{i}J_z u &= 2\sqrt{6}\, c_2^2 XY. \end{aligned} \tag{2.98}$$

CHAPTER 3

PARAMETRIZATION, MD SIMULATION AND ESR SPECTRA OF A NITROXIDE SPIN LABEL ON A POLY-ALANINE α-HELIX

3.1 Introduction

Among the various experimental techniques probing the dynamics of proteins, site-directed spin labeling (SDSL) benefits from using a versatile local reporter that is well tolerated at many sites on soluble and membrane proteins [26]. The continuous wave (cw) electron spin resonance (ESR) spectra of a spin labeled protein are sensitive to molecular motion over a wide range of time scales: from tens of picoseconds to hundreds of nanoseconds. The technique, thus, offers the potential of an extremely rich source of information about biological macromolecules. At the same time, the interpretation of the spectra in terms of detailed protein dynamics is complicated by the internal dynamics of the spin label side chain. To maximally utilize the information present in the spectra, a meticulous understanding of the spin label dynamics becomes necessary.

Over the last decade, Hubbell and co-workers have conducted extensive experimental studies to elucidate the factors affecting the dynamics of nitroxide spin labels on soluble proteins [26, 27, 51, 78, 82, 90, 91]. Of particular interest to this chapter is the work in which 1-oxyl-2,2,5,5-tetramethylpyrroline-3-methyl-methanethiosulfonate (MTSSL) was used as a spin label. Following the general convention, we refer to the amino acid side chain resulting from the reaction of MTSSL with cysteine as R1 (Fig. 3.1). In the majority of the studies T4 Lysozyme (T4L) has served as a model protein system [26, 27, 51, 78, 90, 91]. From this work, site 72 in T4L, situated in the middle of a long five-turn α-helix, has emerged as a

prototypical solvent-exposed helix surface (SEHS) site [26]. The X-band spectra of 72R1, as well as 131R1 (in the middle of a short two-turn helix), show insignificant variation upon alanine mutation of the neighboring $i \pm 3$ and $i \pm 4$ residues [91], suggesting that at these positions R1 interacts only weakly with its neighbors [26]. In spite of this apparent lack of interactions, the spectra of both 72R1 and 131R1 indicate that the conformational freedom of the spin label at those positions is significantly restricted [26, 91]. This ordering was proposed to be due the formation of hydrogen bonds between the disulfide of R1 and the hydrogen of either the backbone amide [91] or the backbone C_α [26]. Put together, the experimental data has been rationalized in terms of the so-called χ_4/χ_5 model for the dynamics of R1 on SEHS sites that are not involved in tertiary contacts [26]. According to the model, the inter-residue immobilization of the disulfide by the backbone effectively locks the conformational transitions about the first two dihedrals, χ_1 and χ_2, of the spin label linker (Fig. 3.1). Since the energetic barrier of the third linker dihedral χ_3—the disulfide torsion angle—is about 7 kcal/mol [63], the internal motion of R1 is assumed to be largely limited to rotations about the last two dihedrals χ_4 and χ_5, hence the name of the model.

The χ_4/χ_5 model motivates and justifies quantitative spectral simulations using the MOMD [4, 27, 28, 44, 50] and SRLS [4, 81] models of Freed and co-workers [80, 94, 106, 107]. In the analytical MOMD/SRLS models, the nitroxide is modeled to undergo anisotropic rotational diffusion in an orienting potential, where the latter is written as a sum of spherical harmonics. Admittedly, such dynamics are intended to correspond to the real spin label dynamics only in an effective, "mean-field" way. Nevertheless, a rough correspondence between the two diffusion coefficients of the MOMD/SRLS model ($D_\perp$ and $D_\parallel$) and rotations about χ_4 and χ_5, has been implied by the χ_4/χ_5 model [27]. As a result, quantitative understanding of the

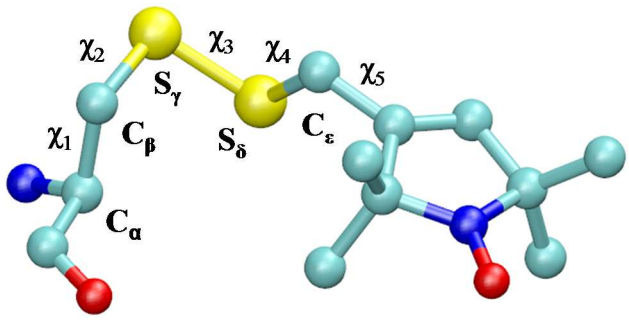

Figure 3.1: The "side chain" R1, resulting from linking MTSSL to a cysteine through a disulfide bond.

dynamics of 72R1 and 131R1 in T4L has been pursued by simultaneous fits of multifrequency ESR spectra with the MOMD/SRLS model [4, 35, 81].

Increasing numbers of studies have recently used atomistic models to gain a deeper insight into the dynamics of R1 by performing molecular dynamics (MD) or Monte Carlo simulations [7, 19, 54, 96, 133, 134]. Potentially, MD simulations can provide access to the detailed motion of the spin label in its heterogeneous environment. Unfortunately, at the present time, exhaustively sampling the conformational space accessible to the spin label is a challenge for MD simulations in which the solvent is treated explicitly. For example, only a few transitions of the R1 dihedrals were observed during 5 and 10 ns simulations of fully solvated spin labeled T4L [134] and Cytochrome *c* [96], respectively. Therefore, to reduce the system size and speed up the simulations, a large majority of the MD studies forgo explicit treatment of the solvent [7, 19, 133]. In addition to replacing the solvent with a continuum dielectric, Monte Carlo search of the R1 conformations [118], and MD simulations at 600 K [7, 133] have been used to achieve greater sampling. Regrettably, a Monte Carlo search strategy does not contain information about

the spin label dynamics, whereas both the dynamics and the populations of the spin label simulated at 600 K are significantly distorted. Ultimately, to assess how relevant the spin label dynamics implied by the molecular models are, ESR spectra should be calculated from the models and, if possible, compared with experiment. Calculations of ESR spectra directly from trajectories require many long trajectories, far beyond what can be currently expected from routine MD simulations of solvated spin labeled proteins. Indeed, an attempt to simulate 9 and 250 GHz spectra from the trajectories of fully solvated T4L has failed [134]. No such attempt has been made in the case of Cytochrome c [96]. As an alternative, Steinhoff and co-workers used the MD simulations to estimate a potential of mean force $U(\Omega)$, where Ω are the Euler angles mapping the nitroxide-fixed coordinate frame to the protein-fixed one, and generated many long trajectories by performing diffusive Brownian dynamics simulations with torques determined by $U(\Omega)$ [7, 133]. ESR spectra were then simulated directly from the Brownian trajectories. Sale *et al.*, on the other hand, assumed that $U(\Omega)$ can be expanded as a sum of spherical harmonics and estimated the expansion coefficients from the MD simulations [19, 119]. Spectra were simulated with the MOMD model using the determined expansion coefficients as input parameters [19, 119].

In another, more recent study the authors refrain from MD simulations altogether [137, 138]. Building on their previous work on spin labeled lipids [20, 21] they propose that the dynamics of R1 on SEHS sites can be rationalized in terms of librations in a few enumerable conformers (rotamers) and exchanges between them. This insightful observation brings the problem of the spin label dynamics to the more familiar realm of internal side chain dynamics in proteins and their manifestation in NMR, ESR and fluorescence [79, 144, 146, 147]. In Ref. [137] the conformational dynamics of R1 on a poly-alanine α-helix was studied in detail.

The absence of steric clashes between the spin label and the helix was used to identify allowed rotamers. The relative probabilities of the rotamers and the rates of exchange among them were estimated from the *ab initio* scans of the torsional potential energies. Based on the high energy barriers and/or large friction opposing the displacement of the bulky spin label, exchanges about χ_1, χ_2 and χ_3 were assessed to be much slower compared to the time scale of standard X-band ESR, providing independent theoretical support for the χ_4/χ_5 model. Due to its simplicity, the approach was suggested as complementary to full MD simulations when insight into the conformational freedom and dynamics of R1 at solvent-exposed sites is sought.

So far, bridging the gap between the atomistic spin label dynamics and the corresponding ESR spectra has been possible only by simplifying the atomistic model, as already discussed above. The degree to which such approximations are justified is presently uncertain. Here, we adopt a different approach and preserve all the atomic detail that a nonpolarizable force field like CHARMM can offer. In an effort to simplify and reduce the problem to its most relevant aspects, we simulate a fully solvated, spin-labeled poly-alanine α-helix, hoping that the dynamics of R1 in this simple system has sufficient bearing on the experimentally well-studied spin label dynamics on SEHS sites. The behavior of the spin label in our MD simulations is expected to be informative about the simplifying assumptions that are safe to make when reduced, stochastic models of the spin label dynamics need to be constructed [7, 19, 118, 119, 133, 137], as in the case of spin-labeled proteins, for which long, all-atom MD simulations might not be feasible.

The chapter is organized as follows: Our methodology is presented in Sec. 3.2. First, the parametrization for a group of four nitroxides is discussed, with particular

emphasis on their electrostatic properties. The energetics of the R1 linker are also examined carefully. Then, we give details about the MD simulations and the calculation of the ESR spectra using the MD trajectories. Section 3.3 contains our results. The conformational dynamics of R1 on a poly-alanine α-helix is analyzed and ESR spectra at 9 and 250 GHz are simulated. The discussion of the results is presented in Sec. 3.4 and our conclusions are given in Sec. 3.5.

3.2 Methods

3.2.1 Force field parameters for four spin labels

Meaningful MD simulations require the use of accurate potential energy functions. The force field parameters pertaining to the nitroxide moiety that were not already present in the official set of CHARMM parameters [87, 121] had to be carefully determined. To ensure their more general validity, four nitroxide model compounds with ring structures based on pyrroline (SLP), pyrrolidine (SLR), oxazolidine (SLT), and piperidine (SLH) were selected for simultaneous parametrization (Fig. 3.2). The first two compounds (SLP and SLR) constitute the rings of the spin labels R1 [91] and R5 [90], respectively, widely used in SDSL studies of proteins [26, 57]. The third model compound (SLT) is a building block for fatty acid and phospholipid spin labels, while the last one (SLH) is itself used as the reporter group TEMPO.

The structures of the four model compounds were optimized with the B3LYP hybrid functional using the standard basis set 6-31G*. This level of theory has been shown to reproduce the experimental geometries of the nitroxides rather well [5].

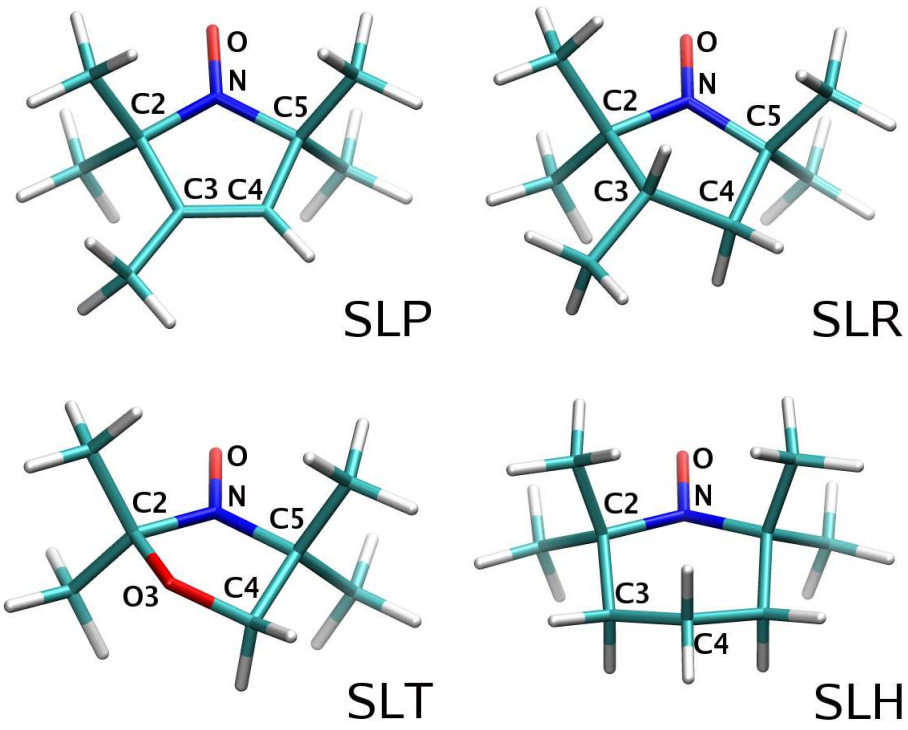

Figure 3.2: Structures and naming convention of the model compounds used in the parametrization.

All the *ab initio* calculations were performed using the program Gaussian 03 [47]. The vibrational frequencies and the normal modes for the model compounds were calculated at the optimized geometries, using B3LYP/6-31G*. A global scaling factor of 0.9806 was used for the calculated frequencies, as recommended in Ref. [124]. The *ab initio* optimized geometries, vibrational frequencies (after scaling) and vibrational modes were used as reference data in the selection of the bonded parameters for the classical force field. In their minimum energy conformations the pyrrolidin and the oxazolidine rings are not planar but prefer a puckered state (Fig. 3.2). Extra effort was exercised to make sure that the various puckered states of those two rings and the energy barriers between them are correctly reproduced with the force field parameters (data not shown).

Partial charges and interaction with water

The partial charges and the Lennard-Jones parameters assigned to the atomic centers need to be optimized carefully so that the nonbonded interactions of the spin label are correctly captured by the force field. Together these two types of parameters determine the nature of the direct interactions of the spin label with its surroundings (e.g. hydrogen bonding and van der Waals contacts), as well as its more global preference for certain types of environment (e.g. aqueous versus hydrophobic). Bearing in mind such considerations, the partial charges were required to reproduce both the overall electrostatic properties of the molecules as well as the more specific hydrogen bonding properties.

To meet the first requirement, the electrostatic potential of each model compound was calculated on a grid of points at B3LYP/aug-cc-pvdz level of theory using the optimized structures. The grid points were generated on five nested Connolly surfaces with scaling factors 1.3, 2.2, 3.0, 5.0 and 6.0, with corresponding densities 2.8, 1.9, 1.3, 0.6 and 0.2 points per Å^2, respectively, chosen in agreement with previous parametrization work of the CHARMM force field [3]. Once the electrostatic potential was calculated, the FITCHARGE module of CHARMM was used to achieve the best fit by varying the atomic partial charges. To be consistent with the existing nonpolarizable CHARMM force field for proteins [87] and lipids [121] the charge on the nonpolar hydrogens was restricted to 0.09 in atomic units. The charge fitting was achieved in two steps. In the first step, the nonpolar hydrogens were assigned a charge of 0.09 and, to keep the molecule neutral, the adjacent carbon atoms were given a charge of -0.09 (methyne carbon), -0.18 (methylene carbon) or -0.27 (methyl carbon). The rest of the atoms were assigned zero charge. Charge fitting with a hyperbolic restraint on the charges—to prevent

Table 3.1: Partial charges for the ring atoms in atomic units.

	O	N	C2	C5	C3/O3	C4
SLP	−0.438	0.220	0.334	0.329	−0.003	−0.340
SLR	−0.433	0.249	0.245	0.267	−0.127	−0.229
SLT	−0.403	0.147	0.406	0.326	−0.336	−0.128
SLH	−0.379	0.167	0.284	-	−0.237	−0.180

their unphysical increase during the fitting—was performed only for the atoms with zero initial charge. All the methyne, methylene or methyl groups, the initial charge of which was already assigned, were excluded from this fit. In the second step a parabolic restraint was applied to keep the charges close to their values of the previous step. In this case, all the atoms, except the nonpolar hydrogens, were included in the fit. The partial charges obtained from this procedure for the ring atoms of the four compounds are given in Table 3.1. The components and magnitudes of the resulting dipole moments are compared with the corresponding *ab initio* values in Table 3.2. The agreement between the two sets is rather satisfactory. Even though the dipole moments of the molecules are slightly overestimated the fitted charges were not scaled down since in a nonpolarizable force field it is desirable to have a dipole moment larger than the one in vacuum.

In the parametrization three new atom types were introduced for the nitroxide oxygen (O) and nitrogen (N), and the doxyl ring oxygen (O3). The Lennard-Jones parameters assigned to the three new atom types were chosen based on the existing CHARMM parameters. To assess the quality of the atomic partial charges and of the Lennard-Jones parameters for the nitroxide oxygen, the interaction of the nitroxide moiety with a water molecule was examined in detail. For each of the four

Table 3.2: *Ab initio* vs. parametrized (in parenthesis) dipole moments (debye).

	SLP	SLR	SLT	SLH
x	1.55 (1.59)	−1.31 (−1.37)	0.78 (0.82)	0.00 (0.00)
y	2.96 (3.02)	3.07 (3.14)	−2.06 (−2.12)	3.10 (3.19)
z	0.00 (0.00)	−0.11 (−0.21)	−0.23 (−0.49)	0.15 (0.24)
tot.	3.35 (3.41)	3.34 (3.43)	2.22 (2.32)	3.11 (3.20)

model compounds the relative orientation of the water molecule with respect to the nitroxide was optimized keeping the structure of the nitroxide and the structure of the water molecule fixed, the former at the B3LYP/6-31G* optimized geometry and the latter at the experimental geometry [8] ($r_{\mathrm{OH}} = 0.9572$ Å, $\theta_{\mathrm{HOH}} = 104.52°$).[1] The optimization was performed using B3LYP/6-311++G**, a level of theory which, reportedly, is sufficient to accurately reproduce hydrogen bond geometries [113]. The energies of the optimized dimers were calculated using B3LYP/aug-cc-pvdz. The interaction energy was calculated by subtracting the energies of the individual molecules from the energy of the dimer. The resulting interaction energy suffers from basis set superposition errors (BSSEs). It is known that the BSSE is larger for MP2 and smaller for B3LYP when used with the same basis set [71]. Based on the water dimer data of Ref. [71], we estimated that the BSSE is less than 0.5 kcal/mol for the aug-cc-pvdz basis set that was used. Considering the uncertainty in the accuracy of the *ab initio* calculation we decided not to correct the interaction energies for the BSSE.

Several structural local minima were identified for each water-nitroxide dimer

[1]Insignificantly different values, $r_{\mathrm{OH}} = 0.9576$Å and $\theta_{\mathrm{HOH}} = 104.51°$, are reported in Ref. [109]. The older values were used in accord with the TIP3P water model [65] used in CHARMM.

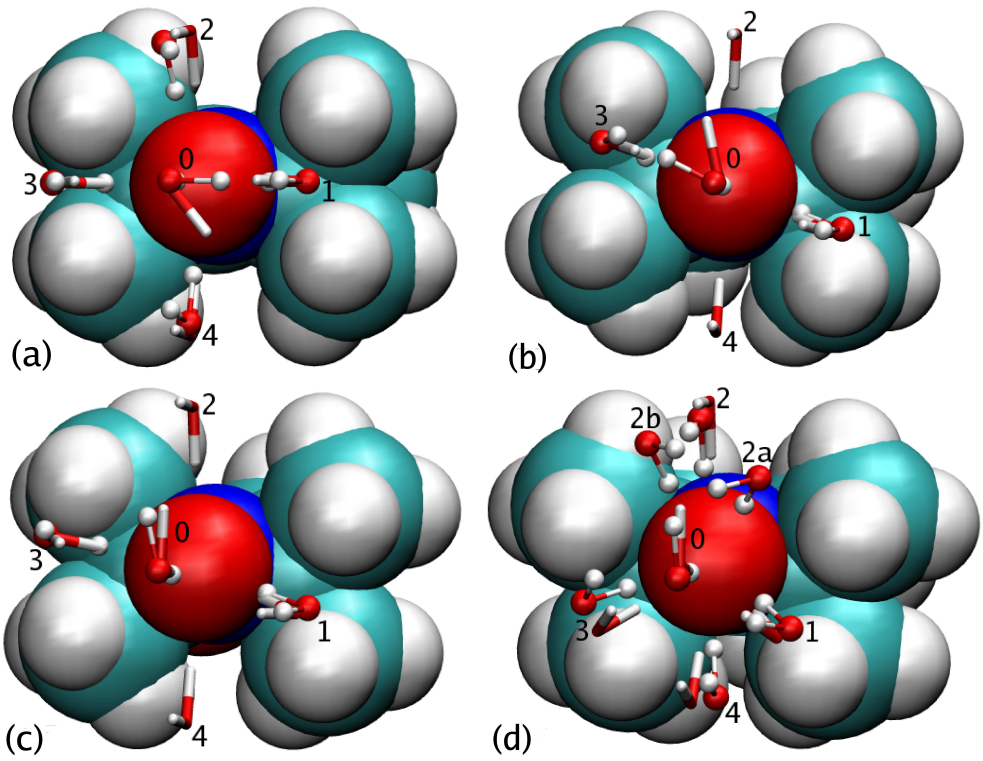

Figure 3.3: Interaction geometries with water for (a) SLP, (b) SLR, (c) SLT, and (d) SLH, optimized with *ab initio* (balls and thin sticks) and with the force field (thick sticks).

(Fig. 3.3). In the *ab initio* calculations, the energetically most favorable conformations are the ones in which the O−H bond of the water lies approximately along the direction of the lone pairs of the nitroxide oxygen (numbered 1 and 3 in Fig. 3.3). Conformations in which the water O−H bond is positioned roughly perpendicularly to the plane of the lone pairs were also found to be local minima (numbered 2 and 4). Their region of attraction is significantly smaller, but present nevertheless, especially for the symmetric nitroxides SLP and SLH. In addition, the geometry in which one of the water hydrogens is along the N−O bond of the nitroxide moiety was also examined by restricting the position of the H-bonding hydrogen to lie on the line along the N−O bond during the optimization (num-

Table 3.3: Interaction energies with water (kcal/mol) and the O$\cdots$H hydrogen bond distance (Å), shown in parenthesis, for the specified conformation.

	SLP	SLR	SLT	SLH
		ab initio		
0	−4.22 (1.99)	−4.35 (1.97)	−3.88 (2.01)	−4.47 (1.97)
1	−6.23 (1.89)	−6.21 (1.90)	−5.92 (1.91)	−5.73 (1.90)
2	−5.35 (1.94)	-	-	−5.38 (1.94)
3	−6.21 (1.89)	−6.20 (1.89)	−5.98 (1.91)	−5.64 (1.91)
4	−5.35 (1.93)	-	−4.91 (1.94)	−5.40 (1.91)
2a				−5.31 (1.92)
2b				−5.35 (1.92)
		param		
0	−5.38 (1.90)	−5.43 (1.91)	−4.91 (1.92)	−5.04 (1.92)
1	−6.12 (1.87)	−6.09 (1.88)	−5.77 (1.89)	−5.52 (1.90)
2	−6.08 (1.88)	−6.15 (1.89)	−5.89 (1.91)	−5.68 (1.92)
3	−6.09 (1.88)	−6.04 (1.88)	−5.75 (1.89)	−5.52 (1.90)
4	−6.08 (1.88)	−6.17 (1.89)	−5.70 (1.89)	−5.67 (1.89)

bered 0). The interaction energies for each of these conformations are listed in Table 3.3, where the distances between the H-bonding water hydrogen and the nitroxide oxygen are also shown in parenthesis.

The numbers in Table 3.3 indicate that with the force field the nitroxide-water interactions are more uniform along the various directions of approach compared to the *ab initio* interactions. For all the model compounds, the force field correctly assigns conformation 0 to be the least favorable. At the same time, the interaction

energy in this conformation calculated with our parameters is about 1 kcal/mol more favorable than the *ab initio* energy. The absence of explicit representation for the oxygen lone pairs in the force field makes the interaction geometries 2 and 4 as favorable as the conformations 1 and 3. This was previously observed in Ref. [5], where lone pair sites for the nitroxide oxygen were introduced in order to reproduce this structural feature with a molecular mechanics force field. Here, we choose to keep the nitroxide oxygen as a point charge and not introduce additional lone pair sites. As a result of this simplification the hydrogen bonding geometry is expected to be slightly off. Nevertheless, in the context of dynamics, one might suspect that thermal agitation will render these structural effects less important. Since the hydrogen bonding energies are within one to two $k_{\mathrm{B}}T$, at room temperature, over the whole range of hydrogen bonding geometries, the energetics of the force field should be appropriate.

Scan of the linker dihedral angles of R1

Rotations about the bonds connecting the nitroxide ring to the protein backbone constitute an intuitive way of rationalizing the dynamics of the spin label side chain R1 [27,78,90,91,137]. To make sure that the simulated linker dynamics proceed on the correct energy surface, a scan of the dihedral energy was performed. Restricted optimizations and single point energy evaluations were carried at the B3LYP/6-31G* and B3LYP/aug-cc-pvdz levels of theory, respectively, for the torsion angles of interest, taking values on a two dimensional grid. The grid points were separated by 30°, in the interval $(-180°, 180°)$. The χ_1–χ_2 energy surface was explored using the construct shown in Fig. 3.4. The two linker dihedrals χ_1 (N–CA–CB–S1) and χ_2 (CA–CB–S1–S2) were constrained during the optimization. In addition, the "backbone" atoms were fixed in an α–helical conformation. The procedure was

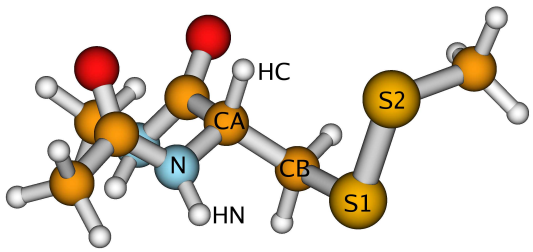

Figure 3.4: Energetically most favorable conformation on the χ_1–χ_2 energy surface, $(\chi_1, \chi_2, \chi_3) = (-60°, -60°, -90°)$. The distance $d_{\mathrm{S1-HN}} = 2.81$ Å and the angle $\theta_{\mathrm{S1-N-HN}} = 57°$. In addition, $d_{\mathrm{S2-HC}} = 3.03$ Å and $\theta_{\mathrm{S2-CA-HC}} = 55°$.

carried separately for $\chi_3 \approx -90°$ and $\chi_3 \approx 90°$. The χ_5–χ_4 energy surface was examined using the construct in Fig. 3.5. Only the values of χ_5 (S2–C–C3–C4) and χ_4 (S1–S2–C–C3) were fixed during the optimization. All the other degrees of freedom were allowed to relax. The resulting energy surfaces are shown in Figs. 3.6 and 3.7. The corner of every small rectangle in the plots is an *ab initio* optimization and energy evaluation data point. The *ab initio* surfaces are in the columns on the left, the scans with the standard force field energy function, in which the energetics of each torsion are independent of the other torsions, are in the middle column (param).

Comparison of the first two columns in Fig. 3.6 shows that the parametrization captures the positions of the minima on the χ_1–χ_2 surface rather well. The relative depths of the minima, on the other hand, are not reproduced satisfactorily. (Since what is meaningful is the energy difference and not the absolute value of the energy, the minimum energy for each surface was set to zero and used as an offset for the other energies.) Whereas the *ab initio* calculation indicates that $(\chi_1, \chi_2) = (-60°, -60°)$ is a global minimum for $\chi_3 \approx -90°$, the best that could be achieved by varying the force field parameters for the dihedrals led to two additional, almost

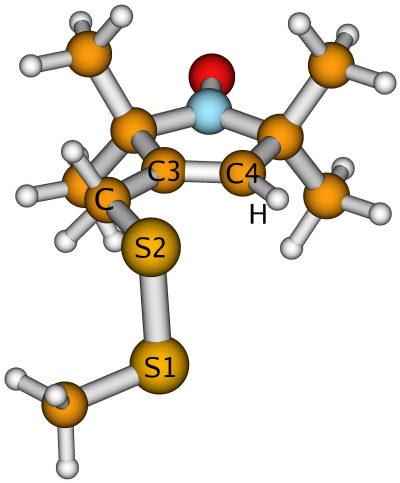

Figure 3.5: The $\chi_5 = 0°$, $\chi_4 = -90°$, $\chi_3 \approx -90°$ conformation of R1. The distance between S2 and the hydrogen attached to C4 is 2.87 Å, $\theta_{\mathrm{S2-C4-H}} = 62°$; $d_{\mathrm{S1-H}} = 3.67$ Å and $\theta_{\mathrm{S1-C4-H}} = 61°$.

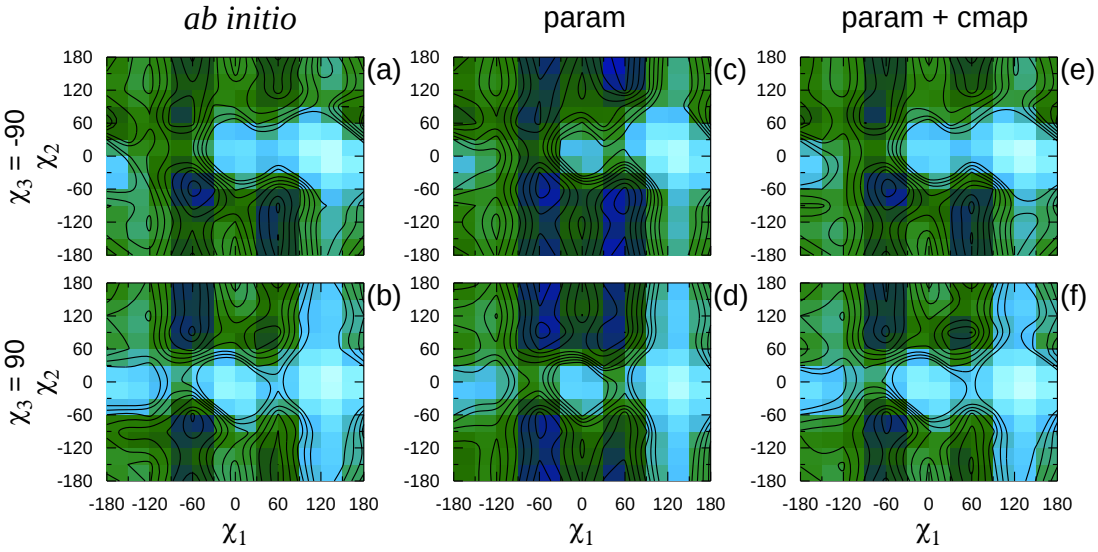

Figure 3.6: *Ab initio* scan of the χ_1–χ_2 potential energy surface. The contours are drawn for every 1 kcal/mol change in energy. Dark regions indicate low energy, light regions correspond to high energy.

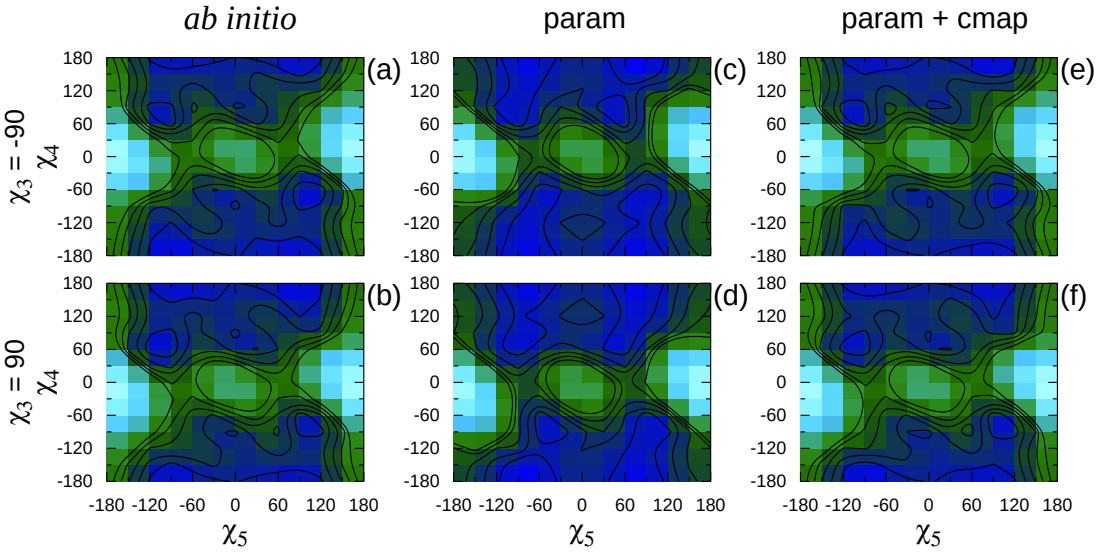

Figure 3.7: Same as Fig. 3.6 for χ_5–χ_4.

equally deep minima at $(60°, -60°)$ and $(60°, 180°)$. According to the *ab initio* energies, these two conformations should lie, respectively, about 1 and 2 kcal/mol higher than the global minimum. The *ab initio* optimized structure for the global minimum is shown in Fig. 3.4, where one of the sulfurs (S1) is seen to be in the vicinity of the backbone amide hydrogen (HN), the other (S2), close to the hydrogen of the C_α (HC). Both of the implied sulfur-hydrogen interactions have been invoked to rationalize the apparent adsorption of the disulfide to the helix backbone [26, 91]. Therefore, it is very important to account for their energetics. The absence of the sulfur lone pairs in the force field and the small partial charge of the sulfur makes it impossible to recreate these favorable interactions naturally. We decided to use the grid based correction map (CMAP), recently introduced in the CHARMM force field [88], to impose the desired *ab initio* energy on the two dimensional χ_1–χ_2 energy surface, thus introducing a coupling between these two torsions. The CMAP grid was calculated by averaging the corrections necessary

for the $\chi_3 \approx -90°$ and $\chi_3 \approx 90°$ conformations. The energy surfaces obtained using CMAP are shown in Fig. 3.6 (param+cmap). As seen, the agreement with the *ab initio* energy surfaces is almost perfect.

In the case of the χ_5–χ_4 energy surfaces in the first two columns of Fig. 3.7, the best parameters with independent χ_4 and χ_5 failed to reproduce not only the relative depths but also the positions of the minima. For $\chi_4 \approx 180°$ the multiplicity of χ_5 is seen to be two, with minima at about $-90°$ and $+90°$. With the force field, the positions of these two minima basically persists for $\chi_4 \approx \pm 90°$, whereas according to the *ab initio* calculations one of the minima should shift to $\chi_5 \approx 0°$. The optimized structure at $(\chi_5, \chi_4) = (0°, -90°)$ is shown in Fig. 3.5, where it is apparent that the force field fails to account for the favorable interaction between the sulfur S2 and the polar hydrogen H. The fact that this conformation has a slightly lower energy than the $(0°, 180°)$ conformation in which S1 lies away from the nitroxide ring, is a clear indication that the lone pairs of the sulfur are involved in the interaction. As before, the sulfur representation in the force field does not allow us to take such effects into account. Therefore, we decided to use the CMAP correction for the χ_5–χ_4 energy surface as well (the right most column of Fig. 3.7), which led to a rather good agreement with *ab initio*.

3.2.2 MD simulation details

Simulations of R1 attached to a poly-alanine α-helix were performed using CHARMM. The simulated helix consisted of 14 alanines and a single spin labeled cysteine at its central position. The helix was solvated with 686 TIP3P water molecules. The resulting system of of 2247 atoms filled a tetragonal simulation box with starting side lengths of 26.0, 26.0 and 34.0 Å. Periodic boundary

conditions were used. The electrostatics were treated with particle mesh Ewald summation. Pressure and temperature pistons were used to achieve an NpT ensemble at $T = 297$ K and $p = 1$ atm. To prevent the unfolding of the helix in water the first five and the last five residues were harmonically restrained to their starting positions with force constants of 0.5 kcal/mol/Å^2.

According to the χ_4/χ_5 model, the first three dihedrals of R1 should rarely undergo transitions. Therefore, considering their multiplicity (χ_1:3, χ_2:3, χ_3:2), we decided to have each of the 18 possible conformations as starting conditions for the simulations. Thus 18 systems, each one starting at a different conformation, were simulated. Below we refer to these trajectories as a1, a2, a3, etc. and b1, b2, etc., where 'a' and 'b' indicate that the trajectory was initiated with $\chi_3 \approx -90°$ and $\chi_3 \approx 90°$, respectively. The simulations were equilibrated for 500 ps. During the equilibration a flat bottom Saxon-Wood potential was used to restrict each of the first three dihedrals to remain in their initial state, while the last two dihedrals were free to explore different conformations. After the equilibration the Saxon-Wood potentials were removed and only the harmonic restraints on the backbone atoms of the first five and last five residues remained. Each of the 18 systems was simulated for 101 ns. The first ns was not considered in the analysis. Snapshots of the simulations were saved every 1 ps.

3.2.3 ESR spectra simulation details

The numerical integrators for the quantal spin dynamics and for the classical rotational diffusion, developed in Ch. 2, allow us to easily model the effect of the global protein tumbling in addition to the spin label dynamics coming from the MD simulations. This is necessary for the qualitative comparison of the simulated spectra

of R1 on a poly-alanine α-helix with the experimentally available data of T4L. For the rotational diffusion coefficient of T4L in water we used $D = 18 \times 10^6$ s^{-1}, which had been obtained in a multifrequency fit to spectra recorded at 22°C [81] with the SRLS model [80]. The viscosity of the nonpolarizable TIP3P water model used in the MD simulations is 2.86 times smaller than the viscosity of water [43, 148], implying that the solvent in the simulations moves about 2.5 times faster than it should. Since the spin label on the poly-alanine helix is largely solvent exposed, its dynamics are also expected to be faster to a similar degree. To correct for the low solvent viscosity, the time axis of the MD trajectories was stretched by a factor of 2.5. Because T4L is a relatively small protein, its tumbling in solution is fast enough to narrow the spectral lines at 9 GHz. To slow down the tumbling of T4L and reduce its effect on the spectra, it is a common practice to use 30 wt % sucrose solution, which is about 3.3 times more viscous than an aqueous solution with no sucrose. Since the rotational diffusion coefficient is inversely proportional to the viscosity, we estimated that $D = 6 \times 10^6$ s^{-1} under such conditions. The viscosity of the solution is expected to affect not only the tumbling of the protein but also the dynamics of the spin label itself. Thus, to compare with experimental spectra in 30 wt % sucrose, the time axis of the trajectories was stretched by a factor of eight ($8 \approx 2.5 \times 3.3$). The stretch factors, the diffusion coefficients and the respective correlation times are summarized in Table 3.4.

When MD trajectories are used as explicit realizations of the randomness affecting the quantum Hamiltonian, it is beneficial to average the magnetic tensors along the MD trajectories over the time step Δt appropriate for the quantum dynamics. Two such time steps, suitable for $B = 0.34$ T (9 GHz) and $B = 8.92$ T (250 GHz), are given in the second column of Table 3.5. The snapshots from the MD simulations are available every $\delta t = 1$ ps. Dividing Δt by δt and by 2.5—the

Table 3.4: Scaling factor for the time axis and rotational diffusion coefficient of T4L used in the spectral simulations in Sec. 3.3. The relaxation time $\tau = 1/6D$ is also shown.

solvent	stretch	$D \times 10^6$ (s^{-1})	τ (ns)
water	2.5	18	9.3
30 (w/w) % sucrose	8.0	6	27.8

factor accounting for the larger diffusion coefficient of water in the simulations—gives the number of MD frames to be averaged over (avgN). Similarly, one can obtain the 'avgN' values for no stretch at all, or for a stretch by a factor of eight (given in parenthesis). It may be noted that the integration of the quantum dynamics can be initiated from different points along the MD trajectory, since the origin of time is arbitrary. The starting time instances were chosen to be separated by 2 ns, which corresponds to 'lagN' number of Δt steps. The last two columns in Table 3.5 list the number of spherical grid points (sphN), used for the initial conditions of the isotropic diffusion, and the Gaussian broadening introduced in the calculation of the spectra (T_{G}^{-1}). The magnetic tensors,

$$\begin{aligned} \mathsf{g}^{\mathtt{N}} &= \mathrm{diag}(2.00809, 2.00585, 2.00202) \\ \mathsf{A}^{\mathtt{N}} &= \mathrm{diag}(6.2, 4.3, 36.9), \end{aligned} \tag{3.1}$$

corresponding to the experimentally determined values for 72R1 on T4L,[2] were used in the spectral simulations.

[2]Ziwei Zhang and Jack H. Freed, unpublished results.

Table 3.5: Parameters used in the simulation of the spectra in Figs. 3.12 and 3.13. Additional Lorentzian broadening of 0.3 G was introduced in all the simulations.

field (T)	Δt (ns)	avgN	lagN	sphN	T_{G}^{-1} (G)
0.34	2.0	800^a (250^b)	1	400^d	1.0
8.92	0.25	100^a (250^c)	8	12800^d	2.0

[a]2.5-fold stretch of the time axis.
[b]8-fold stretch of the time axis.
[c]The time axis is not stretched.
[d]Twice as many points were used for the $D = 0$ simulation.

3.3 Results

3.3.1 Conformational dynamics of R1 on a poly-alanine α-helix

A striking feature of all the MD trajectories is the large number of transitions for each of the dihedral angles of the spin label. Even the disulfide torsion χ_3, which has the highest energy barrier among all the dihedral angles, changes its conformation ten times across all the 18 trajectories (Table 3.6). The two transitions in trajectories a3 and b9 are separated by 27 and 19.3 ns, respectively, and therefore, are most likely independent. (See Sec. 3.2.2 for the naming convention of the trajectories.) Figure 3.8 shows a 20 ns window of the evolution of the five dihedral angles of trajectory b1. This trajectory undergoes one χ_3 transition (Fig. 3.8(e)). The traces in Fig. 3.8, and all the other traces which are not shown here, indeed seem to confirm that the dynamics of R1 on a poly-alanine α-helix can be rationalized in terms of librations in discrete number of states with occasional

Table 3.6: Number of conformational transitions for χ_3 observed in the MD trajectories.

traj. #	1	2	3	4	5	6	7	8	9
a	0	0	2	0	0	0	0	0	0
b	1	0	1	1	0	1	1	1	2

exchange between them, as proposed by Tombolato *et al.* [137].

Interestingly, in Fig. 3.8 we see transitions of χ_1 and χ_2 lasting from less than 1 ns to several nanoseconds—time scales which by no means are slow on the ESR time scale. In addition, the transitions of these dihedrals appear to be largely coupled. For example, the short-lived second transition of χ_1 happens simultaneously with a transition of χ_2. At the last transition of χ_1 not only χ_2 but also χ_4 changes its conformation. As expected from the low energy barriers separating its conformational minima (Fig. 3.7), the fifth dihedral χ_5 undergoes rapid transitions (Fig. 3.8(d)). At the same time, a concerted transition involving χ_2, χ_4 and χ_5, shortly after the 55th nanosecond in Fig. 3.8, locks the conformation of the spin label for almost 5 ns, providing an example of how in simulations extending for 5–10 ns it might be possible to have none or very few transitions of all the linker dihedrals, in spite of the low potential energy barrier of χ_5. Clearly, in this case, full account of the interactions of the spin label with its immediate environment is necessary.

Let us now try to identify the relevant rotamers of R1 and their populations. A given snapshot from the MD trajectories can be assigned to a rotamer in several different ways. One option is to define the rotamers by a set of reference dihedral angle values χ_i and fluctuation windows $\pm\Delta\chi_i$ about them ($1 \leq i \leq 5$). Such

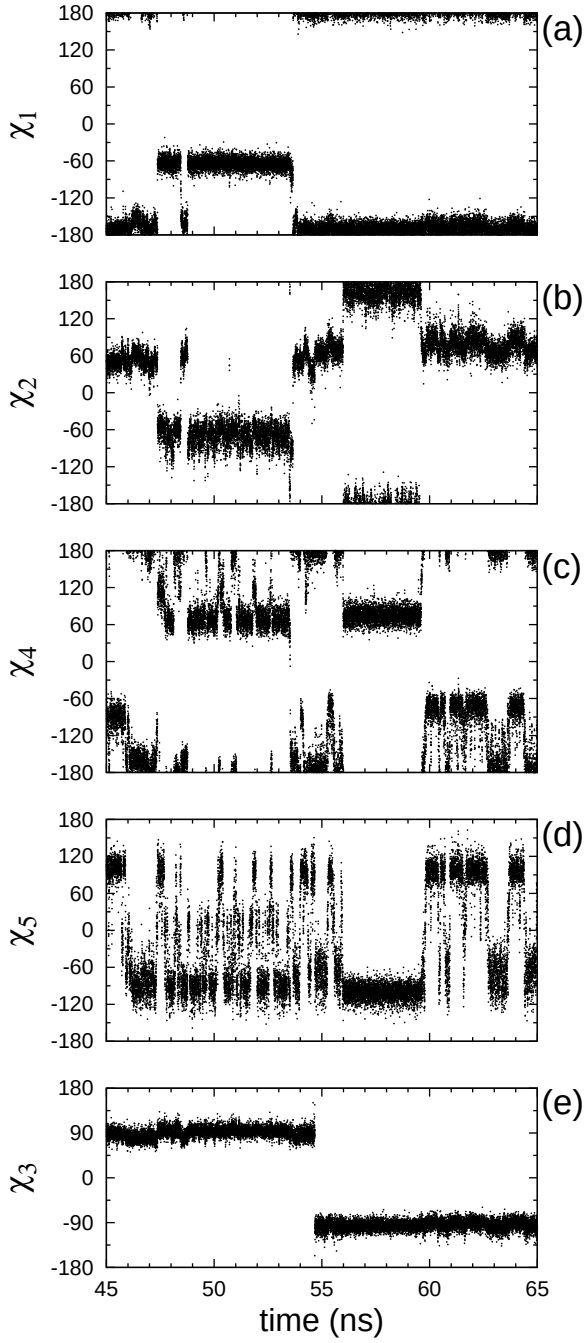

Figure 3.8: Evolution of dihedral angles in the time interval between 45 and 65 ns for trajectory b1.

Table 3.7: Minima of the R1 linker dihedrals (in degrees) used to define its rotameric states in Ref. [137]. The multiplicity of each torsion is in parenthesis.

$\chi_1(3)$	$\chi_2(3)$	$\chi_3(2)$	$\chi_4(3);\chi_5(2)$
$-60, +65, 180$	$\pm 75, 180$	± 90	$(\pm 75; \pm 8, \mp 100), (180, \pm 77)$

reference values and fluctuation estimates were given in Ref. [137] for $T = 298$ K, based on the *ab initio* energy profiles of the R1 dihedrals, and are listed in Tables 3.7 and 3.8. Only 3.5% of all the MD snapshots fall into the conformational volume covered by this definition of rotamers. Even in this case, we find that 65 different rotamers, out of the 108 possible, are visited in the MD simulations. A larger fraction of the MD snapshots gets assigned to some rotamer when the width of the fluctuation window is increased. When 80% of the data is assigned the trajectories visit 96 out of the 108 possible rotamers (Table 3.8). An alternative counting scheme is to use the reference rotamer angles from Table 3.7 as flagpoles and assign a given MD snapshot to the closest flagpole, according to an Euclidean distance metric. This strategy has the advantage of pairing every data point with a rotamer. According to this "minimum distance" criterion, the MD snapshots visit 102 rotamers (Table 3.8).

In spite of the large number of visited rotamers, it might be that the spin label visits most of these conformations only transiently and spends the more significant part of its time in a few rotamers. To evaluate this possibility we calculate the occupation probabilities of the visited rotamers using the minimum distance criterion. The 18 most populated rotamers are ranked in Table 3.9. Indeed, the populations reveal that the spin label spends about a third of its time in only three rotamers (m1, m2 and m3), briefly visiting all the other tens of rotamers.

Table 3.8: Fluctuations (in degrees) about the conformations defined in Table 3.7, together with their percent coverage of all the MD snapshots and the number of visited rotamers.

$\Delta\chi_1$	$\Delta\chi_2$	$\Delta\chi_3$	$\Delta\chi_4$	$\Delta\chi_5$	%	# rot.
8.5^a	12.5^a	8.5^a	12.5^a	$(12.5^a)(25^b)$	3.5	65
30	30	45	30	(30)(45)	59.3	90
40	40	60	40	(40)(60)	80.0	96
		minimum distance			100.0	102

[a]Values estimated in Ref. [137] for $T = 298$ K.
[b]Reference [137] comments that this fluctuation should be larger than 12.5° but does not specify a numerical value.

At this point, it is important to stress that only ten transitions were observed for the dihedral angle χ_3 across all the trajectories. (For brevity, we refer to conformations with $\chi_3 \approx -90°$ as 'm', and conformations with $\chi_3 \approx +90°$ as 'p'.) The fact that there were two p $\rightarrow$ m and eight m $\rightarrow$ p transitions suggests that the p conformer is less populated. However, the exact ratio of the two populations is largely uncertain, implying that the absolute ranking of the m and p rotamers (Table 3.9) is also uncertain. Since more transitions were observed for the other dihedrals (for a given conformation of χ_3) it is safer to assume ergodicity in those cases. Taking into account this limitation, we analyze the two conformations of the disulfide separately. The populations of the rotamers conditioned on the state of χ_3 are given in parenthesis in Table 3.9. From the numbers it becomes clear that the conformational freedom of the m and p states is quite different: Whereas only three rotamers (m1, m2 and m3) represent 50% of all the m conformations it takes six rotamers (p1, p2, p3, p4a, p4b, and p5) to cover the same percentage of the p states.

Table 3.9: Most populated 18 rotamers ranked according to their populations. The populations conditioned on the state of χ_3 are given in parenthesis.

rot.	χ_1	χ_2	χ_3	χ_4	χ_5	prob. (%)	Ref. [137][a]
m1	−60	180	−90	180	−77	13.3 (20.8)	-
m2	−60	180	−90	180	77	10.3 (16.1)	-
m3	−60	−75	−90	75	−100	8.4 (13.1)	-
p1	−60	−75	90	180	77	4.5 (12.5)	-
m	180	180	−90	75	−100	3.7 (5.7)	-
p2	−60	−75	90	75	−100	3.6 (10.0)	-
m	−60	−75	−90	180	77	3.6 (5.7)	C1
m	180	75	−90	180	−77	3.0 (4.6)	-
p3	−60	180	90	180	−77	2.7 (7.6)	C6
p4a	−60	180	90	−75	100	2.6 (7.2)	-
p4b	−60	−75	90	180	−77	2.6 (7.2)	-
p5	−60	180	90	180	77	2.5 (6.9)	-
m	−60	−75	−90	180	−77	2.5 (4.0)	C2
m	180	180	−90	180	77	2.4 (3.7)	C9
m	180	−75	−90	180	77	2.0 (3.1)	-
p	−60	−75	90	75	8	1.9 (5.4)	-
p	180	75	90	−75	100	1.9 (5.3)	-
m	180	75	−90	−75	100	1.7 (2.7)	-

[a]The complete list of the 18 relevant rotamers according to Ref. [137] is given in Table 3.11.

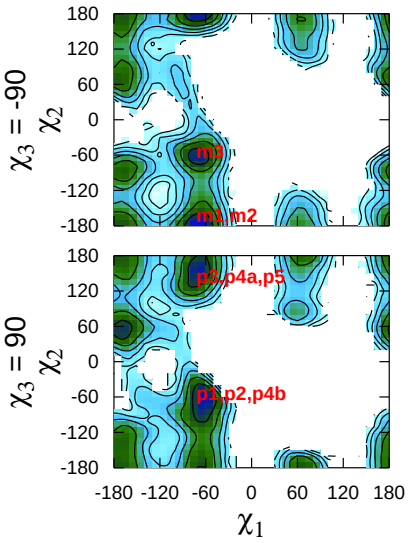

Figure 3.9: The χ_1–χ_2 free energy surface computed from the MD trajectories for the two conformations of the disulfide dihedral. The contours correspond to an energy change of 1 kcal/mol. Regions not visited during the simulations are left white.

The positions of the most populated rotamers are indicated on the χ_1–χ_2 and χ_5–χ_4 free energy surfaces calculated from the trajectories (Figs. 3.9 and 3.10). The *ab initio* χ_5–χ_4 maps were virtually identical for the two χ_3 conformers (Fig. 3.7). In the context of the helix this is no longer the case (Fig. 3.10). The presence of the helix also restricts the conformational space accessible to the first two dihedrals (cf. Figs. 3.6 and 3.9). The $(\chi_1, \chi_2) = (-60°, -60°)$ conformation was suggested as the most likely for R1, based on crystal structures of spin labeled T4L [78]. Indeed, it was observed in four out of the six spin label conformations not involved in crystal contacts [44, 78]. The free energy surfaces in Fig. 3.9 are in agreement with that observation. At the same time, they indicate that other minima, namely $(-60°, 180°)$ for both m and p and $(180°, 60°)$ for the p states only, are also very likely. In fact, the latter minimum corresponds to the other two spin label conformations observed in the crystal structures [44, 78].

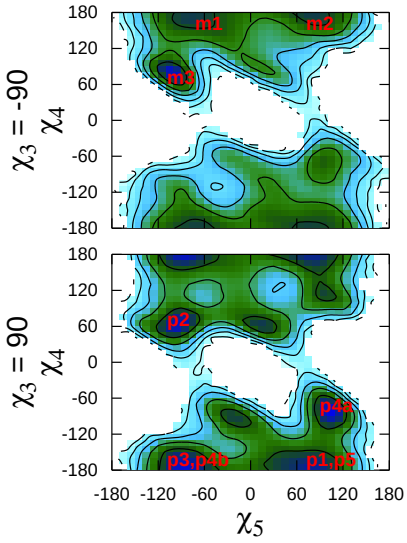

Figure 3.10: Same as Fig. 3.9 for χ_5–χ_4.

To visualize the difference in the configurational space accessible to the spin label in the two conformations of the disulfide torsion, the positions of the nitroxide N and O atoms along the trajectories were mapped onto a cubical grid. The vertices of the grid were separated by 0.3 Å. The grid cells populated by the N–O bond are shown in Fig. 3.11 for the m (left) and p (right) conformations. The N–O bond of the spin label spends 50% of its time within the colored volumes. The difference in the configurational volume accessible to the two conformers is striking. The spin label is seen to be much more restricted in its m states, tending to dwell as close as possible to the $i-3$ and $i-4$ or $i+3$ and $i+4$ residues of the helix. While interactions with the $i-3$ and $i-4$ residues appear to be as important when R1 is in the p conformations, the contacts with residue $i+4$ do not seem to be as favorable. For the p states there are two additional regions easily accessible to the spin label: the broad region around residue $i-1$ and the smaller region on the opposite side. For each of the most populated rotamers, we quantify the strength of the spin label-helix interaction by calculating the average van der Waals

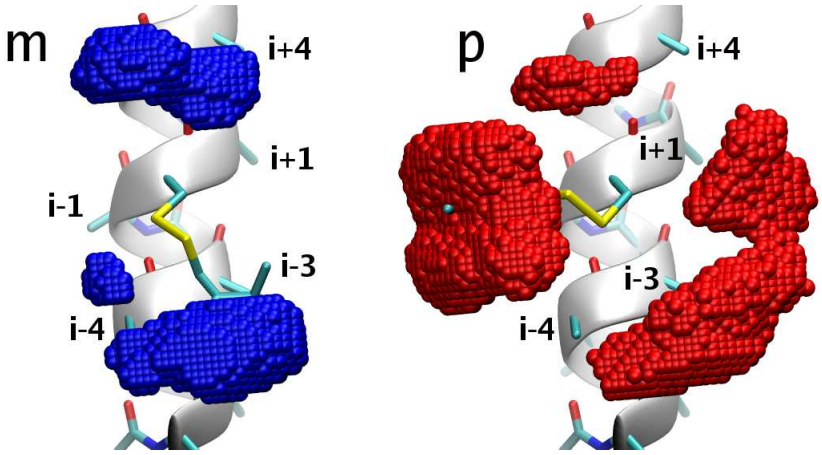

Figure 3.11: Volumes inside which the N–O bond spends 50% of its time in the m (left) and p (right) conformers of R1.

interaction energies between all the C and H atoms on the nitroxide, beyond the disulfide, and the side chain atoms of the alanines at positions $i \pm 4$, $i \pm 3$ and $i \pm 1$ (Table 3.10). Although the energies of the strongest contacts are only equal to $k_{\mathrm{B}}T$ at room temperature, some rotamers are seen to establish two or three such contacts, which leads to interaction energies up to two times stronger than the thermal energy. As already suspected from Fig. 3.11, the energies confirm that the most considerable difference between the m and p states of the spin label is the interaction with side chains at positions $i-1$ and $i+4$. The former is energetically most favorable for $\chi_3 \approx 90°$ but is irrelevant for $\chi_3 \approx -90°$, whereas the opposite is true for the latter. Looking at Fig. 3.11 and using the information in Table 3.10, it is hard to predict to what extent and in what direction mutations at the various neighboring sites of R1 will affect its ordering. The exact outcome will be sensitive both to the possibility of interaction with the new side chain and to the energy of that interaction.

Table 3.10: van der Waals interaction energy (kcal/mol) between R1 in the given rotamer and the side chains at positions $i \pm 1$, $i \pm 3$ and $i \pm 4$. Energies larger than half $k_{\mathrm{B}}T$ at room temperature are bold.

	$i-4$	$i-3$	$i-1$	$i+1$	$i+3$	$i+4$
m1	**−0.64**	**−0.61**	−0.05	−0.06	−0.05	−0.06
m2	**−0.64**	**−0.60**	−0.05	−0.06	−0.05	−0.06
m3	−0.09	−0.12	−0.05	−0.13	**−0.45**	**−0.53**
p1	**−0.31**	−0.15	**−0.44**	−0.07	**−0.41**	−0.11
p2	**−0.35**	−0.11	**−0.52**	−0.05	**−0.42**	−0.08
p3	−0.25	**−0.40**	−0.14	−0.16	−0.16	−0.16
p4a	−0.19	**−0.37**	−0.13	−0.18	−0.18	−0.18
p4b	**−0.32**	−0.15	**−0.44**	−0.07	**−0.38**	−0.10
p5	−0.24	**−0.40**	−0.13	−0.17	−0.16	−0.17

3.3.2 Simulating ESR spectra using the MD trajectories

The test for the similarity of the simulated and the real dynamics of R1 is the comparison between spectra calculated using the MD trajectories and experimental spectra. Since poly-alanine does not retain perfect α-helical structure in water, any quantitative comparison with experimental spectra is not realistic. Instead, the qualitative similarities and differences of the calculated spectra with spectra from the prototypical SEHS sites 72R1 and 131R1 on T4L will be considered. Calculated spectra at $B_0 = 0.34$ T for three different diffusion rates are shown in Fig. 3.12(a). At the top is the powder spectrum for which the dynamics are entirely due to the MD trajectories ($D = 0$). The lower two spectra include isotropic rotational diffusion, with the specified diffusion coefficient, in addition

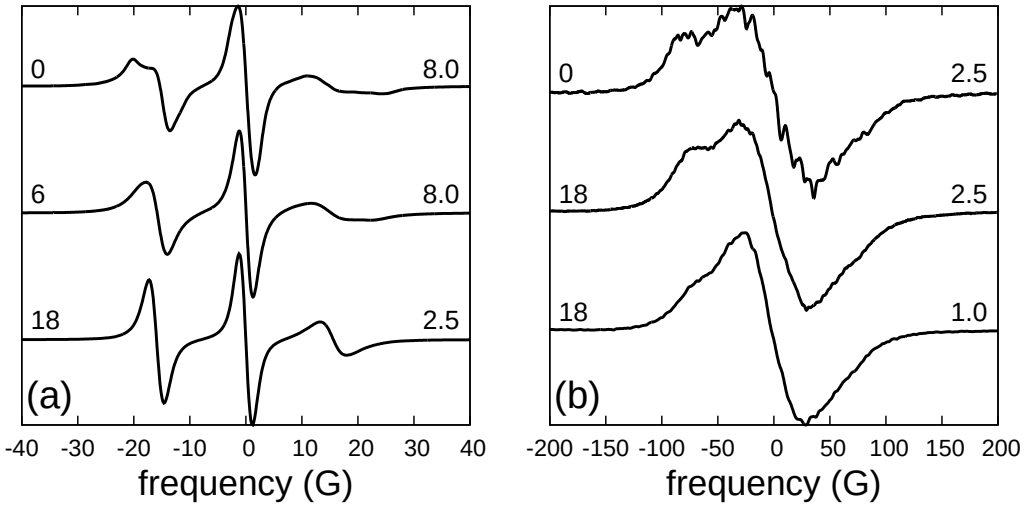

Figure 3.12: (a) $B = 0.34$ T and (b) $B = 8.92$ T spectra simulated from the MD trajectories without ($D = 0$) and with ($D = 6\times$ and 18×10^6 s^{-1}) additional tumbling. The diffusion coefficient is indicated on the left, and the scaling factor on the right hand side of each spectrum. Other simulation parameters are given in Table 3.5.

to the dynamics coming from the MD trajectories. Both the $D = 6 \times 10^6$ s^{-1} (slow) and $D = 18 \times 10^6$ s^{-1} (fast) spectral lines are significantly narrower than the experimental lines for 72R1 and 131R1, recorded respectively with [91] or without [81] sucrose. This indicates that R1 on a poly-alanine α-helix is less ordered and more mobile (in the time window of the 9 GHz experiment) than it is at these two positions in T4L. Comparison of the top two spectra in Fig. 3.12(a) demonstrates that the tumbling of T4L has a non-negligible effect on the 9 GHz spectrum, even in 30 wt % sucrose solution.

Spectra at higher frequencies are less sensitive to slow dynamics in the time window from a few nanoseconds to tens of nanoseconds. Instead, they become progressively more influenced by faster motions on time scales from tens of picoseconds to a few nanoseconds. At 250 GHz (8.92 T) the effect of the rotational

diffusion of a protein like T4L on the spectrum is substantially diminished, as can be seen by comparing the top two spectra in Fig. 3.12(b). (The $D = 0$ spectrum is quite noisy even though twice as many stochastic+MD trajectories were used in its simulation.) As evident from the difference between the bottom two spectra in Fig. 3.12(b), the scaling of the time axis of the MD trajectories, used here to account for the different viscosities of the simulated and real solvent, has a substantial effect on the spectrum. What the correct scaling should be is not immediately clear in general. The situation in which R1 is almost entirely solvent exposed corresponds to one of the extremes. The other is a buried spin label for which there should be no scaling at all. The scaling for a partially solvent-exposed spin label should fall in between those two. It is conceivable to leave the scaling as a fitting parameter when quantitative agreement with experimental spectra is the goal.

The m and p conformations of R1 on a poly-alanine α-helix were drastically different in terms of their conformational freedom. To assess the effect of this difference on the spectra, the trajectories were partitioned into segments in which R1 was either in one or the other conformation. This resulted in 17 m segments and 11 p segments of variable duration, as can be inferred from Table 3.6. 67% of all the snapshots fell into the first, and 33% into the second group. Spectra at 0.34 and 8.92 T, simulated using these segments, are shown in Fig. 3.13 (m and p), where they are compared with spectra simulated using the entire trajectories (all). Since, the m:p ratio is not necessarily represented correctly in the MD simulations, one can look at the m and p spectra as bracketing the range of spectral lines that correspond to different mixtures of the two components. From that point of view, the spectra simulated using the complete MD trajectories ('all' in Fig. 3.13) happen to be one such example. The two humps in the m spectrum at 250 GHz (Fig. 3.12(b)) very much resemble the humps seen in the spectrum of 72R1 [81],

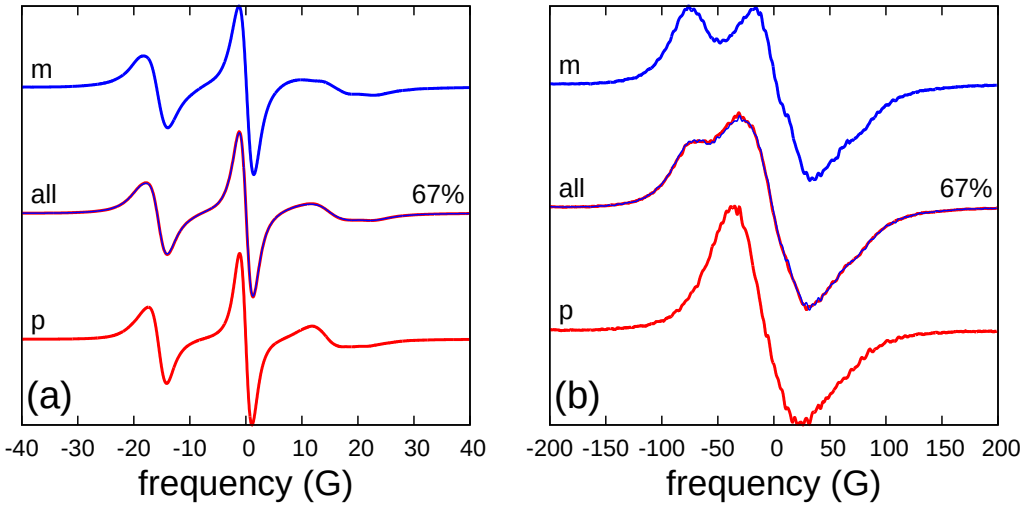

Figure 3.13: Spectra simulated using all the MD trajectories or only their m and p segments, as indicated. (a) $B = 0.34$ T, $D = 6 \times 10^6$ s^{-1} (with an 8-fold scaling of the time axis), (b) $B = 8.92$ T, $D = 18 \times 10^6$ s^{-1} (with 2.5-fold scaling).

whereas the shoulder in the 'all' spectrum is more like the 250 GHz spectrum of 131R1 [81]. This is in spite of the fact that the lines in all the 9 GHz spectra (Figs. 3.12 and 3.13) are much sharper than the corresponding lines of either 72R1 or 131R1. Interestingly, by going from the 'all' ensemble of spin labels to its more ordered subset 'm' we seem to go from a 131R1-like to a 72R1-like spectrum at 250 GHz.

Given that the exchanges between the m and p conformations are very rare, the effect of the exchange rate is expected to be insignificant both at 0.34 and 8.92 T. To test this, spectra were generated by linearly mixing the magnetizations simulated using the m and p segments in a 2:1 ratio, equal to their populations in the MD trajectories. The resulting spectra are labeled '67%' in Fig. 3.13, where they are superimposed on the spectra from the full MD trajectories (all). As suspected, the two match perfectly. Evidently, due to the high energetic barrier

of the disulfide torsion, ESR spectra of R1 in the 9-250 GHz frequency range are always a simple linear superposition of at least two components, independently of whether the spectrum appears to be a "simple one-component" or a "complex two-component" spectrum [51]. Since there are no dynamic effects in the mixing of the m and p conformations, it becomes feasible to simulate the two separately and determine their ratio by fitting the calculated spectrum to experiment. This observation is encouraging for using MD trajectories in the simulation of ESR spectra.

3.4 Discussion

3.4.1 Parametrization

The partial charges for the N and O atoms of the nitroxide moiety (Table 3.1) are in good agreement with the charges 0.17 and -0.31, respectively, recommended in Ref. [5]. There, the charges were determined by a restrained fit to the *ab initio* electrostatic potential calculated using HF/6-31G** level of theory—a procedure very similar to the one that we followed. In the parametrization of Ref. [5], the nonpolar hydrogens have a charge of 0.06, which is typical for the AMBER/OPLS force field [66, 67], whereas we imposed the value of 0.09, in agreement with the nonpolarizable CHARMM force field. In Refs. [118] and [19] the charges of Barone *et al.* are used directly without further assessment. More recently Murzyn *et al.* determined the partial charges of the nitroxide ring of R1 by performing a restricted fit to the *ab initio* electrostatic potential using the AMBER/OPLS protocol [96]. They reported partial charges of 0.118 and -0.395 for the N and O atoms of the

nitroxide. Beier and Steinhoff [7] used two different sets of charges: -0.04 and -0.2, as well as 0.08 and -0.3 for the N and O atoms, respectively. In both cases the charges appear to be somewhat low, as acknowledged by the authors [7].

Until now, none of the studies performing MD simulations with R1 have reported a comparison of their dihedral force field parameters with *ab initio* calculations of the torsional energies of the linker. In some cases, when the time traces of the dihedrals are reported, it is possible to have at least a qualitative idea of the multiplicity of the torsions and the approximate positions of their local minima. For example, Figs. 6 and 7 in Ref. [96] indicate that in that study χ_5 has a multiplicity of three, with preferred conformations at $\pm 60^\circ$ and 180°. Evidently, the dihedral energy barriers of the force fields used in this study were not evaluated against *ab initio* energy calculations.

One dimensional *ab initio* energy scans (performed using HF/6-31G** level of theory), in general agreement with our two dimensional energy surfaces (Figs. 3.6 and 3.7), were reported in Ref. [137]. The construct used for the *ab initio* scan of χ_1 in that study was very similar to the one shown in Fig. 3.4, with the exception that the methyl group attached to S2 was replaced by a hydrogen. The model system used to scan χ_5 was exactly the same as the one shown in Fig. 3.5. Two additional fragments were used to scan the remaining torsional profiles: CH_3–CH_2–S–SH for χ_2 and χ_4, and CH_3–S–S–CH_3 for χ_3 [137]. The exact positions of the two minima of χ_5 were observed to depend on the configuration of χ_4. As already discussed, this coupling between χ_4 and χ_5 is poorly captured by conventional force fields. We were able to account for it by using the CMAP correction of CHARMM. The positions of the minima for all angles determined in Ref. [137] (Table 3.7) and the multiplicities of the torsions are in good agreement with our two dimensional

energy surfaces (Figs. 3.6 and 3.7).

3.4.2 Conformational dynamics of R1

The adiabatic energy profiles of Ref. [137], showed that for the dihedrals from χ_1 to χ_4 the energy minima were separated by barriers ranging from about $4k_{\mathrm{B}}T$ to more than $10k_{\mathrm{B}}T$, at room temperature. Based on this observation, it was concluded that the conformational dynamics of R1 can be rationalized in terms of fast librations in a finite number of stable rotamers with occasional exchanges between them. This picture of the spin label dynamics is very appealing from a conceptual point of view. To use it as a practical tool, one has to be able to identify the populations of the important rotamers and to estimate the rates of exchange between them. How to do so in practice was illustrated in Ref. [137] for a spin labeled poly-alanine α-helix: First, R1 was built in all of its 108 possible rotameric states using the reference values for the angles (Table 3.7). Rotamers which led to steric clashes with the helix were eliminated. This resulted in a dramatic decrease of the allowed rotamers from 108 to 18. Second, the populations of the remaining 18 rotamers were estimated based on the energy differences between the minima of the *ab initio* energy profiles. For this, the potential energy was approximated to be a sum of the single bond contributions. For example, the χ_1 torsional potential (with $\chi_2 \approx 180°$), shown in Fig. 3A of Ref. [137], exhibits a global minimum at $-60°$ and two local minima at $+65°$ and $180°$. Since the global minimum is about 2 kcal/mol deeper than the other two minima, rotamers in which $\chi_1 = -60°$ are more than an order of magnitude more probable than the ones in which $\chi_1 = +65°$ or $180°$. The 18 relevant rotamers of Ref. [137] are shown in Table 3.11 together with their estimated probabilities. Finally, the energy barriers separating the minima were

Table 3.11: The 18 rotamers identified as relevant in Ref. [137] together with their populations.

rot.	χ_1	χ_2	χ_3	χ_4	χ_5	prob. (%)
C5(C6)	−60	180	90	180	77(−77)	18.7
C1(C2)	−60	−75	−90	180	77(−77)	14.3
C8	−60	180	90	75	8	9.8
C4	−60	−75	−90	−75	−8	7.4
C7	−60	180	90	75	−100	5.9
C3	−60	−75	−90	−75	100	4.5
C9(C10)	180	180	−90	180	77(−77)	0.9
C13(C14)	180	180	90	180	77(−77)	0.9
C15(C16)	180	75	90	180	77(−77)	0.7
C12	180	180	−90	−75	−8	0.5
C18	180	75	90	75	8	0.4
C11	180	180	−90	−75	100	0.3
C17	180	75	90	75	−100	0.2

used to estimate the rates of exchange between the rotamers. It was assumed that exchanges occur through single dihedral angle flips. Arguments about the hydrodynamic friction experienced by the spin label were invoked to argue that transitions about χ_1, χ_2 and χ_3 are rather slow on the time scale of X-band ESR and can be safely ignored. As a result, only transitions about χ_4 and χ_5 were considered, in agreement with the experimentally established χ_4/χ_5 model of spin label dynamics.

In the last column of Table 3.9, the identity of the most populated 18 rotamers

according to the MD simulations is compared with the rotamers identified as relevant in Ref. [137]. It is seen that the most populated six rotamers from the MD trajectories are among the ones which were eliminated in Ref. [137] due to steric clashes. This observation signals that building ideal rotamers using the reference values for the dihedrals (determined from the minima of the *ab initio* energy profiles) can be misleading. Apparently, the spin label can easily avoid steric clashes by changing some of its dihedrals by a few degrees and still remain in the same rotamer. The fact that among the first twelve rotamers in Table 3.9 only two pass the steric clash test indicates that the flexing of the dihedrals to avoid steric clashes is more than compensated by the resulting hydrophobic contacts between the spin label and the helix. As we saw, exactly such conformations in which the spin label is able to maximize its contact with the helix are the most populated ones.

It has been previously proposed that weak hydrogen bonds between the sulfurs of the disulfide and the backbone hydrogens contribute to immobilize the χ_1 and χ_2 dihedrals on the time scale of a 9 GHz ESR experiment [26, 90, 91]. Previous MD simulations report either the presence [96] or the absence [7] of sulfur hydrogen bonds with the backbone C_α or amide hydrogens. In both cases, however, the force field lacks the correct ingredients to capture the energetics of such interactions (i.e. sulfur polarizability or lone pairs). In our simulation, we observed that the favorable energy gained by placing the sulfurs close to the backbone hydrogens (included effectively through the χ_1–χ_2 CMAP correction) was not sufficient to immobilize the first two linker dihedrals on the ESR time scale.

In contrast to the assumption of independent torsional dynamics, the MD simulations indicate that simultaneous transitions of several of the dihedrals are com-

mon when R1 is on a poly-alanine helix. This observation agrees with studies of the internal dynamics of amino acid side chains. In Ref. [146], for example, the rotameric dynamics of a lysine side chain, which like R1 has five internal torsional degrees of freedom, were studied to evaluate their effect on NMR relaxation times. There, it was observed that the approximation of independent internal rotations becomes less satisfactory for longer side chains, like lysine, necessitating the addition of two-bond and three-bond rotations in the set of elementary moves together with single-bond transitions [146].

In Ref. [96], it was proposed that the two spectral components, immobilized and mobile, often observed in the spectra of R1, might correspond to conformations with different values of χ_3. In that work, two 10 ns MD simulations of R1 attached to a site on Cytochrome c were performed. The spin label was started with $\chi_3 \approx -90^\circ$ in one of the simulations and $\chi_3 \approx 90^\circ$ in the other. It visited 3 rotamers during the former and 13 during the latter. According to the authors, this observed difference in the mobilities of the two states constitutes a "direct evidence for the effect of χ_3 conformation on dynamics of MTSL moiety" [96]. Our simulations are in qualitative agreement with the observations of Ref. [96] as far as the differences in the ordering and dynamics of the m and p conformations of R1 are concerned: on a poly-alanine α-helix the m states of R1 are more ordered and less mobile than the p states. At the same time, our analysis does not point to any intrinsic property of the disulfide torsion χ_3 that will cause these differences. What orders and immobilizes the spin label in our simulations are the nonspecific hydrophobic contacts with the neighboring alanine side chains. Conformations with different values of χ_3 are able to optimize such contacts to a different degree. It simply happens that on the poly-alanine helix, and apparently at the position studied in Ref. [96], the m conformations are able do to so better than the p conformations.

The opposite might very well be the case in other nontrivial contexts on SEHS sites where, in addition to hydrophobic contacts, specific interactions of the nitroxide with polar or charged side chains could also be present.

3.4.3 Simulated ESR spectra

Very good fits to the 9 GHz and 250 GHz experimental spectra of 44R1, 69R1, 72R1, and 131R1 on T4L in water have been reported [4, 81]. In these studies the SRLS model was used to model the dynamics of the spin label attached to the protein simultaneously with the tumbling of the protein. Excellent fits to the 9 GHz spectra of 72R1, 131R1 and more recently 115R1 and 82R1 on T4L in 30 wt % sucrose solution have been performed [27, 44, 51] using the MOMD model. The MOMD model, differently from the SRLS model, does not account for the rotational diffusion of the protein. As already alluded to, our simulated spectra in Fig. 3.12(a) suggest that the tumbling of T4L has a non-negligible effect on the 9 GHz spectra, even in 30 wt % sucrose solution.

The difference in the X-band spectra of 72R1 and 131R1 in T4L, has been rationalized in terms of the difference in the magnitude of the backbone fluctuations at these two SEHS sites [26, 27, 81, 138]. Due to the significant flexibility of the linker observed in the MD simulations, the coupling of the nitroxide to the protein backbone might not be as strong as previously imagined. The fact that the 'm' and 'all' spectra in Fig. 3.13(b), both corresponding to R1 at a poly-alanine helix, qualitatively resemble the 250 GHz spectra of 72R1 and 131R1 [81], respectively, suggests that factors other than the protein backbone flexibility may be responsible for the relative ordering and immobilization of the spin label at those two sites. The difference in the spectra in our case is entirely due to differences in the ability

of R1 in the two ensembles to engage in hydrophobic contacts with the helix.

3.5 Conclusions

We studied the dynamics of R1 on a poly-alanine α-helix, which, in some sense, constitutes the "ideal" noninteracting SEHS site. Before performing atomistic MD simulations of the fully solvated system, force field parameters for the spin label were developed. The electrostatic properties of the spin label—in particular its dipole moment and interaction energies and geometries with water—were carefully compared with *ab initio* calculations. Special attention was given to the energetics of rotation about the bonds separating the nitroxide ring from the C_α of the spin-labeled residue. These two sets of parameters are extremely important since eventually they determine (1) to what extent the spin label is solvated by water or "sticks" to the accessible hydrophobic patches in its vicinity, and (2) what regions are accessible given the energetic penalties associated with flexing the linker of the spin label.

Our MD simulations indicate that the ordering and dynamics of R1 on a poly-alanine helix result from the competition of various forces with relatively weak energies. Contrary to what is commonly believed, the interaction of the disulfide with the backbone does not seem to lead to the immobilization of the first two dihedrals of the spin label linker on the ESR time scale. The ordering appears to be driven by the favorable van der Waals interaction of the surface of the spin label with the hydrophobic surface provided by the alanine side chains. This implies that the nitroxide and the protein backbone are coupled weakly and indirectly, potentially making R1 a poor reporter of the protein backbone fluctuations. The

degree to which the nitroxide moiety can optimize its contacts with the polypeptide environment is determined by the energetics of the dihedral angles of the spin label side chain. Sorting of the preferred R1 conformations based on the steric clashes of a rigidly built spin label is therefore unlikely to retain the most favorable rotamers. A similar concern applies to a Monte Carlo search in which the spin label is constructed using ideal reference angles for its dihedrals.

What are the implications of the present results on the dynamics of R1 at noninteracting SEHS sites in T4L? One of the most important observations appears to be the propensity of the spin label to interact with the neighboring protein surface. Nonpolar interaction energies on the order of $2k_{\mathrm{B}}T$ are present in the environment of the poly-alanine α-helix. The interactions of a solvent-exposed spin label with its immediate neighbors in a protein are expected to be much more varied than the ones observed in our MD simulations. From this perspective, even a spin label attached to an isolated helix does not fit the expected behavior of an ideal noninteracting site. Thus, the distinction between "noninteracting" and "interacting" SEHS sites [51] is a matter of degree, and not of fundamental qualitative difference. When compared with our simulated spectra at 9 GHz, the spectra of 72R1 and 131R1 on T4L indicate that R1 is more ordered and less mobile at these two positions than it is at the poly-alanine helix. Since the ordering does not seem to be due to the adsorption of the disulfide to the protein backbone, it is likely that the polypeptide surface accessible to the spin label from those two sites is more rugged than the relatively structureless surface of the poly-alanine helix.

Many questions, of course, remain unanswered: If R1 at any SEHS is expected to interact with the neighboring amino acid residues, why were such interactions not detected in the 9 GHz spectra of 72R1 and 131R1? If R1 is not necessarily

a good reporter of the backbone fluctuations, what is causing the differences in the X-band spectra of 72R1 and 131R1? These, and similar questions can only be addressed by performing atomistic MD simulations of fully solvated T4L labeled at those two positions. Such simulations are reported in Ch. 5.

CHAPTER 4

USING MARKOV CHAIN MODELS TO SIMULATE ESR SPECTRA FROM MD TRAJECTORIES OF A NITROXIDE SPIN LABEL

4.1 Introduction

Electron spin resonance (ESR) spectra are rich in information that can be related to the structure and function of the spin labeled biomolecule. Nonetheless, inferring the molecular detail from the spectra is difficult due to uncertainty introduced by the internal dynamics of the utilized reporter. A thorough understanding of the conformational freedom and dynamics of the spin label, therefore, will be very helpful.

In the previous chapter we characterized the behavior of one such spin label, commonly known as R1 (or MTSSL), on the surface of a poly-alanine α-helix by performing molecular dynamics (MD) simulations in explicit solvent. This system was chosen as an idealized model of R1 at solvent-exposed helix surface sites in proteins. Due to the relatively small size of the system, we were able to simulate 18 independent trajectories, each extending for 100 ns. In spite of the reasonably long duration of the simulations, each individual trajectory failed to exhaustively sample all the conformations that were accessible to the spin label. As a result, the times that the spin label was observed to spend in its various conformations, do not necessarily reflect the correct state probabilities, but likely depend on the starting conformations of R1. On the other hand, when taken together, the trajectories seemed to explore a significant realm of conformational possibilities. Even the disulfide torsion angle, the energy barrier for which is known

to be about 7 kcal/mol [63], was observed to flip 10 times between its two stable conformations. There is a strong reason to believe that the combined information from all the simulations might provide a rather good estimate of the populations of the various conformations and the rates of exchange between them, calling for collective analysis of the MD trajecrtories.

An important ansatz to proceed with such an analysis is that during its evolution the spin label side chain "forgets" its past over some relatively short time scale. Mathematically, this suggests that the spin label dynamics can be modeled as a stochastic Markov process. The main idea is that independent, relatively short trajectories can be used to estimate conditional (transition) probabilities, even though they do not necessarily reflect the correct equilibrium probabilities. To this end, the detailed dynamics of the MD trajectories have to be mapped to a discrete-state Markov chain model, the state-to-state transition probability matrix (TPM) of which can be determined from the trajectories. The equilibrium probabilities of the various states are then calculated from the TPM, rather than from the fraction of their occurence in the trajectories. The so-constructed Markov model allows for the generation of arbitrarily long stochastic trajectories, which can be used to simulate ESR spectra in the time domain.

How to build a Markov chain model of a biomolecule from its MD trajectories is unambiguous [24,36,100,127–129,135,136]. First, a set of observables, called order parameters, need to be chosen among the large collection of variables contained in the trajectories. Second, discrete states need to be defined in terms of the values of the order parameters. Once this has been done, the detailed MD trajectories can be replaced by hoping transitions between the discrete states. Lastly, the TPM, describing the kinetics of moving between the states, needs to be estimated from the

time series. The selection of order parameters is a hard problem, lacking a general solution. Although significant progress has been made in specific cases [86], a systematic and universally applicable procedure is not yet available. In most cases, the order parameters to be monitored are chosen based on intuition and physical insight about the system. Common choices for studying the folding of polypeptides, for example, include the number of native contacts the root mean square distance of all the backbone atoms [24], or only the C_αs [128], the hydrogen bond distances [128] or patterns [97], the backbone torsion rotamer [97]. In this chapter, we assume that a choice based on physical intuition is adequate, and consider the remaining two issues: the definition of states given the order parameters and the estimation of the TPM.

The outline of the chapter is as follows: In Sec. 4.2, after reviewing the necessary theory of Markov chain models, we present a two-step procedure for building hidden Markov models from MD trajectories. A theoretical framework that allows us to simulate ESR spectra from the trajectories of the constructed Markov model is developed. In Sec. 4.3, Markov models with different numbers of states are built from the MD trajectories of R1 on the poly-alanine α-helix. The resulting models are used to elucidate the various time scales associated with the internal spin label dynamics and to study the conformational changes that they correspond to. ESR spectra at three different frequencies are simulated from the trajectories generated by these models. The discussion of the results and our conclusions are presented in Sec. 4.4. Additional technical details are contained in Sec. 4.5.

4.2 Theory and methods

4.2.1 Building Markov chain models from trajectories

Commonly, when Markov jump models are constructed from MD trajectories of a biomolecule, the following two steps are performed sequentially. First, the d-dimensional space of the order parameters is divided into numerous, small cells (microstates). The division can be into either equally sized bins [31, 97, 123], or any other irregular basis cells [24, 72, 136]. The latter can either be chosen by hand [136], or determined using some automated strategy, such as the K-means (or K-medoid) clustering algorithm [24]. At this point, it is hoped that if the microstates are chosen to be small enough, such that intra-state relaxation is fast, the kinetics of jumping out of a microstate will be approximately Markovian. Once a meaningful microstate TPM is estimated by counting the transitions (see below), it is used to lump the microstates into several groups of kinetic significance. The resulting macrostates are intended to correspond to the rarely exchanging, metastable conformations of the biomolecule. The lumping step, therefore, necessitates the identification of the weakly coupled sub-blocks of the microstate TPM, and can be achieved in several different ways varying in computational demand [32, 48, 140]. At the end, it is the Markovian kinetics of the macrostates that constitutes a model of the slow dynamics of the biological system.

Consider an N-state, continuous-time Markov chain. Let $i \in \{1, 2, \ldots, N\}$ enumerate the states and $X(t)$ be a random variable indicating the state at time t. The probabilities

$$p_i(t) = \mathbb{P}\{X(t) = i\}, \tag{4.1}$$

to observe the chain in state i at time t, form the vector $p(t) = [p_i(t)]$, whose

evolution is governed by the Master equation

$$\dot{p}_j(t) = \sum_{i=1}^{N} p_i(t) Q_{ij}. \tag{4.2}$$

The matrix $Q = [Q_{ij}]$, referred to as the rate matrix, is the generator of the chain. Its off-diagonal entries are larger or equal to zero. Its diagonal elements are negative and given as [98]

$$Q_{ii} = -\sum_{j \neq i} Q_{ij}. \tag{4.3}$$

They are directly related to the lifetime σ_i of each state:

$$\sigma_i = -1/Q_{ii}. \tag{4.4}$$

For two states i and j ($j \neq i$), the combination $\sigma_i Q_{ij}$ gives the probability that the chain jumps to state j given that it leaves state i [98]. This probabilistic interpretation suggests an intuitive scheme for estimating the rate matrix from a continuously observed trajectory as [11]

$$Q_{ij} = J_{ij}/R_i, \qquad j \neq i, \tag{4.5}$$

where J_{ij} is the number of jumps from state i to state $j(\neq i)$ and R_i is the time spent in state i during the whole trajectory. The diagonal elements follow from Eq. (4.3).

The vector $e = [e_i = 1]$, all the components of which are equal, is the right eigenvector of Q with eigenvalue zero. The corresponding left eigenvector π is the stationary probability distribution of the chain, cf. Eq. (4.2). For a Markov chain built from the MD trajectories of a system in thermal equilibrium, π and Q are expected to be in detailed balance, satisfying

$$\pi_i Q_{ij} = \pi_j Q_{ji}. \tag{4.6}$$

The condition of detailed balance implies that Q can be transformed to a symmetric form by a similarity transformation with the matrix $D = [\sqrt{\pi_i}\delta_{ij}]$, thus, all the eigenvalues of Q are real. When written as $-1/\tau_i$, the non-zero eigenvalues give the relaxation time scales, τ_i, of the stochastic dynamics generated by Q. Note that $\tau_i \neq \sigma_i$.

Coarse-graining the MD trajectories

If the observed time series were generated from a continuous-time Markov chain, one could easily count the total number of $i \to j$ jumps to find J_{ij}, and add the time intervals in which the chain was in state i to calculate R_i. Unfortunately, this is not possible when the trajectories are coming from MD simulations. The major problem is that the short-time dynamics of the order parameters are not necessarily Markovian. In fact they can be inertial over a time interval of 1 ps, typical for saving the MD snapshots. As a result, the traces of the order parameters are typically noisy: spurious transitions back and forth between states i and j are present before a "real" transition occurs. These problems prevent the meaningful estimation of both the number of $i \to j$ jumps and the time spent in state i, making it impossible to deduce the generator of the continuous-time chain using Eq. (4.5). The solution is to allow for the equilibration of molecular and solvent degrees of freedom that are not monitored by the order parameters. If the system was observed at time intervals long enough for such degrees of freedom to equilibrate, its dynamics were more likely to appear memoryless. Thus, it becomes necessary to coarse-grain its evolution in time [22, 23].

The coarse-graining in time comes at a price: Allowing for times τ between two successive observations, we lose touch with the continuous-time Markov process.

Due to this requirement of well-spaced observations, what becomes accessible is a family of discrete-time Markov chain processes, with TPMs parametrized by the observation lag time τ:

$$P(\tau) = \exp(\tau Q). \tag{4.7}$$

We will denote the integer time steps of these chains with a subscript t ($1 \leq t \leq T$), and write the random variable corresponding to the state of the chain at time step t as X_t. The ijth entry of $P(\tau)$ is the conditional probability of the chain to be in state j at time step $t+1$ given that it was in state i at time step t:

$$P_{ij}(\tau) = \mathbb{P}\{X_{t+1} = j | X_t = i\}. \tag{4.8}$$

This automatically implies that, for a given τ, $P(\tau)$ can be estimated from the trajectory as

$$P_{ij}(\tau) = \frac{N_{ij}^{\tau}}{\sum_j N_{ij}^{\tau}}, \tag{4.9}$$

where N_{ij}^{τ} is the number of times $X_t = i$ and $X_{t+1} = j$ (including $j = i$) along the whole trajectory sampled at intervals τ. Since the family of matrices $P(\tau)$ are generated by the same matrix Q, they all share the probability vector π as their left eigenvector with eigenvalue $\lambda_0 = 1$. The condition of detailed balance is also inherited from Q:

$$\pi_i P_{ij}(\tau) = \pi_j P_{ji}(\tau). \tag{4.10}$$

The remaining eigenvalues $\lambda_i(\tau)$ of $P(\tau)$ are restricted, by the relation of $P(\tau)$ to $Q(\tau)$, to lie between zero and one. Each of them is associated with a relaxation time scale τ_i through

$$\tau_i(\tau) = -\tau / \ln(\lambda_i(\tau)), \qquad i \geq 1, \tag{4.11}$$

as can be inferred from Eq. (4.7). The lifetimes σ_i, introduced in terms of the rate matrix in (Eq. (4.4)), can be expressed in terms of the diagonal entries of $P(\tau)$ as

$$\sigma_i(\tau) = \sum_{n=1}^{\infty} (n\tau) P_{ii}^{n-1}(1 - P_{ii}) = \tau/(1 - P_{ii}(\tau)), \tag{4.12}$$

where the sum is over the number of steps n of duration τ spent in state i, and represents the expected value of the time spent in this state.

After the time series of the discrete states are used to estimate $P(\tau)$s for several different values of τ, it is desirable to test whether they are consistent with each other, i.e. whether the TPMs satisfy the semi-group (Chapman-Kolmogorov) property $P(\tau)P(\nu) = P(\tau + \nu)$. A popular version of this test is to examine the time scales $\tau_i(\tau)$, implied by the eigenvalues $\lambda_i(\tau)$ (Eq. (4.11)), as a function of τ, and check whether they are independent of the lag time [24, 36, 135, 136]. The model passes the test if the τ_i's do not vary with τ. If the τ_i's fluctuate for short lag times but then level out for lag times longer than a certain τ^*, the test basically detects the minimum lag time needed for the dynamics to become Markovian.

From the discussion so far, it might appear that having access to the family of TPMs $P(\tau)$ instead of Q does not result in any loss of generality, since one can easily go back and forth between the two using Eq. (4.7). Indeed, when the difference in τ is accounted for, as in Eqs. (4.11) and (4.12), all the matrices $P(\tau)$ correspond to the same time scales τ_i or σ_i. In almost every practical situation though, obtaining the generator Q by inverting Eq. (4.7) is impossible. More often than not, the TPMs estimated from the data using Eq. (4.9) have negative or/and complex eigenvalues. Thus, taking their logarithm to determine the eigenvalues of Q produces non-real numbers. Even when the eigenvalues $\lambda_i(\tau)$ are all positive, the matrix calculated to be Q by inverting Eq. (4.7) very often ends up having negative off-diagonal entries. Different remedies, ranging from neglecting the complex part of the eigenvalues to setting the negative off-diagonal entries to zero [62], are found in the literature. The presence of complex eigenvalues $\lambda_i(\tau)$ is a sign that $P(\tau)$, estimated from the trajectories, is not in detailed balance with its left eigenvector

π. A somewhat more systematic way of making sure that all the eigenvalues are real (but not necessarily non-negative) is to impose detailed balance [36]. Two ways of achieving this are discussed in Sec. 4.5.1.

Lumping microstates into macrostates

Suppose that d order parameters have been chosen successfully and that N discrete states have been defined as non-overlapping regions in the resulting d-dimensional space. For the projection of the MD trajectories onto these states to yield Markovian dynamics when viewed at times spaced by τ, the relaxation times due to the internal structure of the states should be shorter than τ. This forces the states to have as small spatial extent as possible. On the other hand, when the states are excessively small they tend to be visited rarely, making the estimates of the transition probabilities rather poor. As already mentioned before, a common way to deal with these two opposing limitations is to introduce many (e.g. hundreds of) microstates during the initial discretization of the MD trajectories, and then lump them together into a smaller number of kinetically significant macrostates [24,32,123,125]. How to perform a lumping, which captures the slow dynamics of the system without having all the fast detail, is an open question [24,72], in spite of the considerable effort in this direction [30–32, 48, 123, 145].

To introduce the notation and ideas that we rely on later, let us formally examine the lumping step. Diagramatically, the Markovian propagation of the microstates and their lumping into macrostates, can be represented as follows:

$$\begin{array}{ccccccc} p(0) & \xrightarrow{P(\tau)} & p(\tau) & \xrightarrow{P(\tau)} & p(2\tau) & \xrightarrow{P(\tau)} & \\ \downarrow H & & \downarrow H & & \downarrow H & & \\ \tilde{p}(0) & & \tilde{p}(\tau) & & \tilde{p}(2\tau) & & \end{array} \tag{4.13}$$

Here, the horizontal arrows depict the propagation

$$p(t+\tau) = p(t)P(\tau) \tag{4.14}$$

of the microstate probability vector $p(t)$. The vertical arrows indicate that the macrostate probabilities $\tilde{p}(t)$ are related to the microstate probabilities as

$$\tilde{p}(t) = p(t)H, \tag{4.15}$$

where the matrix $H = [h_{ia}]$ is the operator of projection (lumping). A general projection can allow for a given microstate to belong to several different macrostates. The only requirement is that the membership of any microstate to all the M macrostates should sum to one:

$$\sum_{a=1}^{M} h_{ia} = 1, \qquad \text{for all } i. \tag{4.16}$$

Given the microstate equilibrium distribution π, and the projector H, the macrostate equilibrium probabilites $\tilde{\pi}$ follow from Eq. (4.15). In component form

$$\tilde{\pi}_a = \sum_{i=1}^{N} \pi_i h_{ia}. \tag{4.17}$$

It is useful to introduce the probability contribution of microstate i to macrostate a as

$$w_{ai} = \frac{\pi_i h_{ia}}{\tilde{\pi}_a}, \tag{4.18}$$

for which the normalization condition

$$\sum_{i=1}^{N} w_{ai} = 1, \qquad \text{for all } a, \tag{4.19}$$

holds by construction. For a given a, w_{ai} is the intra-macrostate equilibrium distribution of the microstates. From Eqs. (4.18) and (4.16) one finds

$$\pi_i = \sum_{a=1}^{M} \tilde{\pi}_a w_{ai}. \tag{4.20}$$

This relation is the dual of Eq. (4.17), since it expresses π in terms of $\tilde{\pi}$ and W. The duality can be depicted as follows:

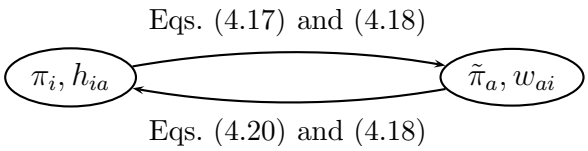

Starting from the quantities in one of the ellipses the quantities in the other ellipse are obtained using the specified equations. In [73] and [72], following the top arrow to go from π to $\tilde{\pi}$ was called *restriction*, whereas going in the opposite direction was called *interpolation*. According to this nomenclature, H and W are the operators of restriction and interpolation. The former "restricts" any probability density over the microstates to a probability density over the macrostates (Eq. 4.15), whereas the latter "interpolates" a detailed probability density from a coarse-grained one as

$$p(t) = \tilde{p}(t)W. \tag{4.21}$$

This naive way of building detail is based on the assumption that the internal probability structure of a macrostate is always in equilibrium. Note that in general, restriction (Eq. (4.15)) followed by interpolation (Eq. (4.21)) does not recover the starting mictostate probability vector,

$$p(t) \neq p(t)A, \tag{4.22}$$

where $A \equiv HW$ is a stochastic matrix (i.e. rows sum to one). Only the microstate equilibrium probability is invariant under this operation, $\pi = \pi A$. Since the action of A on an arbitrary vector leads to another probability vector which is automatically equilibrated inside each of the macrostates, A can be viewed as an operator of intra-macrostate equilibration.

In effect, during the lumping of the microstates into macrostates, a membership array H is sought, such that the macrostate TPM

$$\tilde{P}(\tau) = WP(\tau)H \tag{4.23}$$

captures the slow dynamics of the Markovian microstate propagation as best as possible. (Equation (4.23) reduces to the more familiar

$$\tilde{P}_{ab}(\tau) = \frac{\sum_{i\in a}\sum_{j\in b}\pi_i P_{ij}(\tau)}{\sum_{i\in a}\pi_i}, \tag{4.24}$$

when the elements of H are restricted to be only zero or one, i.e. macrostates are defined with "sharp" boundaries.) The lower dimensional matrices $\tilde{P}(\tau)$ are then used to propagate directly the macrostate probabilities in a Markovian fashion. Various algorithms for constructing sharp [24, 140] or "fuzzy" [32, 48] H from a given P have been proposed.

As clearly demonstrated in [73] and [72], in general, the matrices $\tilde{P}(\tau)$ fail to generate Markovian dynamics in the space of the macrostates, because of the non-commuting nature of propagation and restriction (lumping). More specifically, a two-step microstate propagation followed by lumping does not lead to the same probability density as a lumping followed by a two-step macrostate propagation. This is easily seen using matrix notation:

$$\tilde{P}(\tau)\tilde{P}(\tau) = WP(\tau)AP(\tau)H \neq WP(\tau)P(\tau)H = \tilde{P}(2\tau). \tag{4.25}$$

In words, the square of $\tilde{P}(\tau)$, estimated using a given lag time, is systematically different from $\tilde{P}(2\tau)$, estimated with twice as long lag time. Taking the square of $\tilde{P}(\tau)$ is seen to impose instantaneous equilibration of the microstates inside a macrostate in between two time steps (the matrix A in Eq. (4.25)). Replacing the detailed microstate dynamics with coarse-grained macrostate propagation relies on the assumption that after an inter-macrostate transition the chain will dwell inside the macrostate long enough to sample its equilibrium distribution before making a transition to another macrostate. This is achieved to a large degree by grouping microstates that exchange fast into macrostates, which, on the other hand, are

chosen to be as weakly coupled as possible. In spite of that, occasionally, short-lived visits into macrostates are possible. Their presence leads to an artificially faster macrostate dynamics and is the physical reason behind the inequality in Eq. (4.25). To distinguish such brief visits from "real" transitions, we choose to analyze the time series of the order parameters and to model the spin label dynamics as a *hidden* Markov model (HMM).

4.2.2 Context dependent treatment using hidden Markov models

HHMs have found widespread application in areas as diverse as speach recognition [112], analysis of currents from single ion channels [111, 143], or other single molecule data [92]. In this section, we utilize the well-established methodology of HMMs [112] as a framework that is able to identify state boundaries and inter-state transitions probabilistically, by consdering the complete sequence of events.

Coarse-graining with fuzzy boundaries

In a HMM, the states of the Markov chain are not directly observed. What is observed is the d-dimensional (random) vector of order parameters $\boldsymbol{O}_t$ which is modeled to be "emitted" when the chain is in state i according to some probability density. For analytical tractability, it is convenient to choose the probability density to observe $\boldsymbol{O}_t = \boldsymbol{y}$ when $X_t = i$ as a multivariate Gaussian with a mean

vector $\boldsymbol{\mu}_i$ and a covariance matrix Σ_i:

$$\begin{aligned} b_i(\boldsymbol{y}) &= \mathbb{P}\{\boldsymbol{O}_t = \boldsymbol{y} | X_t = i\} \\ &\propto \sqrt{\frac{\det\{\Sigma_i^{-1}\}}{(2\pi)^d}} \mathrm{e}^{-\frac{1}{2}(\boldsymbol{y}-\boldsymbol{\mu}_i)^\top \cdot \Sigma_i^{-1} \cdot (\boldsymbol{y}-\boldsymbol{\mu}_i)}. \end{aligned} \tag{4.26}$$

In this expression, $\boldsymbol{v}^\top$ indicates the transpose of $\boldsymbol{v}$. Given the sequence of observations,

$$O = \boldsymbol{O}_1 \boldsymbol{O}_2 \ldots \boldsymbol{O}_T, \tag{4.27}$$

and the parameters of the HMM, $\theta = \{p, P(\tau), \boldsymbol{\mu}_i, \Sigma_i\}$, it is possible [112] to calculate the conditional probability

$$\xi_{ij}(t) = \mathbb{P}\{X_t = i, X_{t+1} = j | O, \theta\} \tag{4.28}$$

for the chain to be in state i at time step t and state j at time step $t+1$. The way this is done iteratively is presented in Sec. 4.5.2. (The ith entry of the probability vector p that appeared in θ corresponds to the probability of the chain to start in state i.) With the help of $\xi_{ij}(t)$ it is straightforward to calculate the expectation

$$\mathbb{E}\{N_{ij}^\tau | O, \theta\} = \sum_{t=1}^{T-1} \xi_{ij}(t), \tag{4.29}$$

which can be used in Eq. (4.9), instead of N_{ij}^τ, to estimate $P(\tau)$. To update the other parameters of the HMM it is convenient to consider the probability to be in state i at time t, given O and θ [112],

$$\gamma_i(t) = \mathbb{P}\{X_t = i | O, \theta\} = \sum_{j=1}^{N} \xi_{ij}(t). \tag{4.30}$$

With it, the parameters are updated as follows [112]:

$$p_i = \gamma_i(1), \qquad P_{ij}(\tau) = \frac{\sum_{t=1}^{T-1} \xi_{ij}(t)}{\sum_{t=1}^{T-1} \gamma_i(t)} \tag{4.31}$$

and

$$\boldsymbol{\mu}_i^{\text{new}} = \boldsymbol{\mu}_i^{\text{old}} + \bar{\boldsymbol{\mu}}_i, \qquad \Sigma_i^{\text{new}} = \bar{\Sigma}_i - \bar{\boldsymbol{\mu}}_i \bar{\boldsymbol{\mu}}_i^\top, \tag{4.32a}$$

where

$$\bar{\boldsymbol{\mu}}_i \equiv \frac{\sum_{t=1}^{T} \gamma_i(t)(\boldsymbol{O}_t - \boldsymbol{\mu}_i^{\text{old}})}{\sum_{t=1}^{T} \gamma_i(t)} \tag{4.32b}$$

$$\bar{\boldsymbol{\Sigma}}_i \equiv \frac{\sum_{t=1}^{T} \gamma_i(t)(\boldsymbol{O}_t - \boldsymbol{\mu}_i^{\text{old}})(\boldsymbol{O}_t - \boldsymbol{\mu}_i^{\text{old}})^{\top}}{\sum_{t=1}^{T} \gamma_i(t)}. \tag{4.32c}$$

These equations can be derived using maximum likelihood arguments [10, 83]. When the order parameters are angles, periodic boundary conditions can be imposed on the difference $\boldsymbol{O}_t - \boldsymbol{\mu}_i$.

The hidden Markov modeling strategy presented here shares similarities with the K-means clustering: in both of the methods the number of desired states (clusters) is provided as an input; for each cluster, a representative point ("centroid" in K-means, $\boldsymbol{\mu}_i$ in the HMM) is determined and its members are assigned in an iterative way; the assignment of membership relies on the choice of a distance metric in the space of order parameters. Nevertheless, crucial differences separate the two methods. Whereas the clusters formed by the K-means clustering are purely geometric, the geometry and the kinetics are fused together in the identification of the states in the HMM. After a partitioning of the order parameter space into microstates, which is uninformed by the temporal ordering of the data points, one can only hope that the resulting dynamics will turn out to be Markovian. The partitioning with a HMM, on the other hand, is performed having in mind the expected Markovian dynamics, and considers the entire data as a time-ordered sequence. Needless to say, all those advantages come at the expense of increased computational effort, which, considering the resources demanded by the generation of the starting MD trajectories, is well justified.

Probabilistic lumping

The context dependent analysis can be easily extended to the lumping step, in which the aim is to build a discrete-time Markov chain model with a reduced number of states. The spatial resolution offered by the microstates is preserved by retaining the number of Gaussian basis functions, and using the same microstate emission probability densities as before (Eq. (4.26)). We look for M macrostates with Markovian dynamics according to some probability matrix $\tilde{P}(\tau)$. No dynamics are associated with the microstates. The emission probability b_a from each macrostate a, is a mixture of the N microstate components b_i:

$$b_a(\boldsymbol{y}) = \sum_{i=1}^{N} w_{ai} b_i(\boldsymbol{y}), \qquad 1 \leq a \leq M, \tag{4.33}$$

where w_{ai} is the probability contribution of i to a (Eq. (4.18)). Thus, we deal with a HMM in which the emission from each (hidden) macrostate is a mixture of Gaussian components. The iterative calculation of $\gamma_a(t)$ (Eq. (4.30)) and the update of the starting probabilities and the transition matrix (Eq. (4.31)) remain unchanged, with the understanding that now the indices stand for macrostates. For the estimation of the microstate properties it is useful to introduce [112]

$$\gamma_{ai}(t) = \gamma_a(t) \frac{w_{ai} b_i(\boldsymbol{O}_t)}{b_a(\boldsymbol{O}_t)} \quad \text{and} \quad \gamma_i(t) = \sum_{a=1}^{M} \gamma_{ai}(t). \tag{4.34}$$

The former is the probability of being in macrostate a at time step t having generated $\boldsymbol{O}_t$ from microstate i. The latter is the probability of emitting $\boldsymbol{O}_t$ at time t from a microstate i, idependently of what the macrostate is. The contributions of the microstates to the macrostates are updated as

$$w_{ai} = \frac{\sum_{t=1}^{T} \gamma_{ai}(t)}{\sum_{t=1}^{T} \gamma_a(t)}, \tag{4.35}$$

whereas $\boldsymbol{\mu}_i$ and Σ_i are calculated from Eqs. (4.32).

4.2.3 ESR spectra and the Markov chain model

Stochastic Liouville equation background

The stochastic Liouville equation (SLE), due to Kubo [74–76], describes the dynamics of a quantal system coupled to a classical bath, where the dynamics of the bath are modeled by a stochastic process. A basic assumption of the equation is that the classical degrees of freedom are not influenced by the quatum dynamics. This approximation is rather good for phenomena involving magnetic resonance of electronic and nuclear spins [1, 37].

Let us consider a quantal system with a density operator $|\rho(t)\rangle\rangle$, written as a Liouville space vector [95], coupled to a Markov chain process $X(t)$. The probabilities $p_i(t)$ for the process (Eq. (4.1)) satisfy the Master equation (4.2). The density operator obeys the Liouville-von Neumann equation

$$|\dot{\rho}(t)\rangle\rangle = -\mathrm{i}\check{L}_{X(t)}|\rho(t)\rangle\rangle, \tag{4.36}$$

in which the dependence of the Liouvillian on the state of the Markov chain is denoted as a subscript. (The inverted caret indicates that the Liouvillian is a Liouville space operator, i.e. a superoperator.) The SLE for this coupled quantum-classical system is an equation of motion for [75, 76]

$$|u_i(t)\rangle\rangle = \mathbb{E}\big\{|\rho(t)\rangle\rangle | X(t) = i\big\}, \tag{4.37}$$

the expectation of the density matrix at time t given that currently $X(t) = i$. It reads [75, 76]

$$|\dot{u}_j(t)\rangle\rangle = -\mathrm{i}\check{L}_j|u_j(t)\rangle\rangle + \sum_i Q_{ij}|u_i(t)\rangle\rangle. \tag{4.38}$$

When $X(0)$ is chosen from the equilibrium probability density π, the initial con-

dition of Eq. (4.38) is

$$|u_i(0)\rangle\rangle = |\rho(0)\rangle\rangle\pi_i. \tag{4.39}$$

Notice that initially $|u_i(t)\rangle\rangle$ is separable in its classical and quantum parts. For a bath which is modeled by a continuous stochastic process $Y(t)$, the probability density $p(y,t)$ is taken to satisfy a Fokker-Planck equation [52]

$$\partial_t p(y,t) = \mathscr{G} p(y,t), \tag{4.40}$$

with stationary solution $\pi(y)$. The differential operator $\mathscr{G}$ acts on the variable y. In such cases, the SLE becomes [75, 76, 122]

$$\partial_t |u(y,t)\rangle\rangle = -\mathrm{i}\check{L}(y)|u(y,t)\rangle\rangle + \mathscr{G}|u(y,t)\rangle\rangle \tag{4.41}$$

with initial condition

$$|u(y,0)\rangle\rangle = |\rho(0)\rangle\rangle\pi(y). \tag{4.42}$$

Eliminating the fast intrastate dynamics

When different components of the classical dynamics evolve on well separated time scales one can formally eliminate the fast dynamics. For example, the dynamics of a given spin label can be viewed as a superposition of fast intrastate dynamics Y in a given macrostate X, and much slower exchanges between the macrostates. Symbolically, this can be written as [34, 49, 142]

$$\dot{Y}(t) = \frac{1}{\epsilon} g(X(t), Y(t)), \qquad \dot{X}(t) = f(X(t)), \tag{4.43}$$

where ϵ is a small parameter and the functions f and g are $O(1)$ in ϵ. Clearly, for small ϵ, Y varies on a faster time scale than X. In Eq. (4.43) it is assumed that the exchanges do not depend on the intrastate dynamics, thus f is independent of

Y. Associated with this system of evolution equations is a Fokker-Planck-Master equation

$$\partial_t p_j(y,t) = \frac{1}{\epsilon}\mathscr{G}_j p_j(y,t) + \sum_i p_i(y,t) Q_{ij} \tag{4.44}$$

for the joint probability density $p_i(y,t)$. The operator $\mathscr{G}_j$ acts only on the variable y but depends on the state j of the Markov chain. There is a different operator (with different diffusion tensor and ordering potential, for example) for each j. Its exact form is not important for the purposes of our discussion. Suffice it to say that $\pi(y|j)$ that satisfies the condition

$$\mathscr{G}_j \pi(y|j) = 0 \tag{4.45}$$

is the equilibrium probability density of Y for a given state j.

Coupling the classical processes in Eq. (4.43) to the quantal dynamics (cf. Eq. (4.36))

$$|\dot{\rho}(t)\rangle\!\rangle = -\mathrm{i}\check{L}_{X(t)}(Y(t))|\rho(t)\rangle\!\rangle, \tag{4.46}$$

one obtains the SLE

$$\begin{aligned}\partial_t |u_j(y,t)\rangle\!\rangle = \Big(-\mathrm{i}\check{L}_j(y) + \frac{1}{\epsilon}\mathscr{G}_j\Big)|u_j(y,t)\rangle\!\rangle \\ + \sum_i Q_{ij}|u_i(y,t)\rangle\!\rangle\end{aligned} \tag{4.47}$$

with initial condition

$$|u_i(y,0)\rangle\!\rangle = |\rho(0)\rangle\!\rangle \pi_i(y). \tag{4.48}$$

Here $\pi_i(y)$ is the joint equilibrium probability density corresponding to Eq. (4.44). We look for a solution of the SLE in the form [49]

$$|u\rangle\!\rangle = |u^{(0)}\rangle\!\rangle + \epsilon|u^{(1)}\rangle\!\rangle + \epsilon^2|u^{(2)}\rangle\!\rangle + \cdots, \tag{4.49}$$

with initial conditions

$$\begin{aligned}|u_i^{(0)}(y,0)\rangle\!\rangle &= |u_i(y,0)\rangle\!\rangle \\ |u_i^{(k)}(y,0)\rangle\!\rangle &= 0, \qquad k \geq 1.\end{aligned} \tag{4.50}$$

Substituting in Eq. (4.47) and collecting terms with equal power of ϵ leads to the hierarchy of equations

$$\epsilon^{-1}: \quad \mathscr{G}_j|u_j^{(0)}(y,t)\rangle\!\rangle = 0, \tag{4.51a}$$

$$\epsilon^{0}: \quad \mathscr{G}_j|u_j^{(1)}(y,t)\rangle\!\rangle = \big(\partial_t + \mathrm{i}\check{L}_j(y)\big)|u_j^{(0)}(y,t)\rangle\!\rangle - \sum_i Q_{ij}|u_i^{(0)}(y,t)\rangle\!\rangle, \quad \cdots. \tag{4.51b}$$

The first equation implies that $|u_j^{(0)}(y,t)\rangle\!\rangle$ is in the null space of $\mathscr{G}_j$. From Eq. (4.45) it follows that

$$|u_j^{(0)}(y,t)\rangle\!\rangle = \pi(y|j)|h_j(t)\rangle\!\rangle, \tag{4.52}$$

where $h_j(t)$ is arbitrary. Let us define the operator [49, 68, 69]

$$\mathscr{P}a_j(y) \equiv \pi(y|j)\int a_j(y)\,\mathrm{d}y, \tag{4.53}$$

which projects onto the null space of $\mathscr{G}_j$ by mapping a general function of (j,y) into a function of j times $\pi(y|j)$. With this, the requirement that $u^{(0)}$ is in the null space of $\mathscr{G}_j$ translates into $\mathscr{P}u^{(0)} = u^{(0)}$. It is not hard to see that $\mathscr{P}\mathscr{G}_j = \mathscr{G}_j\mathscr{P} = 0$. Acting with $\mathscr{P}$ on both sides of the second equation in the hierarchy gives

$$\partial_t|u_j^{(0)}(y,t)\rangle\!\rangle = -\mathrm{i}\mathscr{P}\check{L}_j(y)|u_j^{(0)}(y,t)\rangle\!\rangle + \sum_i Q_{ij}|u_i^{(0)}(y,t)\rangle\!\rangle. \tag{4.54}$$

Using Eqs. (4.52) and (4.53), the first term on the right hand side of the equality becomes

$$\mathscr{P}\check{L}_j(y)|u_j^{(0)}(y,t)\rangle\!\rangle = \bar{\check{L}}_j|u_j^{(0)}(y,t)\rangle\!\rangle, \tag{4.55}$$

where

$$\bar{\check{L}}_j \equiv \int \check{L}_j(y)\pi(y|j)\,\mathrm{d}y \tag{4.56}$$

is the Liouvillian for state j averaged over the equilibrium probability of the fast dynamics inside the state. The physical implication is that the process Y relaxes

to its equilibrium distribution before X has time to change. As a result, Eq. (4.54) together with its initial condition can be viewed as the SLE corresponding to the system of equations

$$\dot{X}(t) = f(X(t)), \qquad |\dot{\rho}(t)\rangle\rangle = -\mathrm{i}\bar{\bar{L}}_{X(t)}|\rho(t)\rangle\rangle. \tag{4.57}$$

Thus, to lowest order, one can replace the instantaneous Liouvillian with its average over the current macrostate. Below, we use this result in the simulation of ESR spectra from the Markov models estimated from the MD trajectories.

4.3 Results: Dynamics and ESR spectra of R1 on a poly-alanine helix

4.3.1 Building the Markov chain models

The analysis of the conformational dynamics of R1 on a poly-alanine α-helix, presented in Ch. 3, suggests that the five dihedrals of the spin label are good candidates for order parameters to be used to monitor its dynamics. An alternative set of order parameters are the Euler angles $\Omega_{\mathtt{MN}}$ that parametrize the transformation of the helix-fixed coordinate system `M` to the nitroxide-fixed system of axes `N`. To compare these two choices, we attempted the construction of two Markov chain models: one, using the spin label dihedral angles, and the other, using the Euler angles. The MD snapshots from each of the 18 trajectories were first projected to the space of the order parameters. The resulting points in five or three dimensions were then clustered using the K-means algorithm. The latter is based on the definition of distance in the multidimensional space of the order parameters. We

chose an Euclidian distance metric in the five dimensional space of the dihedral angles. The only complication, related to the periodicity of the angles, was treated by restricting the separation between two points in each of the dimensions to be always in the range $(-180°, 180°)$. Since selecting a distance metric in the space of the Euler angles is not trivial, we chose to work with quaternions of unit length. Such quaternions live on the surface of a four-dimensional unit sphere for which the great circle arc between two points defines a natural distance metric [77, 126]. Considering the multiplicity of its five linker dihedral angles ($\chi_1 : 3$, $\chi_2 : 3$, $\chi_3 : 2$, $\chi_4 : 3$, and $\chi_5 : 2$) the spin label R1 potentially has 108 rotamers. To ensure the complete coverage of all the rotamers, the K-means clustering algorithm was initiated with 120 clusters. For the model using the dihedral angles as order parameters, 108 centroids were initialized at the ideal, "reference" dihedral angles of each rotamer ($\pm 60°$, $180°$ for multiplicity of 3, $\pm 90°$ for multiplicity 2). The remaining 12 centroids were chosen randomly by generating random numbers from a uniform distribution in the angular range $(-180°, 180°)$. For the other model, the initial 120 centroids were chosen to be uniformly-distributed random unit quaternions [77]. When the dihedral angles were used to build the centroids, some of the initial centroids failed to have any snapshots assigned to them. Such centroids were moved around randomly before the next iteration. This was repeated until all the 120 centroids acquired members. For the two choices of order parameters, convergence was assumed when the average centroid shift in one iteration was less than 10^{-5} degrees in the space of the five dihedral angles, and less than 10^{-4} on the surface of the four-dimensional unit sphere.

As a result of the clustering, the trajectories of the order parameters were converted to time series of jumps between 120 discrete states. These were then used to construct TPMs for values of τ ranging from 50 to 800 ps. The time

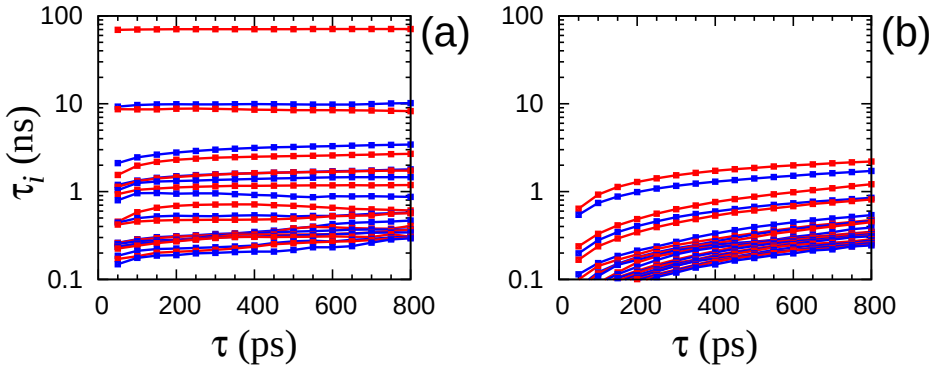

Figure 4.1: Time scales τ_i $(1 \leq i \leq 22)$ of the two K-means-based Markov models as a function of lag time τ: (a) dihedral angles and (b) quaternions (Euler angles) used as order parameters.

scales τ_i, implied by the non-negative eigenvalues of $P(\tau)$, were calculated from Eq. (4.11). The slowest 22 time scales are shown in Fig. 4.1 as a function of τ for the two models. The independence of the relaxation times on the lag time is a signature of a good Markovian model. Whereas the lines are more or less horizontal in Fig. 4.1(a), they are significantly sloped in Fig. 4.1(b). More importantly, according to the first model, the slowest dynamical event occurs on a time scale of ∼70 ns, followed by two other events on time scales ∼10 ns; these time scales are completely missing in the second model.

From the analysis of the internal dynamics of R1 reported in Ch. 3, we know that the rarest dynamical event in this system is the transition of the disulfide torsion angle χ_3 between its two energetically preferred values of $\pm 90°$. The additional analysis, presented below, confirms that the slowest relaxation time in Fig. 4.1(a) is associated with the flip of χ_3. The absence of a similar slow time scale in Fig. 4.1(b) indicates that the information regarding the state of χ_3 is lost when the conformation of R1 is projected to the space of the Euler angles. Based on this observation, we conclude that the Euler angles do not constitute good order

parameters for the description of the dynamics of R1 on a poly-alanine α-helix, and do not consider them further.

In Fig. 4.1(a), the time scales τ_i show relatively little dependence on the lag time τ, indicating that the jump dynamics among the K-means clusters are approximately Markovian. Nevertheless, when plotted on a linear scale, some of the $\tau_i < 5$ ns are seen to rise throughout the whole examined range of τ without reaching a plateau (Fig. 4.2(a)). A context dependent analysis is expected to alleviate this problem. A HMM with 120 microstates was constructed analizing the time series of the five dihedral angles with a lag time $\tau = 100$ ps. The probability densities for observing a certain combination of the torsion angles, given the state of the Markov chain, were chosen as in Eq. (4.26). The initial estimates of $\boldsymbol{\mu}_i$ were taken to coincide with the positions of the K-means centroids, determined in the previous step. The starting covariance matrices $\boldsymbol{\Sigma}_i$ were also calculated according to the membership assigned by the K-means clustering. The parameters of the HMM were optimized using Eqs. (4.31) and (4.32). At the end of each iteration, microstates with less than 100 snapshots assigned to them, were removed. Convergence was assumed when each of the entries of the TPM changed by less than 10^{-3} in an iteration. After convergence, the Viterbi algorithm was used to generate time series of the hidden states, which were then used to estimate TPMs for integer multiples of the lag time used in the optimization. The time scales $\tau_i < 5$ ns, of the obtained TPMs are shown in Fig. 4.2(b). Comparison with the same time scales estimated directly from the K-means clustered trajectories (Fig. 4.2(a)) reveals that the time scales determined from the HMM are less dependent on τ and attain their asymptotic values at much shorter lag times.

In Table 4.1, we compare the slowest 14 time scales τ_i, calculated using $P(\tau)$,

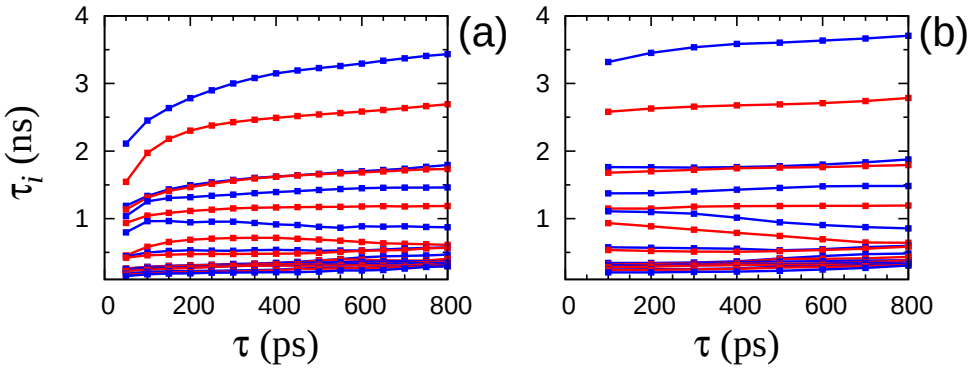

Figure 4.2: Time scales τ_i $(4 \leq i \leq 22)$ of the transition matrices $P(\tau)$ estimated from the time series produced by (a) the K-means clustering and (b) the Viterbi algorithm after a HMM optimization with $\tau = 100$ ps. The five linker dihedral angles were used as order parameters.

determined at $\tau = 100$ ps, either (i) directly by the HMM optimization (P), or (ii) from the microstate trajectories generated with the Viterbi algorithm (traj.). For all practical purposes, the two alternatives appear to be basically identical. The presence of gaps between the relaxation time scales τ_i implies the existence of relatively weakly coupled sub-blocks in the Markov chain [31, 32, 48]. From the gaps in Figs. 4.1(a) and 4.2(b), it is clear that the conformational dynamics of R1 can be understood as a hierarchy of Markov chains with 2, 4, 6, 14, etc. number of macrostates. Which one of those chains to choose will depend on the desired temporal resolution.

We constructed Markov models with $M = 6$, 14, 23, and 27 macrostates. During the optimization, the microstate properties $\boldsymbol{\mu}_i$ and Σ_i, were fixed and not allowed to change. The weights w_{ai}, with which microstate i contributes to the macrostate a, were optimized using the iterative procedure presented in Sec. 4.2.2. Convergence was assumed when each of the entries of the estimated TPM changed

Table 4.1: The time scales τ_i (ns), for models with 120, 6 and 14 states, calculated using $\tau = 100$ ps.

	$N = 120$		$M = 6$		$M = 14$	
i	traj.	P	flow	$\tilde{P}$	flow	$\tilde{P}$
1	70.8	70.8	67.8	70.1	68.5	70.4
2	10.8	10.8	8.29	9.60	8.50	10.0
3	8.85	8.81	7.90	8.23	8.14	8.46
4	3.32	3.26	1.67	3.10	2.19	3.78
5	2.58	2.55	1.12	2.14	1.40	2.86
6	1.76	1.74	-	-	1.22	1.78
7	1.68	1.66	-	-	1.00	1.72
8	1.37	1.37	-	-	0.89	1.36
9	1.15	1.14	-	-	0.88	1.21
10	1.11	1.10	-	-	0.84	0.99
11	0.93	0.92	-	-	0.59	0.59
12	0.58	0.57	-	-	0.27	0.54
13	0.54	0.53	-	-	0.26	0.51
14	0.34	0.34	-	-	-	-

by less than 10^{-4} in an iteration. The required initial weights were assigned according to the lumping method of [140], which is extremely simple from a computational point of view. It groups microstates together in a macrostates using sharp membership. w_{ai} was intialized to 1 if a microstate i belonged to a macrostate a, and to 0.01 if it did not. These starting weights were normalized to satisfy Eq. (4.19).

The time scales of the transition matrices determined after the convergence

of the HMM procedure are shown in Table 4.1 for the first two models ($\tilde{P}$). In addition, the time scales of the transition matrices, calculated from Eq. (4.24) from the sharp clustering of [140] are also shown (flow). Since this clustering was used to initialize the weights w_{ai}, the difference between the two sets of time scales is an indicator of the improvement offered by the HMM versus the lumping with sharp membership. From this perspective, it is seen that for both $M = 6$ and $M = 14$ the improvement is significant, and allows the models to faithfully capture the slow dynamics of the detailed $N = 120$ model.

4.3.2 Analysis of the conformations

Having gained confidence that the constructed Markov models with different number of macrostates are able to capture the slow dynamics of the spin label, we examine the implications the macrostates carry regarding the conformations of R1. The hierarchical emergence of Markov models with 2, 4 and 6 states is followed in Table 4.2. As expected, the division of states in the 2-state model is based on the value of χ_3. The populations of the $\chi_3 \approx -90^\circ$ and $\chi_3 \approx +90^\circ$ macrostates are estimated to be 88 % and 12 %, respectively (last row of Table 4.1). The time scale associated with the flip of the disulfide dihedral is determined to be $\tau_1 \sim 70$ ns. This is the slowest event in the internal dynamics of the spin label R1, when it is situated at the middle of a poly-alanine α-helix. Since this time scale is expected to be largely determined by the dihedral energy barrier of χ_3 (about 7 kcal/mol) [63], the slow rate of exchange between the two conformations of the disulfide torsion angle is most likely a general characteristic of R1 at solvent-exposed sites in proteins. In the 4-state model, each of the $\chi_3 \approx \pm 90^\circ$ states is itself split in two: states with $\chi_1 \approx 60^\circ$ separate from the others. Such conformations place the S_γ of

Table 4.2: The characterization of the Markov models with 2, 4 and 6 states in terms of the dihedral angle conformations. The lifetimes of the states, from Eq. (4.12), are in bold.

χ_3	$-90°$				$+90°$		:2
χ_1	$-60°, 180°$			$+60°$	$-60°, 180°$	$+60°$	:4
χ_2	$180°$		$-60°, +60°$				
a	I[a]	II	III	IV	V	VI	:6
σ_a (ns)	**2.4**	**6.1**	**5.2**	**9.8**	**55**	**8.7**	
$\tilde{\pi}_a$ (%)	6.0	43.6	37.0	1.5	11.4	0.5	
	88.1%				11.9%		

[a]This macrostate contains two microstates (the two black points in Figs. 4.3(a) and 4.3(b)), which have very similar values for all the five dihedrals, $\boldsymbol{\mu}_i \approx (-170°, 160°, -95°, 75°, -100°)$.

the spin label side chain in a sterically unfavorable position against the backbone atoms of the α-helix. According to the 6-state model, the populations of these states are barely a few percent (Table 4.2), in agreement with the data for cysteine side chains on α-helices, for which $\chi_1 \approx 60°$ is seen only 5% of the time [84]. These conformations of R1 are expected to be poorly populated at solvent-exposed sites in α-helices. The time scales τ_1 ($\sim$ 100 ns), and τ_2, τ_3 ($\sim$ 10 ns) indicate that the populations of the two χ_3 conformers and of the $\chi_1 \approx 60°$ conformations, as well as the rates of their exchange, will be among the hardest to sample reliably in atomistic MD simulations. Certainly, for R1 at a general solvent-exposed site, there could be additional conformations which might be equally hard to sample. The remaining time scales of the internal R1 dynamics, according to the Markov models, are faster than 4 ns. From Table 4.2, the slowest two of them ($\tau_4 \approx 3.5$ and $\tau_5 \approx 2.5$ ns) appear to be related to conformations with $\chi_2 \approx 180°$ and $\chi_3 \approx -90°$.

In Table 4.3 we show the populations of the 14-state model. To facilitate the presentation, the probabilites of the macrostates have been renormalized based on the χ_3 conformation to which they belong. The projection of the centroids $\boldsymbol{\mu}_i$, to the χ_1–χ_2 and χ_5–χ_4 planes, for microstates whose membership to a given macrostate is larger than 0.8, are shown in Fig. 4.3. The microstates in a given macrostate are much more similar in terms of their χ_1 and χ_2 dihedrals, than in terms of χ_4 and χ_5. Even though localized, the projections of the macrostates on the χ_1–χ_2 plane are somewhat irregular, and, especially in the χ_2 direction, extend well beyond the ideal positions ($\pm 60^\circ$ and 180°) expected for a torsion angle with multiplicity of 3. A few microstate centroids have $\chi_2 \approx \pm 120^\circ$, which would constitute barriers for the ideal dihedral. In Fig. 4.4 we show the R1 conformations corresponding to some of the $\boldsymbol{\mu}_i$'s from Fig. 4.3. The major source of intra-macrostate disorder is seen to be related to the last two dihedrals of the spin label side chain. At the same time, one of the shown microstates in macrostate 2 has a different χ_1 value from the others. Since the 14-state model lumps together conformations with exchange time faster than half a nanosecond ($\tau_{13} \approx 0.5$ ns in Table 4.1), this indicates that it is possible to have relatively fast flips of χ_1. The TPMs of the 6- and 14-state models are shown in Fig. 4.5. The states on the left-hand side correspond to $\chi_3 \approx -90^\circ$, those on the right-hand side to $\chi_3 \approx 90^\circ$. Bidirectional transitions between the two sets of conformations involve macrostates 2 and 9 (cf. Fig. 4.4). A unidirectional transition is seen to connect macrostate 13 to 6. The states with $\chi_1 \approx 60^\circ$ are also observed to be connected to the others through one-way transitions. One-way transitions in the probability matrix are due to the limited number of transitions out of or into the states present in the MD trajectories.

Table 4.3: Populations (%) and lifetimes (ns) of the 14-state Markov model, normalized separately for conformations with $\chi_3 \approx -90°$ (states 1 to 7), and $\chi_3 \approx 90°$ (states 8 to 14). The states with $\chi_1 \approx 60°$ are indicated with a star.

state #	1	2	3*	4*	5	6	7	tot.
popul.	26.8	49.0	0.9	0.8	6.8	9.3	6.4	100.0
lifetime	**3.8**	**5.9**	**1.3**	**1.0**	**1.4**	**2.4**	**2.6**	
state #	8	9	10*	11*	12*	13	14	tot.
popul.	34.1	34.0	0.1	0.4	3.6	14.1	13.7	100.0
lifetime	**2.4**	**1.3**	**1.1**	**0.7**	**3.6**	**1.7**	**0.8**	
color[a]	red	green	blue	purple	cyan	yellow	black	

[a]Used in Figs. 4.3 and 4.4.

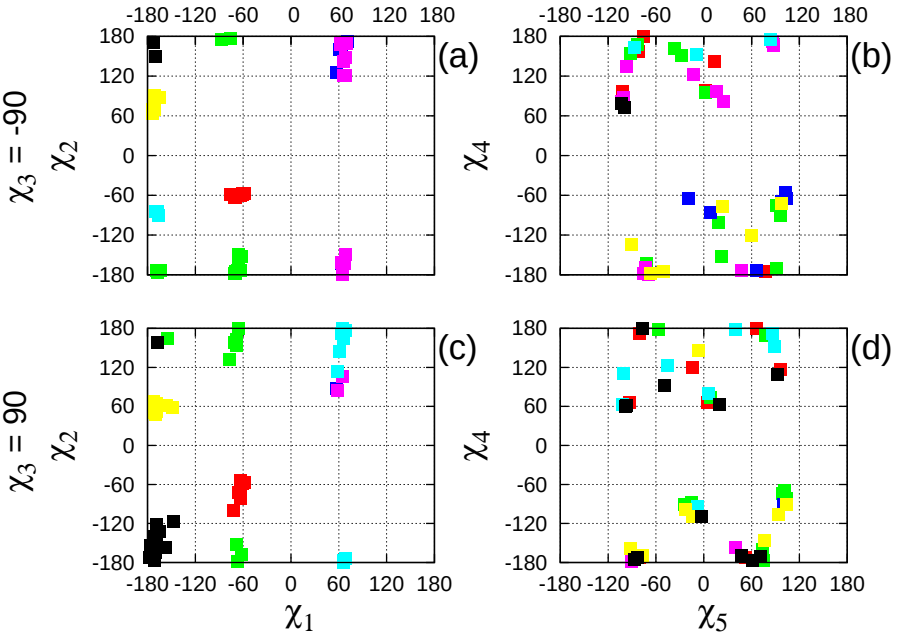

Figure 4.3: Positions of the 120 mean vectors $\boldsymbol{\mu}_i$ projected to the χ_1–χ_2 and χ_5–χ_4 planes (colored according to the scheme in Table 4.3).

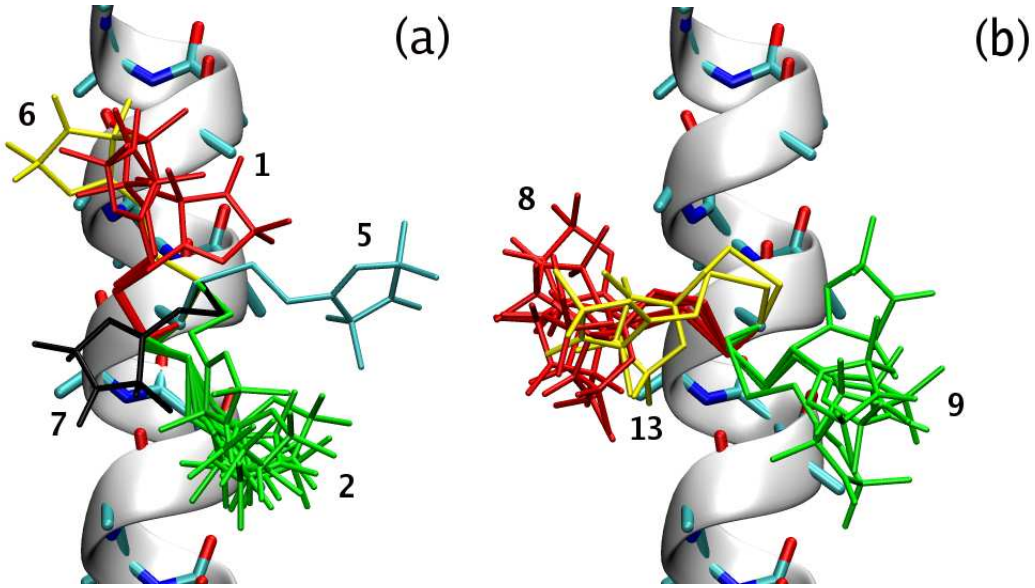

Figure 4.4: Spin label conformations corresponding to the microstate centroids $\boldsymbol{\mu}_i$, which have $\pi_i > 1.2\%$ and belong to macrostates with $\tilde{\pi}_a > 6.0\%$ (according to the renormalized probabilities in Table 4.3). The macrostates are numbered and colored following the convention of Table 4.3. (a) $\chi_3 \approx -90°$ conformations, (b) $\chi_3 \approx 90°$.

4.3.3 Multifrequency ESR spectra

We intend to compare spectra simulated using the stochastic jump trajectories according to the motional model

$$\mathtt{L} \xrightarrow{\text{rot. diff.}} \mathtt{M} \xrightarrow[\text{chain}]{\text{Markov}} \mathtt{N} \tag{4.58}$$

with spectra simulated directly from the MD trajectories according to

$$\mathtt{L} \xrightarrow{\text{rot. diff.}} \mathtt{M} \xrightarrow{\text{MD traj.}} \mathtt{N}. \tag{4.59}$$

In these diagrams, $\mathtt{N}$ is the coordinate system attached to the spin label, $\mathtt{M}$ is the coordinate frame attached to the helix, and $\mathtt{L}$ is the stationary lab-fixed frame.

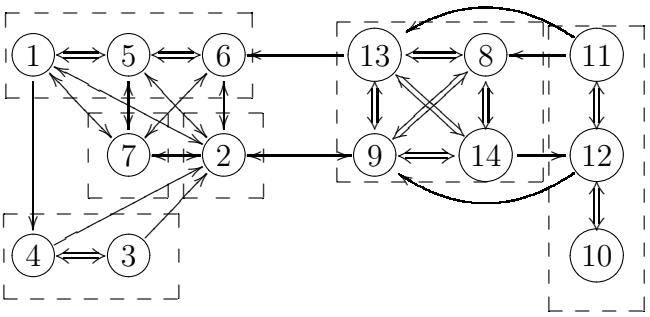

Figure 4.5: The hierarchical structure of the TPM for the 6-state (dashed boxes) and 14-state (circles) models. The correspondence between the states is as follows: I = $\{7\}$, II = $\{2\}$, III = $\{1, 5, 6\}$, IV = $\{3, 4\}$, V = $\{8, 9, 13, 14\}$, and VI = $\{10, 11, 12\}$. Intra-macrostate transitions for the 6-state model are indicated with block arrows and correspond to larger transition probabilities. The directions of the arrows indicate the directions of the transitions observed in the trajectories.

Rotational Brownian diffusion of `M` with respect to `L`, with diffusion coefficient $D = 18 \times 10^6$ s^{-1}, is introduced to represent the tumbling in solution of a small soluble protein like T4 Lysozyme. The dynamics of the spin label with respect to the helix are accounted for by the trajectories of either the Markov models or the MD simulations. The details of the numerical propagation of the quantal dynamics and the stochastic rotational diffusion were given in Ch. 2. As in Ch. 3, when spectra were simulated for the model (4.59), the numerical propagation of the quantal spin dynamics was carried with a time step Δt, chosen according to the strength of the magnetic field (Table 4.4). The MD trajectories were used to calculate average magnetic tensors for the successive time intervals of duration Δt. To account for the low viscosity of the TIP3P water model used in the MD simulations, the time axis was stretched by a factor of 2.5. Since the MD snapshots were saved every 1 ps, time-averaged magnetic tensors were calculated by averaging over 'avgN' successive snapshots (Table 4.4). The quantum integration was initialized at time intervals separated by 2 ns along each of the MD trajectories, which corresponds

Table 4.4: Parameters used in the simulation of the ESR spectra from the MD and the Markov chain trajectories.

field (T)	Δt (ns)	avgN	lagN	sphN	T_{L}^{-1} (G)	M
0.33	2.0	800	1	400^a	0.8	14
3.40	0.5	200	4	3200^b	1.2	23
6.09	0.4	160	5	6400^b	2.2	27

[a]Twice as many points were used with the Markov trajectories.
[b]Four times more points were used with the Markov trajectories.

to 'lagN' number of Δt steps. The columns 'sphN' and T_{L}^{-1} in Table 4.4 list, respectively, the number of spherical grid points used for the initial conditions of the isotropic diffusion, and the Lorentzian broadening introduced in the calculation of the spectra. The magnetic tensors were taken to be

$$\begin{aligned} \mathsf{g}^{\mathtt{N}} &= \mathrm{diag}(2.00809, 2.00585, 2.00202) \\ \mathsf{A}^{\mathtt{N}} &= \mathrm{diag}(6.2, 4.3, 36.9), \end{aligned} \tag{4.60}$$

in agreement with the values used in Ch. 3.

When spectra were simulated with the Markov model (4.58), we used the time intervals Δt of Table 4.4 as an indicator of the minimal temporal resolution the model was expected to provide. The (approximate) number of required macrostates, was determined by examining the eigenvalues of the $N = 120$ microstate model. Three such values, corresponding to time scales slower than, respectively, 0.8, 0.2 and 0.16 ns (after accounting for the 2.5 scaling of the time axis), are listed in the last column of Table 4.4. For each of the models, trajectories were generated with the macrostate transition matrix $\tilde{P}(\tau)$ estimated at $\tau = 100$ ps. As a result, the time step of the numerical integration was 0.25 ns (again scaling by 2.5) for the motional model (4.58). 200 trajectories were simulated per spherical

grid point.

The direct comparison between the two motional models (4.59) and (4.58) is encumbered due to the differences in the relative populations of the states as determined from the MD trajectories and from the Markov model. The populations of the two χ_3 conformations, for example, are present in a 2:1 ratio in the MD trajectories, as discussed in Ch. 3, whereas the 6-state model gives a ratio of 22:3 (Table 4.2). The latter number takes into account not only the total time spent in each state (2:1), which for non-ergodic trajectories is heavily determined by the initial conditions, but also the ratio of the number of observed p→m and m→p transitions (4:1), which is exactly why the Markov modeling is used in the first place. Hoping to circumvent this complication, we simulate and compare spectra for conformations with $\chi_3 \approx -90°$ and 90° separately. Based on the time scales in Table 4.1, we expect the sampling inside each of these two conformations to be approximately ergodic.

Recently, multifrequency spectra at 9.5, 95 and 170 GHz (0.33, 3.4 and 6.09 T) have been reported for R1 at position 131 in T4 Lysozyme [35]. Motivated by this study, we compare spectra simulated using the Markov state trajectories (in color) and the MD trajectories (black lines) for the three field strengths (Fig. 4.6). Spectra from models with number of states estimated to be sufficient for a given field strength (column M in Table 4.4) lie along the diagonal running from the upper left corner to the lower right corner of Fig. 4.6. These are seen to be essentially identical to the spectra below the diagonal for all the three field strengths, indicating convergence with respect to the number of Markov states. In comparison, the spectra above the diagonal (from models with less states than necessary) exhibit sharper features. This is a well known effect in simulations

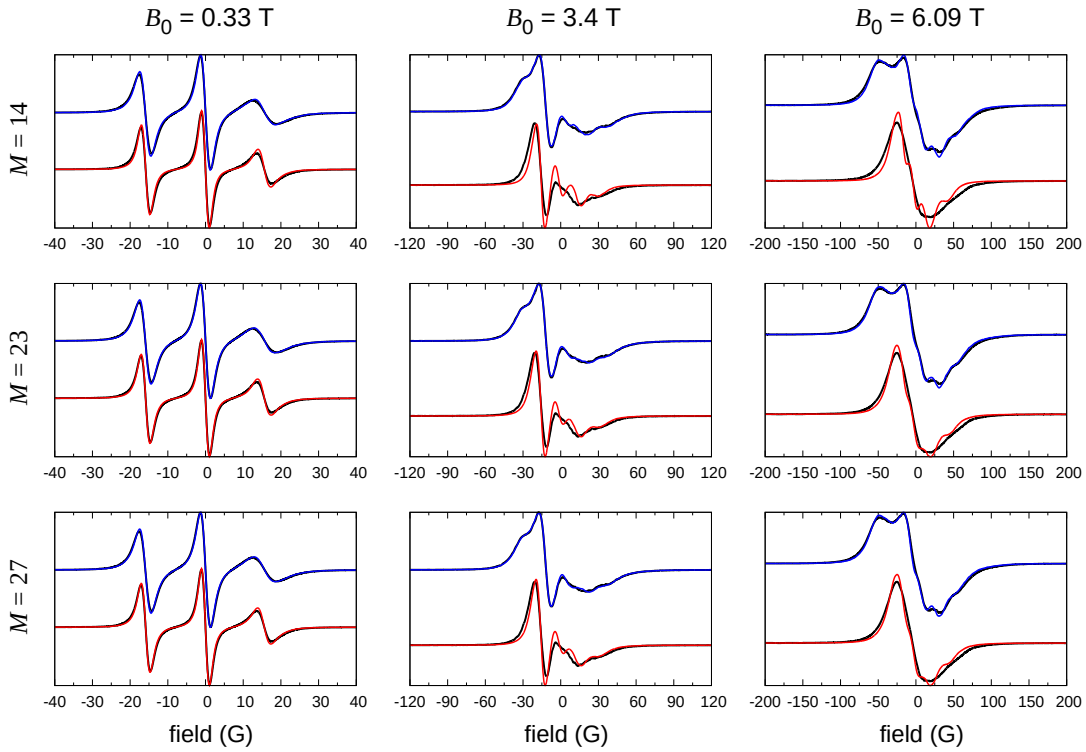

Figure 4.6: Comparison of spectra at 9, 95 and 170 GHz ($B_0 = 0.33$, 3.4 and 6.09 T, respectively) simulated using the MD trajectories (black lines) and the stochastic trajectories (colored lines), generated with a 14-, 23- and 27-state Markov models. In each figure, spectra simulated from the $\chi_3 \approx -90°$ and $\chi_3 \approx 90°$ subblocks of the full transition probability matrix are shown, respectively, at the top (blue) and bottom (red). The effect of overall tumbling with isotropic rotational diffusion $D = 18 \times 10^6$ s^{-1} is included in each spectrum.

based on average Hamiltonians (also called effective Hamiltonian) [27, 89]. For all fields, the agreement between the spectra simulated using the MD and the Markov trajectories is rather good for the $\chi_3 \approx -90°$ conformations. The spectra of the $\chi_3 \approx 90°$ conformations, on the other hand, show systematic differences: at all fields the Markov chain dynamics appear to be somewhat faster than the dynamics in the MD trajectories.

4.4 Concluding discussion

A systematic method for constructing Markov chain models from the MD trajectories of the spin label R1, using the values of its dihedral angles as order parameters, was presented. Starting from numerous clusters, determined by the K-means clustering algorithm, we gradually walked our way to Markov modles with reduced number of states. At every stage of our procedure we formulated the problem as an inference of a HMM, and relied on the probabilistic framework developed for such models [112]. The states of the constructed Markov models were examined to gain an insight into the metastable conformations of the spin label R1 on a poly-alanine α-helix. Stochastic trajectories were generated using the estimated TPMs, and used to simulate ESR spectra at three different field strengths.

To overcome the problem of the artificially imposed inter-state relaxation (the matrix A in Eq. (4.25)), Kube and Weber relax the requirement that $\tilde{P}(\tau)$ should be a stochastic matrix [72, 73]. They construct a coarse-grained matrix $\tilde{P}(\tau)$, for which the two steps of lumping and propagation commute for any τ. Unfortunately, the resulting $\tilde{P}(\tau)$ lacks probabilistic interpretation since it has negative matrix elements, which makes it inappropriate for generating stochastic trajectories to be used in the simulation of ESR spectra. To estimate a legitimate stochastic matrix $\tilde{P}(\tau)$, we decided to analyze the data successively with two HMMs: the first, suited for the initial step of projecting the snapshots into a Markov jump model with many states, the second, for the lumping step. The motivation to use HMMs came from the work of Horenko *et al.* [55, 56, 93], in which a HMM with overdamped, diffusive dynamics inside each of the hidden states was developed.

Recently, a procedure for the automatic identification of macrostates that exchange according to Markov chain kinetics, from MD trajectories, has been pro-

posed [24]. In consists of repeated identification of microstates with K-medoid clustering, followed by their lumping into macrostates. At every new iteration, the K-medoid clustering is applied separately to the data that has been lumped into a macrostate in the previous step. Once new microstates have been constructed, the macrostate boundaries are dissolved and built again from scratch. The intention is that the repeated application of these two steps will result in microstates that lack internal structure and in macrostates that unite these microstates in the kinetically most meaningful way. The lumping in [24] is performed according to the TPM estimated by pure counting (according to Eq. (4.9)). Counting short-lived excursions accross macrostate boundaries as genuine transitions, leads to apparent memory at short lag times. This effect is significantly reduced if such excursions are identified, and treated accordingly by using a HMM, as demonstrated in the context of R1 on a poly-alanine α-helix (Fig. 4.2) Other, less demanding and more practical alternatives should be also possible. Certainly, the extent to which sharp macrostate boundaries and their fast recrossings are a problem, will depend on the time scale separation between the intra-macrostate equilibration and inter-macrostate dynamics. Nevertheless, our analysis of the internal spin label dynamics suggests that it might be worthwhile to extend the automatic strategy of [24] to allow for probabilistic membership and context-dependent treatment of the data.

Previously, MD trajectories of the spin label R1 have been used to construct stochastic models of its dynamics [7, 19, 133]. In all of these studies, the Euler angles Ω, describing the orientation of the nitroxide-fixed frame `N` with respect to the macromolecular frame `M`, were used as order parameters. In [133] and [7] the Euler angle space was partitioned into bins of width 3.6° along each of the three angles, and a potential of mean force $U(\Omega)$ was calculated by counting how many

times the MD snapshots fall into a given bin. Diffusive Brownian dynamics were run with forces cacluated from $U(\Omega)$. In [19], $U(\Omega)$ was assumed to depend only on two out of the three Euler angles, which allowed for its expansion in terms of spherical harmonics. The expansion coefficients were then determined from a least-squares fit of the analytical potential to the logarithm of the normalized histogram built from the MD snapshots.

The unrealistically fast dynamics in Fig. 4.1(b), when compared with Fig. 4.1(a), indicates that by monitoring the values of the Euler angles one is insensitive to the state of the disulfide torsion angle χ_3. When the regions of Ω accessible to the two conformations of χ_3 overlap, a memoryless model in which decision about where to go to next is based solely on the current values of the Euler angles, can easily cross to the other conformation. In such cases, it is not legitimate to build a Markovian (memoryless) model, since the true dynamics depend on degrees of freedom which are not explicitly accounted for. It is possible that for restricted spin labels, for which certain values of Ω are accessible only from unique structural conformations, the dynamics projected onto the Euler angles could provide a faithful representation of the internal spin label dynamics. For R1 at solvent-exposed helix surface sites, though, our results suggest that the Euler angles are not good order parameters to characterize its internal dynamics. From that perspective, the potential of mean force $U(\Omega)$, even though accessible computationally, is largely irrelevant for the dynamics of R1 at such sites.

In Fig. 4.4 we saw that the inter-macrostate disorder was mainly due to variation in the values of the last two dihedrals χ_4 and χ_5. At first glance, this might look as a support of the χ_4/χ_5 model, proposed to rationalize the internal dynamics of R1 relevant for the ESR spectra [26, 27]. According to the model, the

transitions of χ_1, χ_2 and χ_3 are too slow to be dynamically relevant for the ESR spectra. Thus, the deviation of the spectral line shape from the rigid limit is mainly due to transitions of χ_4 and χ_5. The time scales presented in Table 4.1, and the characterization of the states in Table 4.2, suggest that only the time scale associated with the χ_3 transition falls in the rigid limit, whereas all the others are on the order of 10 ns or faster. Hence, the segmental motion of all the dihedrals, except χ_3, has the potential to contribute to the deviation of the spectrum away from the rigid limit.

The Markov chain analysis of the R1 conformations and their time scales of mixing identified the exchange between the states with different values of χ_3 and the populations of the states with $\chi_1 \approx 60^\circ$ as the hardest to sample reliably in free MD simulations. (Additional slow events are not ruled out for R1 at solvent-exposed sites in proteins.) In spite of the sampling problem that these events pose, they do not hinder the simulation of ESR spectra. As already pointed out in Ch. 3, due to the rather slow exchange rate of the two χ_3 conformers, the decay of the magnetization from each of them can be added linearly to obtain a spectrum for all frequencies including, and beyond, 9 GHz. Thus, their relative populations can be left as a free parameter of mixing and determined by fitting the simulated spectrum to an experimental one. In addition, even though the exact populations of the $\chi_1 \approx 60^\circ$ conformations and their rates of exchange might be largely uncertain, their influence on the spectra is probably insignificant because the populations are expected to be rather small in absolute terms for R1 at solvent-exposed sites on α-helices.

In the simulation of the ESR spectra we used only the average values of the magnetic tensors in a given macrostate, based on the result of Sec. 4.2.3 summa-

rized by Eq. (4.57). This equation is only valid to zeroth order in the expansion parameter ϵ. Another term, proportional to the integral of the correlation function of the Liouvillian, appears when the analysis is carried to next order in ϵ. It is the famous relaxation operator in the Redfield theory of relaxation [114, 115]. In [138], for example, the relaxation operator was calculated assuming overdamped torsional oscillations of R1. In principle, this term can also be included in the time domain propagation of the spin dynamics, performed in this chapter. There is a significant difference, though, between the average Liouvillian in Eq. (4.57) and the relaxation operator. Whereas the former corresponds to an average Hamiltonian in the Hilbert space of the problem, the latter necessitates the quantal propagation to be carried in Liouville space. As was demonstrated in Ch. 2, propagating the density matrix in the Hilbert space is preferable from a computational point of view. Therefore, we avoid using a relaxation operator by introducing larger number of macrostates such that dynamics on sufficiently fast time scales is explicitly present.

Markov chain models constructed from MD trajectories of the spin label dynamics, hold the potential of bridging the wide gap between atomistic MD simulations of solvated spin labeled proteins and their experimental ESR spectra. They provide a rigorous probabilistic framework for utilizing the information from many, relatively short MD trajectories toward a single, coherent model of the spin label dynamics. Not using the MD trajectories directly for the simulation of the spectra, removes the burden, imposed by the slow decay of the transverse magnetization (hundreds of nanoseconds at 9 GHz), on the duration of a single dynamical trajectory. Using the MD trajectories to estimate *conditional*, transition probabilities, makes it possible to use many (tens or hundreds), relatively short (tens of nanoseconds) simulations. Calculating realistic ESR spectra, in quantitative

similarity with experiment, from atomisitc MD simulations of a spin labeled protein, is therefore expected to become a feasible task in the very near future. The framework developed in this chapter is applied in Ch. 5 to the dynamics of R1 on solvent-exposed sites in T4 Lysozyme.

4.5 Imposing detailed balance and the HMM estimation

4.5.1 How to impose detailed balance

A legitimate TPM P in detailed balance with its equilibrium probability vector π can be constructed from any symmetric matrix with non-negative entries. Let S be such a matrix and

$$s_i \equiv \sum_j S_{ij} \tag{4.61}$$

are its row sums. Then,

$$P_{ij} = \frac{S_{ij}}{s_i} \quad \text{and} \quad \pi_i = \frac{s_i}{\sum_i s_i} \tag{4.62}$$

are in detailed balance. This observation forms the basis of two different strategies for imposing detailed balance on transition matrices estimated from the data. In the first one, the available MD trajectories are analized both forward and backward in time, thus counting a forward $j \to i$ transition also as a backward $i \to j$ transition. With this understanding, the forward-backward ($\leftrightarrow$) transition count matrix becomes

$$\overleftrightarrow{N}^{\tau}_{ij} = \left(N^{\tau}_{ij} + N^{\tau}_{ji}\right)/2, \tag{4.63}$$

which is symmetric by construction. Therefore, the matrix $\overleftrightarrow{P}(\tau)$ built from it by row normalization is automatically in detailed balance with its equilibrium

eigenvector $\overleftrightarrow{\pi}$. In the second alternative [36], $P(\tau)$ is built from the forward counts only according to Eq. (4.9). Then, its stationary eigenvector π is calculated. Since the forward transition count matrix is not necessarily symmetric, $P(\tau)$ and π need not be in detailed balance. They are used to build the symmetric matrix

$$S_{ij} = (\pi_i P_{ij} + \pi_j P_{ji})/2, \tag{4.64}$$

from which new $\overrightarrow{P}(\tau)$ and $\overrightarrow{\pi}$, in detailed balance with each other, are formed according to Eq. (4.62)

In each of these two ways the information present in the transition count matrix is utilized in a qualitatively different fashion. For concreteness, let us consider a two-state Markov model. Suppose that the simulated trajectories of the model result in

$$N^\tau = \begin{pmatrix} 200 & 5 \\ 3 & 800 \end{pmatrix}, \tag{4.65}$$

for some lag time τ. This means that the total time spent in the states is 200τ and 800τ, respectively. Also, the trajectories contain five $1 \to 2$ and three $2 \to 1$ transitions. Following the first procedure, we build the forward-backward count matrix

$$\overleftrightarrow{N}^\tau = \begin{pmatrix} 200 & 4 \\ 4 & 800 \end{pmatrix}, \tag{4.66}$$

for which $\overleftrightarrow{P}_{12} \approx 4/200$ and $\overleftrightarrow{P}_{21} \approx 4/800$. The equilibrium probabilities for the two states follow from the detailed balance condition, Eq. (4.10). For their ratio one finds

$$\overleftrightarrow{\pi}_1 / \overleftrightarrow{\pi}_2 = \overleftrightarrow{P}_{21} / \overleftrightarrow{P}_{12} \approx \frac{4/800}{4/200} = 1/4. \tag{4.67}$$

In the second case, $\overrightarrow{P}_{12} \approx 5/200$ and $\overrightarrow{P}_{21} \approx 3/800$. The detailed balance condition gives

$$\overrightarrow{\pi}_1 / \overrightarrow{\pi}_2 = \overrightarrow{P}_{21} / \overrightarrow{P}_{12} \approx \frac{3/800}{5/200} = 3/20, \tag{4.68}$$

which agrees with what is obtained from constructing

$$S = \begin{pmatrix} 120 & 3 \\ 3 & 800 \end{pmatrix} \tag{4.69}$$

using Eq. (4.64), and calculating $\overrightarrow{\pi}$ from Eq. (4.62). Clearly, the two ways of imposing detailed balance lead to drastically different equilibrium probabilities.

More careful examination of the two procedures reveals the source of the difference. Symmetrizing N^τ according to Eq. (4.63) makes sure that the number of $i \to j$ and $j \to i$ transitions are the same, without changing the diagonal terms. Since the number of transitions typically is much smaller than the numbers along the diagonal, such symmetrization basically implies that the ratio of the equilibrium probabilities will be dominated by the ratio of the diagonal elements, as was the case in Eq. (4.67). The ratio of the diagonal terms simply reflects the frequencies of observing the chain in each of its states over all of the available trajectories. For non-ergodic trajectories, these frequencies do not correspond to the thermodinamic Boltzamnn weights of the states, but are dominated by the state in which the trajectories were started. When only forward transitions are counted, the number of $i \to j$ and $j \to i$ transitions are not necessarily equal. In this case, the ratio of the equilibrium probabilities implied by the TPM depends not only on the ratio of the diagonal terms but also on the ratio of the observed transitions, as seen in Eq. (4.68). From this example it becomes clear that the forward-backward counting scheme presupposes that the available trajectories are ergodic and visit the states of the chain according to the equilibrium probabilities. When only relatively short trajectories are available, which is the situation that we deal with, the forward-only counting scheme uses the scarce but valuable information present in the off diagonal elements of N^τ together with the total times spent in each state (the diagonal elements) to estimate a more meaningful equilibrium

probability vector.

4.5.2 Details about the HMM estimation

Forward and backward variables

Let

$$O_{t:s} = \boldsymbol{O}_t \boldsymbol{O}_{t+1} \dots \boldsymbol{O}_{s-1} \boldsymbol{O}_s, \qquad 1 \leq t < s \leq T, \tag{4.70}$$

denote the sequence of observations from time step t to time step s, and $O = O_{1:T}$ indicate the entire sequence of observations. The forward variables

$$\alpha_i(t) = \mathbb{P}\{X_t = i, O_{1:t} | \theta\} \tag{4.71}$$

correspond to the conditional probability of observing the sequence of observations up to time t and being in state i at time t, given the parameters of the model. They can be calculated efficiently as

$$\begin{aligned} \alpha_i(1) &= p_i b_i(\boldsymbol{O}_1) \\ \alpha_j(t) &= \sum_{i=1}^{N} \alpha_i(t-1) P_{ij} b_j(\boldsymbol{O}_t), \quad 1 < t \leq T. \end{aligned} \tag{4.72}$$

The backward variables

$$\beta_i(t) = \mathbb{P}\{O_{t+1:T} | X_t = i, \theta\}, \tag{4.73}$$

are the conditional probabilities of observing the sequence $O_{t+1:T}$, given the parameters of the model and that the (hidden) state at time t is i. They can also be calculated recursively as

$$\begin{aligned} \beta_i(T) &= 1 \\ \beta_i(t) &= \sum_{j=1}^{N} P_{ij} b_j(\boldsymbol{O}_{t+1}) \beta_j(t+1), \quad T > t \geq 1. \end{aligned} \tag{4.74}$$

Once the forward and backward variables are known it is easy to calculate the conditional probability of observing the whole sequence of observations O, given the parameters of the model:

$$\mathbb{P}\{O|\theta\} = \sum_{i=1}^{N} \alpha_i(T) = \sum_{i=1}^{N} \alpha_i(t)\beta_i(t). \tag{4.75}$$

The last equality holds for any $1 \leq t \leq T$. Also, $\gamma_i(t)$ and $\xi_{ij}(t)$, defined in Eqs. (4.30) and (4.28), respectively, can be calculated as

$$\gamma_i(t) = \frac{\alpha_i(t)\beta_i(t)}{\mathbb{P}\{O|\theta\}}. \tag{4.76}$$

and

$$\xi_{ij}(t) = \frac{\alpha_i(t)P_{ij}b_j(\boldsymbol{O}_{t+1})\beta_j(t+1)}{\mathbb{P}\{O|\theta\}}. \tag{4.77}$$

Scaling

The forward and backward variables, as defined above, become exponentially smaller with increasing T. For numerical purposes it is necessary to work with slightly different variables. Let us start by introducing the scaling factors

$$\begin{aligned} c(1) &= \mathbb{P}\{\boldsymbol{O}_1|\theta\} \\ c(t) &= \mathbb{P}\{\boldsymbol{O}_t|O_{1:t-1},\theta\}, \qquad 1 < t \leq T, \end{aligned} \tag{4.78}$$

in terms of which

$$\mathbb{P}\{O_{1:t}|\theta\} = \prod_{\tau=1}^{t} c(\tau). \tag{4.79}$$

A non-vanishing (scaled) forward variable can be defined as

$$\bar{\alpha}_i(t) = \mathbb{P}\{X_t = i|O_{1:t},\theta\}, \tag{4.80}$$

whose relation to the original forward variable is

$$\bar{\alpha}_i(t) = \frac{\mathbb{P}\{X_t = i, O_{1:t}|\theta\}}{\mathbb{P}\{O_{1:t}|\theta\}} = \frac{\alpha_i(t)}{\prod_{\tau=1}^{t} c(\tau)}. \tag{4.81}$$

It is this product of many terms in the denominator that, for large T, leads to vanishingly small forward variables beyond machine precision. The remedy is to work with the $\bar{\alpha}_i(t)$s and $c(t)$s instead of the original $\alpha_i(t)$s. From the definition of $c(t)$ one can write

$$\begin{aligned} c(t) &= \sum_{i,j} \mathbb{P}\{X_{t-1} = i | O_{1:t-1}, \theta\} P_{ij} b_j(\boldsymbol{O}_t) \\ &= \sum_{j,i} \bar{\alpha}_i(t-1) P_{ij} b_j(\boldsymbol{O}_t). \end{aligned} \tag{4.82}$$

In terms of the auxiliary variable

$$\tilde{\alpha}_j(t) \equiv \sum_{i=1}^{N} \bar{\alpha}_i(t-1) P_{ij} b_j(\boldsymbol{O}_t), \qquad 1 < t \leq T, \tag{4.83}$$

this yields,

$$c(t) = \sum_{j=1}^{N} \tilde{\alpha}_j(t). \tag{4.84}$$

Substituting Eq. (4.81) into Eq. (4.72) and using Eq. (4.83) gives

$$\bar{\alpha}_j(t) = \tilde{\alpha}_j(t)/c(t). \tag{4.85}$$

These equations allow us to calculate the sacaled forward variables and the scaling coefficients recursively. The procedure starts with $\tilde{\alpha}_i(1) = \alpha_i(1)$. Defining scaled backward variables as

$$\bar{\beta}_i(t) \equiv \frac{\beta_i(t)}{\prod_{\tau=t}^{T} c(\tau)}, \tag{4.86}$$

the recursion Eq. (4.74) becomes

$$\begin{aligned} \bar{\beta}_i(T) &= 1/c(T) \\ \bar{\beta}_i(t) &= \frac{1}{c(t)} \sum_{j=1}^{N} P_{ij} b_j(\boldsymbol{O}_{t+1}) \bar{\beta}_j(t+1), \qquad T > t \geq 1. \end{aligned} \tag{4.87}$$

In terms of the scaled variables one has

$$\begin{aligned} \gamma_i(t) &= c(t) \bar{\alpha}_i(t) \bar{\beta}_i(t) \\ \xi_{ij}(t) &= \bar{\alpha}_i(t) P_{ij} b_j(\boldsymbol{O}_{t+1}) \bar{\beta}_j(t+1), \end{aligned} \tag{4.88}$$

which can be easily obtained from Eqs. (4.30) and (4.28) using Eq. (4.79) with $t = T$.

The Viterbi algorithm

Once the parameters of the model are optimized one can find the best state sequence $X_1 X_2 \dots X_T$ corresponding to the observation sequence O. This is achieved using the following three step procedure known as the Viterbi algorithm [112]:

$$\begin{cases} \delta_i(1) = p_i b_i(\boldsymbol{O}_1) \\ \psi_i(1) = 0 \end{cases} \tag{4.89a}$$

$$\begin{cases} \delta_j(t) = \max_i\{\delta_i(t-1)P_{ij}b_j(\boldsymbol{O}_t)\} \\ \psi_j(t) = \text{argmax}_i\{\delta_i(t-1)P_{ij}\}, \quad 1 < t \leq T \end{cases} \tag{4.89b}$$

$$\begin{cases} X_T = \text{argmax}_i\{\delta_i(T)\} \\ X_t = \psi_{X_{t+1}}(t+1), \quad T > t \geq 1. \end{cases} \tag{4.89c}$$

CHAPTER 5

DYNAMICS AND ESR SPECTRA OF A NITROXIDE SPIN LABEL AT SOLVENT-EXPOSED SURFACE SITES IN T4 LYSOZYME

5.1 Introduction

Electron spin resonance (ESR), in combination with site-directed spin labeling (SDSL), is a powerful biophysical technique that has been successfully used for probing protein conformation in native—aqueous or membrane—environments, and its changes during protein function [12, 14–17, 29, 33, 61, 99, 102–104, 131, 132]. When a nitroxide spin label is successively placed at all possible positions along the entire protein sequence, overall trends and general patterns across all the recorded spectra provide qualitative information about the secondary protein structure and the orientation of its subunits relative to each other or to the solvent [29, 103, 104]. Quantitative analysis of spectra from a few strategically selected spin-labeled sites on the protein of interest, is required to measure long-range distances (10–70 Å) [12, 15–17, 99]. The specific features of each spectral line shape need to be carefully understood and interpreted when detailed information is sought.

Since the protein environment manifests itself in the ESR spectrum through modulation of the internal spin label dynamics, relating the specifics of a given spectrum to the local protein dynamics and structure calls for close familiarity with the behavior of the reporter itself, and for means to rigorously evaluate its effect on the spectral line shape. Considerable effort has gone into characterizing the conformational dynamics of the spin label MTSSL, most commonly used in SDSL of proteins. Following the genral convention, we refer to the "side chain" resulting from the reaction of MTSSL with a cysteine residue as R1 (Fig. 5.1). In addition

to ESR spectroscopy [27, 82, 90, 91], calculation of ESR spectra [4, 27, 28, 44, 50, 81] with the analytically tractable diffusional models MOMD [94] and SRLS [106, 107] and X-ray crystallography [44, 50, 51, 78] have been used to gain insight into the conformations and dynamic modes of R1. Spectra at several different strengths of the magnetic field have been used to probe the spin label dynamics [4, 35, 81], providing increased sensitivity to subtle motional features over multiple time-scale windows [80], ranging from tens of picoseconds to hundreds of nanoseconds. In many of these studies, T4 Lysozyme (T4L) has been employed as a model protein system (Fig. 5.1).

In the MOMD and SRLS models used to fit the experimental spectra, the rotation of the coordinate system attached to the nitroxide with respect to the coordinate system fixed on the protein, is modeled as a restricted Brownian diffusion in an ordering potential, which is expressed as a sum of spherical harmonics. Informed by the parameters of the MOMD model, four fundamentally different types of dynamic modes have been proposed for the side chain R1 with a simple, one-component spectrum: disordered, weakly ordered, strongly ordered, and immobilized [44]. Each dynamic mode is thought to be correlated with the local protein topology. The strongly ordered and the immobilized modes are observed at sites in which R1 is partially or fully buried [44]. At sites with weak ordering, on the other hand, R1 is believed not to be involved in tertiary interactions. For many such solvent-exposed surface sites in T4L, the X-band ($\sim$9 GHz) ESR spectra suggest that the anisotropic motion of the spin label is independent of interactions with the neighboring side chains on the same helix [90, 91].

The diffusion in a cone-like potential, assumed for the internal dynamics of R1 by the MOMD/SRLS model, could reflect the correct spin label dynamics, but

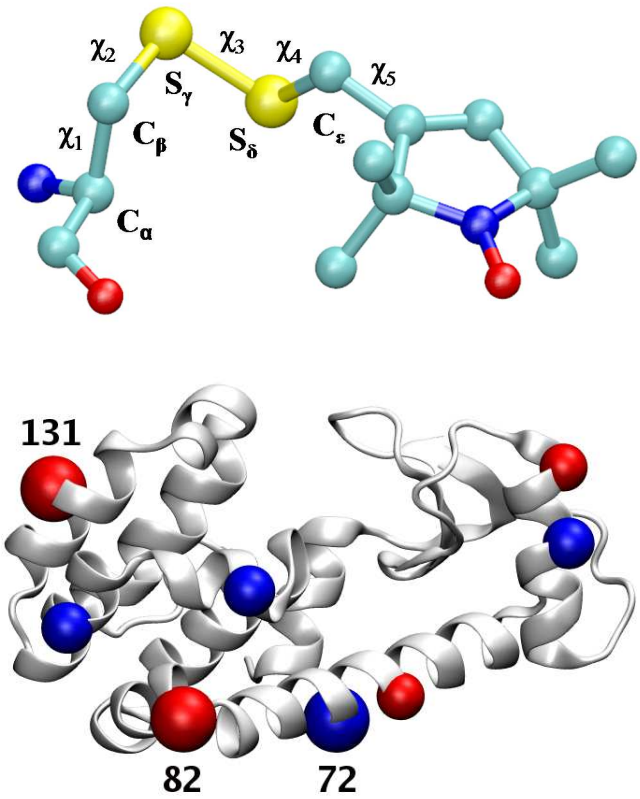

Figure 5.1: Top: The "side chain" R1, resulting from linking MTSSL to a cysteine through a disulfide bond. Bottom: Cartoon representation of T4 Lysozyme. Spin labels were present simultaneously at same-color sites in simulation set 1 (blue) or 2 (red). Only the sites studied in this work are numbered. The figures were drawn with VMD [59].

not necessarily. Diverse experimental data, summarized as the χ_4/χ_5 model [28], have sought to establish a direct, structural link between the actual microscopic dynamics of R1 and the MOMD/SRLS model [26, 27]. According to the χ_4/χ_5 model, the internal dynamics of R1 that affect the spectrum are dominated by torsional motion about the last two dihedrals, χ_4 and χ_5 (Fig. 5.1). It is assumed that the remaining three dihedrals are effectively immobilized on the ESR time scale; χ_1 and χ_2 due to a C_α–H$\cdots S_\delta$ interaction [26–28, 44], χ_3 as a result of the

relatively high energy barrier for the disufide dihedral (about 7 kcal/mol [63]). The two components of the MOMD/SRLS rotation tensor ($D_{\|}$ and $D_{\perp}$) are assumed to correspond approximately to rotations about χ_4 and χ_5 [27, 28, 44]. Rotations about χ_5 are proposed to be slightly more restricted due to steric clashes of the S_δ with the nitroxide ring substituents, explaining the intra-residue origin of the MOMD/SRLS ordering potential [27, 44]. The MOMD/SRLS model with a single set of parameters (i.e. single spectral component) is not always sufficient to fit the experimental spectrum. Better fits are achieved when two, independent spectral components are mixed in some ratio, leading to a two-component spectrum.

Crystallographic X-ray structures of spin-labeled T4L provide additional experimental information about the conformations of R1 at solvent-exposed sites [44, 50, 78]. Implicitly, the χ_4/χ_5 model has been taken to imply a one-to-one correspondence between a single spectral component, sufficient to fit the observed spectrum with the MOMD/SRLS model, and a conformation of R1 as resolved in a crystal structure (up to disorder in the last two dihedrals). While it is possible that this effective motional model reflects the actual dynamics of the spin label, it appears that more complicated motions could also give rise to the same spectral features, as exemplified by 131R1 for which the crystal structure (pdb id: 2CUU) [44] shows electron density for two sets of (χ_1, χ_2) combinations, while a single-component spectrum is observed.

In spite of the increasing availability of crystal structures and of multifrequency ESR spectra, the number of relevant spin label conformations, the molecular nature of the interactions that stabilize them, the time scales of their interconversion, and the effect of these factors on the ESR spectra have remained elusive. In principle, molecular dynamics (MD) simulations could be used to reveal all these aspects and

to link them to the experimental observations. In practice, it is beyond the current capabilities of MD simulations, which use atomic detail and explicit solvation, to sample exhaustively the conformational freedom of a spin label. Previous MD studies of spin labeled proteins have either simplified the description [7,19,119,133] (e.g. using implicit solvent, or simulating at 600 K), at the expense of distorting the energetics and dynamics to an uncertain degree, or have failed to use the MD trajectories to calculate ESR spectra [96, 134], leaving the relation between the simulated dynamics and the spectra unclear.

The methodological prerequisites for performing all-atom MD simulations of proteins spin labeled with MTSSL, and calculating multifrequency ESR spectra using the MD simulations were developed in the previous chapters. To this end, the partial charges of the nitroxide ring and the torsional energetics of the R1 side chain were parametrized against *ab initio* target data in Ch. 3. A systematic procedure for mapping the internal R1 dynamics to a stochastic, Markov jump process was proposed in Ch. 4. Using the efficient numerical integrators that were developed in Ch. 2, the Markov jump model is easily combined with a rotational diffusion model, accounting for the global protein tumbling in solution, to calculate ESR spectra.

Here, this methodology is applied to a spin-labeled, soluble protein. We perform extensive, all-atom MD simulations of R1 in T4L and construct Markov chain models of the spin label dynamics. The models allow us to calculate realistic ESR spectra, reflecting both the internal R1 dynamics and the tumbling of the protein, and to compare with available electron densities. As a result, we are able to present an atomically-detailed picture of the behavior of R1 at solvent-exposed sites in proteins, which unifies the diverse spectroscopic and crystallographic data

by providing insight into their molecular origins.

5.2 Results and discussion

5.2.1 Two prototypical helix surface sites, 72 and 131

Sites 72 and 131 in T4L are located in the middle of, respectively, a long and a short helix (Fig. 5.1). At both positions, R1 is not expected to be involved in tertiary contacts. In addition, X-band ESR spectra show insignificant changes upon mutation of the neighboring $i\pm3$, $i\pm4$ residues to alanine [91]. Contributions to the spectra from the local backbone flexibility are expected to be rather small for 72R1 and more significant for 131R1, due to the differences in the relative backbone rigidity inferred from the Debye-Waller factors in the T4L crystal structure [27,28]. Thus, 72R1 has emerged as a reference site which is believed to exhibit the internal dynamics of R1 in isolation [27, 28]. In comparison, the X-band spectra of 131R1 are thought to exemplify the effect of backbone motion on side chain mobility [27, 28].

MD simulations of fully-solvated, spin-labeled T4L were used to construct Markov chain models of R1 at those two sites, using the five spin label dihedrals as order parameters. Models of 72R1 and 131R1 with 11 and 12 states, respectively, provided temporal resolution of about 800 ps. Models with 37-38 states were necessary to go down to a time resolution of 160 ps, needed for the calculation of ESR spectra at high fields. The relaxation time scales of the finer models are shown in Fig. 5.2 as a function of lag time. The lines are expected to be horizontal if the dihedral time series can be faithfully modeled by a Markov

chain model. Markov jump dynamics are seen to be appropriate for both 72R1 and 131R1. At both sites, the slowest relaxation times ($\tau_1 \gtrsim 100$ ns) are related to transitions of the disulfide torsion angle between its two stable conformations $\chi_3 \approx -90^\circ$ (m) and $\chi_3 \approx 90^\circ$ (p). The exact numerical values of τ_1, as well as the relative populations of the m and p conformations, are expected to be poorly estimated due to the small number of such transitions observed in the simulations (Table 5.1). Fortunately, because of its excessive slowness, the precise value of τ_1 is immaterial for the calculation of ESR spectra at 9 GHz and at higher frequencies, since such spectra can be simulated as a linear superposition of spectra from the m and p conformations only.

By using the m and p sub-blocks of the estimated transition probability matrices separately, we simulated ESR spectra at three different magnetic field strengths (Figs. 5.3 and 5.4, left). Isotropic rotation, with diffusion coefficient appropriate for the tumbling of T4L in water, was introduced in addition to the Markov chain dynamics. The ratio at which the m and p conformers are present under experimental conditions can be conveniently determined by linearly mixing the two spectral line shapes and fitting to experimental spectra. The best global fits, obtained upon simultaneous variation of the m and p populations and the Lorentzian broadening, introduced in the simulations by hand, are presented in the middle column of Figs. 5.3 and 5.4. Experimental multifrequency ESR spectra of 72R1 and 131R1 have been published previously [35, 81], but we make use of recently obtained spectra with improved signal-to-noise [149].

For the three fields, the spectra from the m and p conformations of 131R1 are seen to be quite similar to each other and to the experimental spectra, with the difference increasing progressively with the increase of the field (Fig. 5.4, left). At

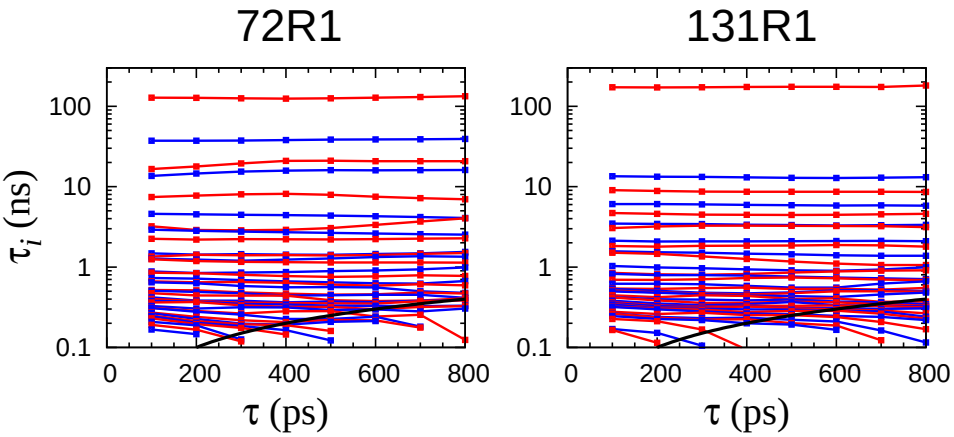

Figure 5.2: Relaxation time scales $\tau_i(\tau) = -\tau/\ln\lambda_i(\tau)$, implied by the eigenvalues, λ_i, of the transition probability matrices estimated from the data at various lag times τ. The thick black curves correspond to 2τ. τ_i's that fall under these curves are essentially zero and are poorly estimated.

Table 5.1: Number of transitions between conformers with $\chi_3 \approx -90°$ (m) and $\chi_3 \approx 90°$ (p) observed in all of the MD trajectories of the specified site.

transition	72	131	82
m→p	2	1	4
p→m	1	1	0

$B = 0.33$ T (9.5 GHz) both the m and p spectra are essentially identical to the experimental spectrum, therefore, they do not inform the mixing ratio (87% m vs. 13% p), estimated from the global fit, as much as the spectra at $B = 3.4$ and 6.1 T (95 and 170 GHz, respectively). The simultaneous fit to the multifrequency spectra indicates that about 90% of the spin label side chains at position 131 in T4L have $\chi_3 \approx -90°$ in solution at 22–24°C. The agreement between the calculated/fitted and the experimental spectra is seen to be remarkably good over the entire field

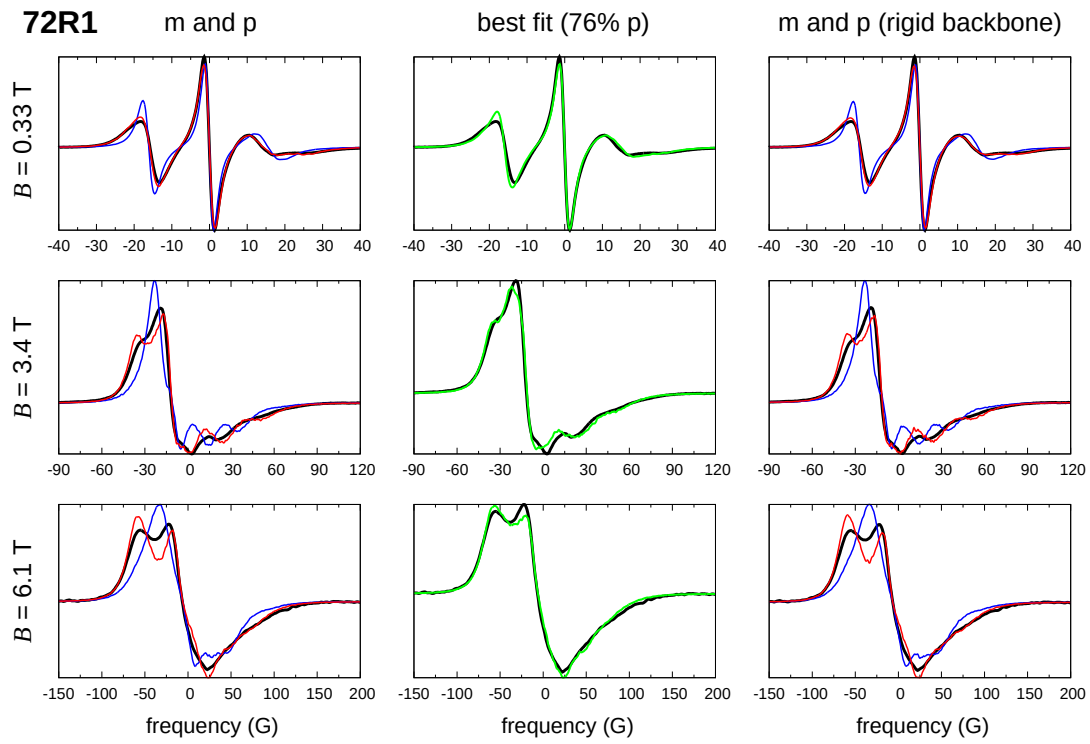

Figure 5.3: Experimental spectra of 72R1 at 22°C (black) are compared with, left: calculated spectra of the m (blue) and p (red) conformations; middle: best fitting spectra (green), achieved by varying the relative populations of the m and p conformations and the Lorentzian broadening; right: spectra for the m (blue) and p (red) conformations, in which the local backbone fluctuations were artificially removed. The simulation and fitting parameters are given in Table 5.2.

range (Fig. 5.4, middle). In the case of 72R1 the m and p contributions to the spectra are markedly different (Fig. 5.3, left), with the latter being consistently more similar to the experimental spectrum for all the three field strengths. At $B = 0.33$ T, the p component by itself is essentially identical to the experimental spectrum, whereas adding some fraction of the m component improves the fit at the two higher fields (Fig. 5.3, middle). Overall, the calculated/fitted spectra (with 24% m vs. 76% p) agree well with the experiment, but not to the same degree as

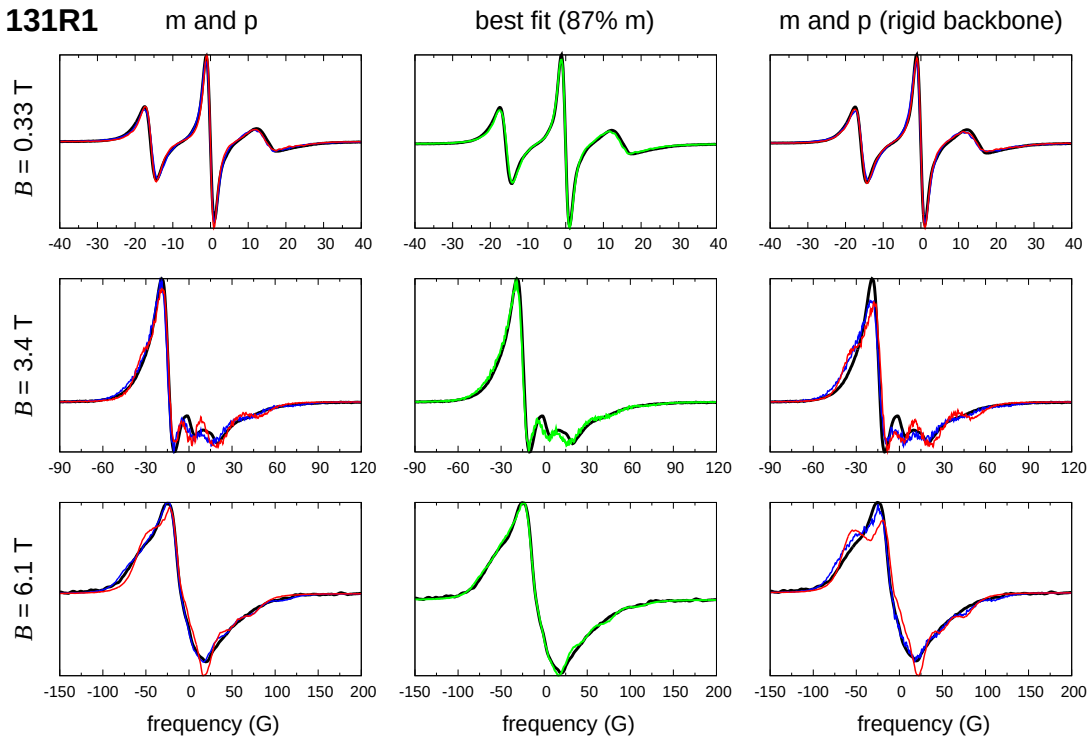

Figure 5.4: Same as Fig. 5.3 for 131R1.

131R1. The reason for this can be identified from the relaxation time scales in Fig. 5.2. Unlike 131R1, the dynamics of which exhibit a gap in the 15–100 ns time window, slow events, on the time scale of tens of nanoseconds, are present for 72R1. That R1 has longer-lived conformations at position 72 is even more apparent from the lifetimes of the Markovian states (Table 5.3). In fact, state A of 72R1 was reached in only one of the MD trajectories at about the 10th ns and was never left, thus it acted as a sink for the probability of the Markov chain. To ensure a well-behaved transition probability matrix, one artificial transition from state A to the state that led to it was introduced (see Sec. 5.3.2). As a result, both the population and the lifetime of this state are uncertain. Even though longer-lived, state D was left in four of the seven trajectories that reached it, thus it appears

Table 5.2: Parameters used in the simulation of the ESR spectra. The diffusive rotational dynamics of the macromolecule with respect to the lab-fixed frame was initialized from 'sphN' spherical grid points. 200 stochastic trajectories lasting for 'stpN' steps were launched from each grid point. A simulation time step of 200 ps was used with the Markov transition matrices estimated at $\tau = 100$ ps, where the 2-fold difference aims to correct for the unrealistically low viscosity of the TIP3P water model used in the MD simulations. T_{L}^{-1} denotes the Lorentzian broadenings yielding the best global fit to the experimental spectra.

			T_{L}^{-1} (G)	
B (T)	stpN	sphN	72R1	131R1
0.33	3000	800	0.6	0.2
3.40	2500	25600	0.7	0.2
6.10	2000	25600	1.7	1.6

to be sampled better. In any case, the amount of sampling, which directly affects the estimated populations and lifetimes of the states inside each of the m and p sub-blocks, appears to be less sufficient for 72R1 than for 131R1.

Differences in the X-band spectra of 72R1 and 131R1 have been proposed to result from differences in the backbone flexibility at these two sites [26–28]. We artificially removed the local backbone fluctuations present in the MD simulations (see Sec. 5.3.3) and calculated the corresponding multifrequency ESR spectra for the m and p conformers (Figs. 5.3 and 5.4, right). None of the spectra of 72R1 is affected by this procedure, whereas the spectra of 131R1 change dramatically. This result agrees with the intuitive expectation that, looking from the global coordinate frame attached to T4L, the local frame attached to the $i-4$ to $i+4$ helical segment is less ordered at $i = 131$ than at $i = 72$. At the same time, the effect of the local backbone fluctuations on the ESR spectrum is seen to be more pronounced at

Table 5.3: Lifetimes, $\sigma_i = \tau/(1 - P_{ii}(\tau))$, and populations, π_i, for states with $\sigma_i > 5$ ns and $\pi_i > 1\%$, calculated from the 11- and 12-state Markov models of 72R1 and 131R1, respectively. The m:p ratio was set to 1:1 for the reported π_i's.

	72R1				131R1			
	m		p		m		p	
state	A[a]	B[b]	C[c]	D[d]	E[e]	F[f]	G[g]	H[h]
σ_i (ns)	**22**	8.2	**15**	**58**	7.1	5.2	**11**	5.3
π_i (%)	2.9	35	13	36	16	14	25	8.2

[a] $(\chi_1, \chi_2, \chi_3, \chi_4) \approx (180°, -90°, -80°, 180°)$.
[b] $(\chi_1, \chi_2, \chi_3) \approx (-60°, -60°, -90°)$.
[c] $(\chi_1, \chi_3) \approx (-60°, 90°)$.
[d] $(\chi_1, \chi_2, \chi_3) \approx (-170°, 60°, 90°)$.
[e] $(\chi_1, \chi_2, \chi_3, \chi_4, \chi_5) \approx (180°, 180°, -90°, 70°, -100°)$.
[f] $(\chi_2, \chi_3) \approx (180°, -90°)$.
[g] $(\chi_1, \chi_2, \chi_3) \approx (-60°, -60°, 100°)$.
[h] $(\chi_1, \chi_2, \chi_3) \approx (60°, 180°, 90°)$.

95 GHz and higher frequencies, and to be essentially absent at X-band (Fig. 5.4, right). Therefore, when taking the local flexibility of the protein at the spin-labeled position into account is clearly crucial for the quantitative agreement of the calculated and experimental spectra, it does not explain the difference observed in the X-band spectra of 72R1 and 131R1.

Having determined the relative m and p populations from the spectral fits (about 75% p for 72R1 and 90% m for 131R1), we can proceed with the structural and energetic analysis of the conformations of 72R1 and 131R1 that are relevant in an aqueous environment at 24°C. The most populated seven Markovian states of 72R1 are presented in Table 5.4. The corresponding spin label conformations for the first five of them are shown in Fig. 5.5. In spite of the variation of χ_4 and χ_5, as well as χ_1, χ_2 and χ_3, across the most populated states, the nitroxide ring ap-

pears to be rather well localized, failing to explore a large volume of the potentially available conformational space. To establish the energetic causes of this localization, we calculated the interaction energies between the nitroxide ring, including C_ϵ and S_δ, and the neighboring amino acids—both side chain and backbone atoms (Table 5.5). The numbers clearly demonstrate that the ordering and localization of the nitroxide ring is due to the favorable van der Waals (vdW) contacts with the neighboring hydrophobic residues Phe4, Val75, Val71 and Ile3. Even the interactions with the polar Asn68 and the charged Arg76, when present, are mainly non-electrostatic. The result explains why alanine mutations at positions $i \pm 3$ and $i \pm 4$ failed to detect interactions of the spin label with its neighbors [90, 91]. Not only is the $i - 1$ residue and amino acids distant in the sequence involved in the interactions, but an alanine at positions $i - 4$ (N68A) and $i + 3$ (V75A) can also engage in nice hydrophobic contacts with R1 both in the m and p states, as was shown in the context of R1 on a poly-alanine α-helix (Ch. 3). The prevalence of the p conformations for 72R1 agrees with the observation that the m states of R1 can not establish vdW contacts with Ala at position $i - 1$, whereas the p states interact best with that position.

In contrast, the conformations corresponding to the first five most populated states of 131R1 are more spread around (Fig. 5.6(a)), although, pairwise, they share similar values for three out of the five spin label dihedrals (Table 5.6). The interactions that the spin label participates in are also quite varied both in nature and in the identity of the partner (Table 5.7). Since the electrostatic interactions were calculated in vacuum ($\epsilon = 1$), the relatively large interaction energies with distant amino acids, appearing in Table 5.7, are in fact less significant in the presence of water. The values are more representative when the spin label and its partner are in proximity, which can be inferred from the presence of a significant

Table 5.4: The seven most populated states of the Markov model of 72R1 with 25% m. The dihedral angles for two of the most probable microstates belonging to each state are shown. σ is the state lifetime (ns), $\tilde{\pi}$ and π (%) are the state and microstate populations. The cumulative probabilities are in parenthesis. The capital letters indicate to which coarse-grained state from Table 5.3 the state belongs to.

state	σ	$\tilde{\pi}$	π	χ_1	χ_2	χ_3	χ_4	χ_5
#1	1.5	22.9	21.4	−176	49	94	−82	100
D		(22.9)	1.4	−170	55	102	−65	97
#2	0.5	16.1	10.9	−168	48	85	−159	−70
D		(39.0)	3.0	−169	54	85	−169	−81
#3	0.3	14.1	4.1	−169	48	78	−144	20
D		(53.1)	3.9	−162	47	79	−170	88
#4	1.3	9.0	4.2	−63	−66	94	172	57
C		(62.1)	1.9	−65	−78	84	146	87
#5	0.9	7.8	1.2	−55	−44	−91	−178	−93
B		(69.9)	1.2	−62	−20	−85	−175	−20
#6	1.6	4.3	2.6	−70	−65	−92	77	−99
B		(74.2)	1.2	−57	−56	−90	107	−99
#7	0.6	3.9	1.8	−72	−66	−84	162	80
B		(78.1)	0.6	−75	−67	−83	173	96

Table 5.5: Interaction energies (kcal/mol) of 72R1 with the specified residues for the five most populated states in Table 5.4. The van der Waals and electrostatic contributions are shown separately. Energies larger than the thermal energy at room temperature (0.6 kcal/mol) are in bold.

state		I3	F4	N68	V71	V75	R76
	vdw	−0.2	**−1.3**	**−1.7**	**−1.6**	**−1.5**	**−1.7**
#1	elec.	−0.3	−0.6	0.2	0.0	−0.1	**1.1**
	total	−0.5	**−1.9**	**−1.5**	**−1.6**	**−1.7**	−0.6
	vdw	−0.5	**−1.4**	−0.5	**−1.2**	**−2.2**	**−1.2**
#2	elec.	−0.5	−0.2	−0.3	0.2	−0.1	**0.7**
	total	**−1.0**	**−1.6**	**−0.7**	**−1.0**	**−2.3**	−0.5
	vdw	**−0.7**	**−1.5**	−0.4	**−1.1**	**−2.2**	**−1.2**
#3	elec.	0.0	−0.1	−0.3	0.2	0.1	0.6
	total	**−0.7**	**−1.6**	**−0.7**	**−0.9**	**−2.1**	**−0.7**
	vdw	**−0.8**	**−1.6**	−0.5	**−1.6**	**−2.1**	−0.4
#4	elec.	0.0	0.0	−0.5	0.1	0.4	**1.0**
	total	**−0.8**	**−1.6**	**−1.0**	**−1.5**	**−1.7**	0.5
	vdw	**−0.9**	**−1.7**	−0.5	**−1.4**	**−2.0**	−0.3
#5	elec.	0.0	0.1	0.2	−0.4	0.3	1.5
	total	**−0.8**	**−1.6**	−0.3	**−1.8**	**−1.7**	**1.2**

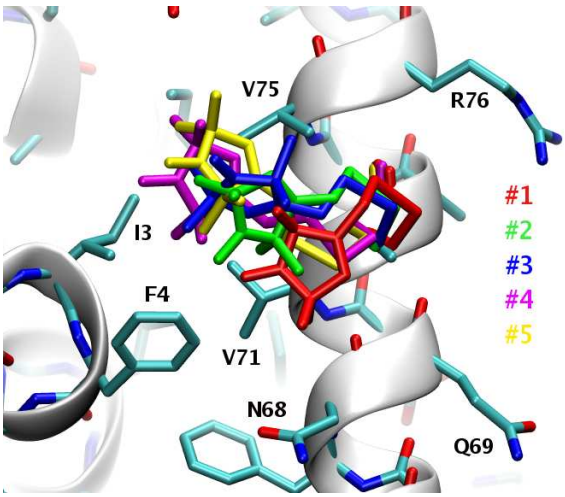

Figure 5.5: First five conformations of 72R1 from Table 5.4.

vdW interaction. Therefore, in Table 5.7, relatively large electrostatic interactions were highlighted only when the corresponding vdW interactions were also significant (i.e. larger than $k_{\mathrm{B}}T$). Interestingly, in its dominant state R1 appears to be involved in favorable electrostatic and vdW interactions with Arg154. The interaction energy remains significant even after accounting for the unfavorable electrostatic and favorable vdW interactions with Asp127. (The conformations of the side chains in Figs. 5.5, 5.6 and 5.8 are generic and do not necessarily reflect their true rotamers when interacting with R1.) Comparison of the interaction energies with Asp127 for states #1 and #2 reveals how the electrostatic interaction with charged amino acids can vary from unfavorable to favorable, depending on how the nitroxide oxygen and nitrogen atoms (partial charges of -0.44 and 0.22 in atomic units) are positioned with respect to the amino acid side chain. Again, the conformations, their interaction energies and comparison with the energetics of R1 on a poly-alanine α-helix help us understand why D127A, E128A and K135A mutations did not have a significant effect on the X-band spectra [44,91]. The latter residue is clearly not an important interaction partner. The m conformations of R1, deduced

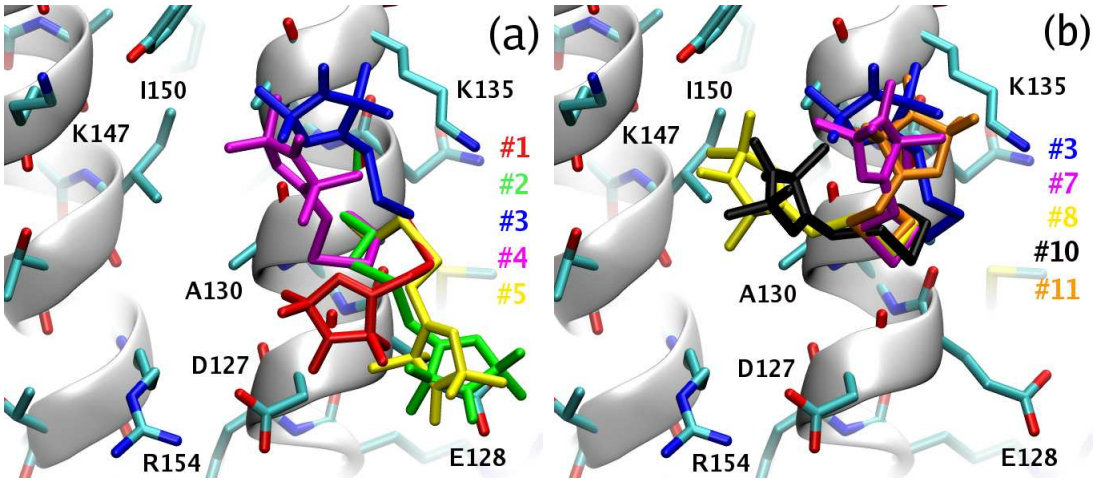

Figure 5.6: (a) Most populated five conformations of 131R1 from Table 5.6. (b) The set of conformations in Table 5.6 consistent with the recently solved crystal structure of 131R1 [44].

to be the most populated at this position (Table 5.2), were observed to establish favorable vdW contacts with alanines at position $i-4$ and $i-3$, the strength of which could be comparable to the interactions with Asp127 and Glu128. The ability of R1 to participate in diverse—hydrophobic and electrostatic—interactions simultaneously with several partners, makes it very hard to drastically change its environment through alanine mutations, especially since Ala itself might be an interacting partner at many of the $i \pm 3$, $i \pm 4$ positions. From that perspective, the changes of the spectra over several different frequencies are expected to be more informative about the effect mutations have on the behavior of R1.

Recently, the crystal structure of 131R1 was solved and densities were observed for rotamers corresponding to $(\chi_1, \chi_2) \approx (-60°, -60°)$ and $(180°, 60°)$, but not for the atoms of the nitroxide ring nor the C_ϵ, leaving the last three dihedrals undetermined [44]. Table 5.6 was intentionally extended to include the more probable states in the Markov model that exhibit dihedral angles consistent with the crys-

Table 5.6: Same as Table 5.4 for the Markov model of 131R1 with 90% m. Asterisk indicates states with (χ_1, χ_2) that agree with the values observed in the crystal structure at 100 K.

state	σ	$\tilde{\pi}$	π	χ_1	χ_2	χ_3	χ_4	χ_5
#1	7.0	30.1	28.0	−173	173	−96	72	−100
E		(30.1)	1.4	−171	−133	−103	74	−98
#2	0.8	12.8	7.8	−65	−177	−84	−174	−87
F		(42.9)	3.0	−70	−178	−95	174	−70
#3*	2.4	6.3	12.7	−171	66	−97	174	−63
		(55.6)	1.9	−171	73	−91	−159	−82
#4	0.9	7.7	4.3	−74	8	−89	173	−51
		(63.3)	2.1	−157	73	−93	141	−83
#5	0.5	7.1	3.9	−169	−179	−84	167	88
F		(70.4)	0.9	−173	−161	−85	166	50
#6	0.6	6.1	2.9	−64	−176	−82	−166	103
F		(76.5)	1.3	−65	−163	−85	−99	91
#7*	0.8	5.5	2.5	−66	−57	−83	166	83
		(82.0)	2.1	−68	−52	−80	160	−69
#8*	1.3	4.0	1.8	−62	−48	101	−161	77
G		(86.0)	1.2	−62	−53	102	−169	53
#9	1.4	2.0	1.2	−170	−93	−85	−175	−86
		(88.0)	0.8	−167	−94	−88	176	58
#10*	0.5	1.6	0.6	−58	−58	97	173	−83
G		(89.6)	0.4	−61	−60	97	163	−24
#11*	0.6	1.4	1.2	−64	−60	−91	85	−101

Table 5.7: Same as Table 5.5 for some of the states of 131R1 from Table 5.6.

	D127	E128	A130	A134	K135	Y139	K147	I150	R154
	−2.4	**−1.5**	**−0.8**	−0.1	−0.4	0.0	0.0	−0.1	**−1.8**
#1	**4.3**	0.6	−0.2	0.1	0.8	0.3	0.3	0.1	**−4.5**
	1.9	**−1.0**	**−1.0**	−0.1	0.4	0.2	0.3	0.0	**−6.3**
	−1.9	**−2.7**	−0.2	0.0	−0.1	0.0	0.0	0.0	−0.2
#2	**−1.9**	**−2.7**	0.2	−0.1	0.6	0.1	0.4	1.3	1.3
	−3.8	**−5.5**	0.0	−0.2	0.5	0.1	0.4	**1.3**	**1.0**
	−0.1	−0.1	−0.4	**−1.8**	**−2.2**	**−1.4**	−0.2	−0.2	−0.1
#3*	−0.6	−2.1	−0.4	**0.7**	**2.6**	0.3	−0.2	0.1	0.3
	−0.7	**−2.2**	**−0.8**	**−1.1**	0.4	**−1.1**	−0.3	0.0	0.2
	−0.2	−0.1	−0.5	**−1.3**	**−1.7**	**−0.8**	−0.1	−0.1	−0.2
#7*	−0.2	−0.9	−0.1	0.4	**1.5**	0.2	−1.0	0.1	−0.2
	−0.5	**−1.1**	**−0.7**	**−1.0**	−0.2	−0.6	**−1.1**	−0.1	−0.4
	−0.7	−0.2	**−2.0**	**−1.2**	−0.2	**−1.5**	**−1.7**	**−1.6**	**−1.6**
#8*	**−2.7**	−0.7	0.2	0.4	0.4	0.1	**−5.4**	−0.1	**2.0**
	−3.3	**−0.9**	**−1.8**	**−0.8**	0.1	**−1.4**	**−7.1**	**−1.7**	0.3
	−0.6	−0.2	**−1.7**	**−1.0**	−0.3	**−1.2**	**−1.0**	**−1.0**	**−1.6**
#10*	−1.9	−0.9	0.1	0.5	0.4	0.2	**−4.7**	−0.1	**1.8**
	−2.5	**−1.1**	**−1.6**	−0.5	0.1	**−1.0**	**−5.8**	**−1.1**	0.2
	−0.3	−0.2	−0.5	**−1.1**	**−2.1**	−0.4	0.0	−0.1	−0.2
#11*	−0.4	−0.9	0.0	0.3	**−4.1**	2.4	−1.0	0.0	0.1
	−0.6	**−1.1**	−0.6	**−0.9**	**−6.2**	**2.0**	**−1.1**	−0.1	−0.1

tallographic data. The corresponding conformations are shown in Fig. 5.6(b), and their interaction energies in Table 5.7. Direct comparison between the MD simulations and the electron densities is hindered by the fact that the diffraction data were collected at 100 K. Nevertheless, the $(\chi_1, \chi_2) \approx (-60°, -60°)$ conformations in Fig. 5.6(b) illustrate how knowledge of the first two dihedrals does not imply a unique value of χ_3, in agreement with missing electron density for C_ϵ. Two of those conformations, #8 and #10, are seen to reside close to Lys147, where they form favorable electrostatic interaction. The other two, #7 and #11, manage to position the nitroxide ring in a way similar to the well-populated #3, but with different values for χ_1 and χ_2. Interestingly, significant electrostatic interactions with either Lys147 or Lys135 are present for states #8, #10 and #11. Such interactions could be further facilitated in the frozen crystal environment, which is expected to have a lower dielectric constant than bulk water.

5.2.2 82R1: weakly ordered, loop surface site

Residue 82 in T4L is positioned at a short, two-residue loop (Fig. 5.1). At this site, R1 is nicely exposed to the solution. A crystal structure of T4L with 82R1 has been solved to 1.7 Å resolution (pdb id: 2CUU [44]). Electron density is present for the spin label side chain up to S_δ when the density map is examined with a cutoff of 2σ, fixing the values of χ_1 and χ_2. Density for C_ϵ becomes visible at a cutoff to 1.5σ, constraining χ_3. At smaller cutoffs the first carbon atom of the nitroxide ring is also resolved. The resulting conformation of R1, $(\chi_1, \chi_2, \chi_3, \chi_4) = (-68°, -56°, 101°, 94°)$, was observed to place the nitroxide ring close to the protein surface, which was argued to overly restrict the torsional freedom of χ_4, compared to what would be expected from the χ_4/χ_5 model based on the MOMD fit of

the 9.5 GHz spectrum [44]. As a result, it was concluded that, very likely, the conformation in the crystal structure did not reflect the room temperature state of R1 but corresponded to the immobilized component observed in the spectrum of 82R1 at low temperature. [44]

A Markov chain model was constructed from the MD trajectories of 82R1 (Fig. 5.7). The absence of any p→m transitions in the trajectories (Table 5.1) makes it impossible to rigorously estimate the ratio of the m and p populations. Nonetheless, having four transitions in the opposite direction suggests that p should be more populated. Somewhat arbitrarily, we chose to mix the two in a ratio of 1:9. The most populated states, their conformations and interaction energies are presented in Table 5.8, Fig. 5.8 and Table 5.9, respectively. Unlike 72R1 and 131R1, in which the spin label preferentially adapted conformations that place the nitroxide ring in close contact with the protein surface, R1 is seen to extend fully into the solution in its most probable state at position 82. This state must be preferred entropically, since it lacks both vdW and electrostatic interactions (Table 5.9). More compact states, supported by contacts with Arg80, Asn81 and Lys85 are also highly probable. Analysis of the Markov states allows us to conclude that the electron densities observed at 100 K reflect a spin label conformation relevant at 24°C (Table 5.10). Indeed, about 30% of the time the spin label is in a conformation with $(\chi_1, \chi_2, \chi_3) \approx (-60°, -60°, 90°)$, and more than 15% of the time in the state for which density was observed. For each of the first four dihedrals, the values implied by the electron densities are more probable than the other possible values across all the states (Table 5.10). At the same time, the MD simulations indicate that the spin label is able to explore a large number of rotameric states, in spite of the fact that its 9.5 GHz spectrum can be fit with only one MOMD spectral component. [44] Support for this observation comes from

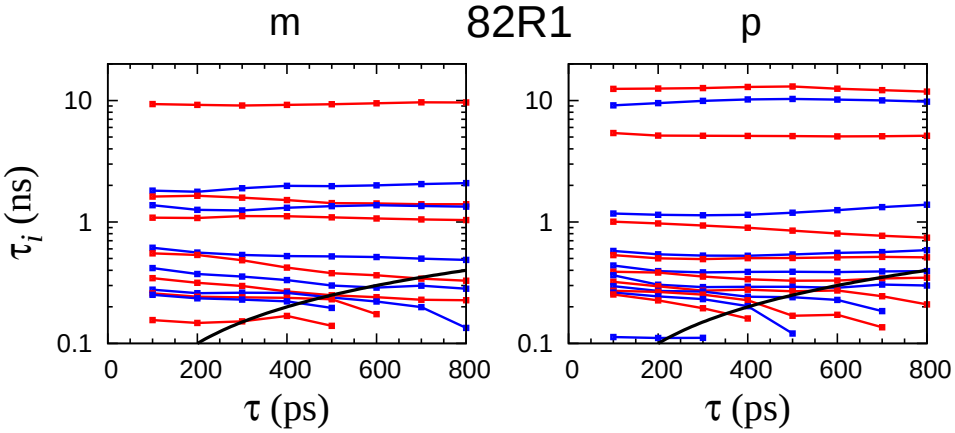

Figure 5.7: Relaxation time scales for the m (14 states) and p (17 states) conformations of the 31-state Markov model of 82R1.

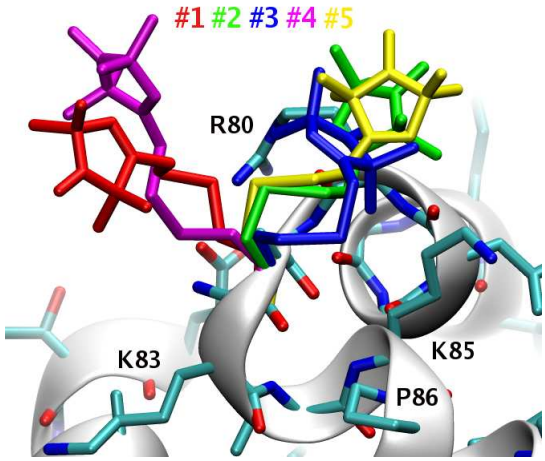

Figure 5.8: Conformations of 82R1 for the states in Table 5.8.

the crystal structure itself, which at 1.5σ cutoff clearly shows electron density corresponding to $\chi_1 \approx 60°$. This value of χ_1 is known to be very unlikely for R1 at sites on α-helices, since it positions S_γ uncomfortably against the backbone hydrogen-bond partners supporting the helical structure. Evidently, $\chi_1 \approx 60°$ is populated by 82R1, which is located in a loop.

Table 5.8: Same as Table 5.6 for the Markov model of 82R1 with 90% p. Asterisk indicates states with dihedrals that agree with the values observed in the crystal structure at 100 K.

state	σ	$\tilde{\pi}$	π	χ_1	χ_2	χ_3	χ_4	χ_5
#1	0.8	17.3	4.7	−60	178	86	−177	−83
		(17.3)	3.1	−60	176	86	179	83
#2*	0.7	16.0	5.6	−61	−60	101	89	−98
		(23.2)	3.0	−60	−107	85	63	20
#3	1.5	9.8	6.5	−163	54	91	−80	105
		(32.0)	3.3	−177	44	81	−109	101
#4	1.2	8.6	2.1	60	178	86	−178	70
		(40.6)	1.4	59	173	85	−178	−88
#5*	0.6	7.5	4.2	−60	−61	98	126	98
		(69.9)	3.2	−54	−64	98	164	86

5.2.3 Conclusion

Traditionally, 72R1 and 131R1 on T4L have epitomized the spin label dynamics at solvent-exposed sites on α-helices for which the spin label was assumed not be involved in tertiary interactions. [26] The difference between their X-band spectra has been proposed to reflect differences in the local backbone dynamics. [26] Our results demonstrate that the behavior of R1 at these two positions is much more complex than commonly believed. Due to its amphipathic nature, the nitroxide ring of the spin label appears to utilize every possibility to establish a van der Waals contact with a hydrophobic residue or form a salt bridge with a charged one. The length of the linker allows R1 to extend its range of exploration beyond its immediate neighbors on the helix (e.g. Phe4 and Arg154 for 72R1 and 131R1,

Table 5.9: Same as Table 5.5 for the states of 82R1 from Table 5.8.

state		R80	N81	K83	K85	P86
	vdw	−0.2	−0.2	−0.3	−0.2	−0.1
#1	elec.	0.8	−0.2	0.6	1.0	−0.1
	total	0.6	−0.4	0.3	**0.8**	−0.3
	vdw	**−2.1**	**−1.3**	−0.2	**−1.6**	−0.4
#2*	elec.	−0.4	−0.2	0.8	0.0	0.2
	total	**−2.5**	**−1.4**	0.6	**−1.6**	−0.2
	vdw	**−1.8**	**−1.6**	−0.3	**−1.9**	**−0.7**
#3	elec.	**−2.6**	0.3	0.3	**−2.7**	0.0
	total	**−4.4**	**−1.3**	−0.1	**−4.7**	**−0.7**
	vdw	−0.2	−0.3	**−0.8**	−0.1	−0.1
#4	elec.	0.5	0.2	0.2	0.4	0.5
	total	0.3	−0.1	−0.6	0.3	0.5
	vdw	**−2.7**	**−1.3**	−0.2	**−1.6**	−0.1
#5*	elec.	−0.6	−0.1	2.0	**3.3**	0.0
	total	**−3.3**	**−1.4**	**1.8**	**1.7**	−0.2

respectively). Thus, contrary to the assumptions of the χ_4/χ_5 model, R1 does not appear to be a self-contained unit, which immobilizes its first two dihedrals through a disulfide-backbone interaction and restricts rotations about its last two dihedrals through steric hindrance of the disulfide with the ring. [27, 44] The flexibility of the R1 side chain suggests that the coupling between the nitroxide and the protein backbone fluctuations is weaker than previously believed. The match between the calculated and the experimental spectra at three different field strengths, provide strong support for the relevance of the MD simulations and the Markov

Table 5.10: Populations of the first four torsion angles determined from the most probable 15 states (populations larger than 1.5%) of the 31-state Markov model of 82R1, built by mixing m and p in a 1-to-9 ratio. The dihedral values observed in the crystal structure are in bold.

χ_1	$-\mathbf{60}^\circ$ (64%)				60°	180°
χ_2	$-\mathbf{60}^\circ$ (36%)		90°	180°	(15%)	(15%)
χ_3	$\mathbf{90}^\circ$ (30%)	-90°	(2%)	(26%)		
χ_4	$\approx \mathbf{90}^\circ$	rest	(6%)			
	(18%)	(12%)				

chain analysis reported in this paper. The changes in the calculated spectra upon artificially removing the local backbone motions, demonstrate that X-band spectra are marginally influenced by backbone fluctuations, and clearly illustrate the sensitivity of high-field ESR to subtle protein dynamics. Collectively, the results of this study indicate that the rigorous interpretation of ESR spectra has to take into account the molecular nature of the spin label and its environment.

5.3 Methods

5.3.1 MD simulation details

The MD simulations were performed with the program CHARMM, using the CHARMM22 protein force field [87] with CMAP correction. [88] The electrostatics was treated with particle mesh Ewald summation. The parameters that were not available in the existing force field were optimized targeting the electrostatic and

energetic properties of the spin label determined from *ab initio* calculations, as described in Ch. 3. The simulated system consisted of a spin labeled T4L, together with 7305 TIP3P water molecules, and 11 sodium and 19 chloride counter ions. Two different sets of simulations were performed at $T = 297$ K and $p = 1$ atm. In one of the sets, 18 trajectories were simulated for 32.3 ns; in the other, 54 trajectories were simulated for 12.7 ns. The first nanosecond was excluded from the analysis. In the first set, T4L was labeled at sites 44, 72, 109, and 119; in the second, at sites 40, 69, 82, and 131 (Fig. 5.1).

5.3.2 Markov chain analysis

The method to best map the MD trajectories to a Markov chain model of the R1 dynamics was discussed in Ch. 4. The values of the five R1 dihedrals were used to infer the states of the (hidden) Markov model, allowing a transition matrix of the state-to-state jump probabilities to be estimated from the MD trajectories. Here we only mention that because of the relatively limited duration of each MD trajectory, one-way transitions were observed for some states (see Table 5.1 for an example). Such states appeared as sources or sinks in the Markov analysis. For the former, the equilibrium probability implied by the estimated transition probability matrix is zero, as if R1 can never return to these states. Entirely discarding such transiently populated states might not be necessarily a bad approximation. Handling the sinks is more problematic. These are the states that the spin label gets into but never leaves during the simulated time window. In the presence of such states the equilibrium probability becomes zero for every state except the sink. In either case, we decided to introduce one artificial transition that leaves the sink to the state that jumped to it, or enters the source from the state that it

exited to. Only some states with $\chi_1 \approx 60^\circ$ acted as a source for 72R1, 131R1 and 82R1, including state #4 in Table 5.8. This value of χ_1 is known to be unfavorable for S_γ when R1 is on α-helices, similarly to cysteine residues, 5% of which have been observed to adapt this conformation in crystal structures. [84] There were no sinks for 131R1 and 82R1. State A in Table 5.3 was a sink for 72R1.

5.3.3 Spectral simulation

ESR spectra were simulated in the time domain with the integrators developed in Ch. 2, using the procedure described in Ch. 4. Trajectories of the instantaneous orientation of the nitroxide-fixed coordinate system N, with respect to the lab-fixed system of axes L, were simulated according to the following motional model:

$$\mathtt{L} \xrightarrow{\text{rot. diff.}} \mathtt{M} \xrightarrow[\text{chain}]{\text{Markov}} \mathtt{N}. \tag{5.1}$$

The molecular frame M, rigidly attached to the T4L molecule, was modeled to undergo global tumbling with rotational diffusion coefficient $D = 18 \times 10^6$ s^{-1}, which is based on the estimate of a multifrequency ESR study and SRLS fit. [81] The MD trajectories provide detailed representation of the dynamics of N with respect to M. The Markov models constructed from the MD trajectories, on the other hand, offer a coarse-grained version of the dynamics of R1 with respect to T4L, but allow us to simulate as many and as long trajectories as required for the convergence of the spectra.

Average magnetic tensors were calulated for each of the Markovian states using the MD trajectories, as described in Chs. 2 and 4. This required the definition of a molecular frame M, so that the detailed dynamics in the MD trajectories were partitioned according to the model (5.1). The averaging was only over the

motion of the nitroxide with respect to `M`, accounted for by the Markov chain model. To remove the global tumbling of T4L from the MD trajectories, the MD snapshots were superimposed such that the deviation of the root-mean-square distance (RMSD) of all the protein backbone atoms was minimized. This is the intuitively most satisfying definition of a coordinate system attached to the protein. With this choice of `M`, all the dynamics with respect to the global protein-fixed frame, including the local backbone motions, contribute to the averaging of the magnetic tensors. To explicitly study the effect of the local backbone fluctuations on the multifrequency ESR spectra this global definition of `M` was replaced with a local one. A coordinate system attached to the helical segment centered at the spin-labeled position i, was defined by superimposing the MD snapshots such that only the RMSD of the backbone atoms of the residues from $i-4$ to $i+4$ was minimized. In this way, the local motion of the helix with respect to the global protein frame was artificially eliminated. The so-defined, helix-fixed coordinate system was allowed to tumble in solution with the same diffusion coefficient as used for the tumbling of T4L.

CHAPTER 6

OUTLOOK TO THE FUTURE

The effort to utilize all-atom MD simulations to understand the molecular origins of the ESR line shape aims to provide insight into the connection between the protein/spin label dynamics and the experimental multifrequency spectra. In the previous chapters, I have summarized the extent to which my Ph.D. work has contributed to the progress in that direction. Nonetheless, it only scratches the surface of the broader challenge to utilize MD simulations in the interpretation of ESR spectra. Many problems remain to be addressed, and many more to be formulated. In the next paragraphs, I point to some of the immediate extensions of my work.

The quantum integrator developed in Ch. 2 was specifically tailored to the simulation of the free induction decay of the transverse magnetization, in the presence of a strong constant magentic field. This justified the high-field approximation and limited attention to the $\rho^{-+}(t)$ part of the density matrix only. As a result, it was possible to have a fast and accurate numerical integrator of the quantal dynamics of the spins. To extend the time-domain simulation of ESR spectra to T_1 relaxation processes and to pulsed ESR, it is necessary to propagate the full density matrix. How to achieve the most efficient and accurate numerical propagation of $\rho(t)$ remains to be clarified.

Another complication that is of tremendous interest in the study of biological systems, is the dipolar coupling between two spin labels on the same macro-

molecule. In this case, the relevant spin Hamiltonian becomes [6, 60]

$$\begin{aligned}\hat{H}(t) = \gamma_{\mathrm{e}} \sum_{i=1,2} \Big(\boldsymbol{B} \cdot \mathsf{G}^{(i)}(t) \cdot \hat{\boldsymbol{S}}^{(i)} + \hat{\boldsymbol{I}}^{(i)} \cdot \mathsf{A}^{(i)}(t) \cdot \hat{\boldsymbol{S}}^{(i)} \Big) \\ \gamma_{\mathrm{e}} \Big(-2J \hat{\boldsymbol{S}}^{(1)} \cdot \hat{\boldsymbol{S}}^{(2)} + \hat{\boldsymbol{S}}^{(1)} \cdot \mathsf{D}(t) \cdot \hat{\boldsymbol{S}}^{(2)} \Big),\end{aligned} \tag{6.1}$$

where $\hat{\boldsymbol{S}}^{(1)}$ and $\hat{\boldsymbol{S}}^{(2)}$ are the spin operators of the electrons, $\hat{\boldsymbol{I}}^{(1)}$ and $\hat{\boldsymbol{I}}^{(2)}$ are the spin operators of the ^{14}N nuclei on the two spin labels and $\mathsf{G}^{(i)}$ and $\mathsf{A}^{(i)}$ are their magnetic tensors. The J coupling is due to the direct overlap of the electronic orbitals, and D is the dipolar coupling tensor. The components of the latter, with respect to the laboratory system of axes, depend on the instantaneous value of the vector $\boldsymbol{r}(t)$ pointing from one of the unpaired electrons to the other, and are defined as

$$D_{ij}(t) = \frac{1}{2} \frac{\mu_0}{4\pi} \hbar \gamma_{\mathrm{e}} \frac{1}{r^3(t)} \left(\delta_{ij} - \frac{3}{r^2(t)} r_i(t) r_j(t) \right). \tag{6.2}$$

As such, D is a symmetric and traceless tensor. The integrator of the quantal spin dynamics needs to be substantially modified to handle the coupling of the two spins. In addition, the (stochastic) model of the classical spin label dynamics has to be augmented, such that it follows not only the orientation of the two nitroxide-fixed frames with respect to the lab-fixed frame, but also the distance between the two electrons.

Potentially, the construction of Markov models of the spin label dynamics from its MD trajectories, presented in Ch. 4, can be further developed and optimized. In Chs. 4 and 5, the number of independent trajectories and their duration was almost arbitrary. The advantages and limitations related to performing hundreds of simulations for several nanoseconds, as opposed to tens of simulations for tens of nanoseconds should be carefully assessed for the approach to gain a wider practical applicability. Building discrete-state stochastic models from continuous MD trajectories is an active area of research, the developments in which are expected

to be directly transferable to the spin label. For example, strategies to identify the important but poorly sampled inter-state connections of the transition probability matrix and to concentrate the later sampling to such regions are being explored [127].

Lastly, for this methodology to be attractive to the experimental community, it is important to be able to vary some of the phenomenological parameters (e.g. the rotational diffusion tensor, the populations of the very slowly exchanging conformations of the spin label, *etc.*) with the intention to determine their values by fitting to experimental spectra, as was done in Ch. 5. Numerically efficient ways of achieving this should be developed more systematically.

APPENDIX A

ROTATIONS

Rotation transformations play a central role in ESR and good understanding of the mathematical aparatus required to describe such transformations is necessary. Basic summary is provided below.

A.1 Active view of rotations

A.1.1 Kinematics of rotations

Let us consider the rotation transformation $\mathscr{R}$, which actively rotates a given vector $\boldsymbol{V}$ to the vector $\boldsymbol{V}'$. This is written as

$$\boldsymbol{V}' = \mathscr{R}\boldsymbol{V}. \tag{A.1}$$

It is convenient to represent the arbitrary abstract vector $\boldsymbol{V}$ in terms of its components in a chosen reference system, defined by the orthonormal triad of right-handed unit vectors $\{\underline{\boldsymbol{e}}_{(1)}, \underline{\boldsymbol{e}}_{(2)}, \underline{\boldsymbol{e}}_{(3)}\}$.[1] In passing, note that the identity operator $\mathscr{E}$ can be expressed in terms of the basis vectors in the form

$$\mathscr{E} = \sum_i \underline{\boldsymbol{e}}_{(i)}\underline{\boldsymbol{e}}_{(i)}, \tag{A.2}$$

referred to as "the resolution of identity" [64]. For a specified choice of the basis vectors, the components V_i determine the vector $\boldsymbol{V}$ uniquely and vice versa:

$$\boldsymbol{V} = \sum_i V_i \underline{\boldsymbol{e}}_{(i)} \qquad \text{and} \qquad V_i = \boldsymbol{V} \cdot \underline{\boldsymbol{e}}_{(i)}. \tag{A.3}$$

[1] The basis vectors obey the orthonormality condition $\underline{\boldsymbol{e}}_{(i)} \cdot \underline{\boldsymbol{e}}_{(j)} = \delta_{ij}$, and form a right-handed coordinate system, $\underline{\boldsymbol{e}}_{(i)} \times \underline{\boldsymbol{e}}_{(j)} = \underline{\boldsymbol{e}}_{(k)}$ for i, j, k cyclic.

Following [64], the collection of the components written as a column vector will be denoted by $[V]$. In the active view of rotations, the operator $\mathscr{R}$ rotates the vectors $\boldsymbol{V}$ of the configuration space but leaves unaffected the basis vectors. The representation of $\boldsymbol{V}$ and $\boldsymbol{V}'$ in terms of their components with respect to $\underline{\boldsymbol{e}}_{(i)}$ induces a representation of the rotation operator $\mathscr{R}$ in terms of its components

$$R_{ij} = \underline{\boldsymbol{e}}_{(i)} \cdot \mathscr{R}\underline{\boldsymbol{e}}_{(j)}. \tag{A.4}$$

The collection of components R_{ij} will be written as the matrix R.[2] This last expression, together with Eq. (A.2), immediately leads to

$$\sum_i \underline{\boldsymbol{e}}_{(i)} R_{ij} = \mathscr{R}\underline{\boldsymbol{e}}_{(j)} = \underline{\boldsymbol{e}}'_{(j)}, \tag{A.5}$$

which shows how the rotated basis vectors are related to the original basis vectors. Since in the active view of rotations the basis vectors are not affected by the transformation $\mathscr{R}$, Eq. (A.5) will not be of any use until we start viewing the rotations passively.

Using the definitions of the vector and operator components, Eqs. (A.3) and (A.4), respectively, into the abstract rule of vector rotation, Eq. (A.1), one straightforwardly obtains its representation

$$V'_i = \sum_j R_{ij} V_j \qquad \text{or} \qquad [V'] = \mathsf{R}[V], \tag{A.6}$$

where the second expression is a restatement of the first using matrix notation.[3] Obsereve that the active transformation of the vector components, Eq. (A.6), is different from the transformation of the basis vectors, Eq. (A.5). We now turn to the transformation of operators under rotation. Given that the operator $\mathscr{O}$

[2]The rotation matrices R form a 3×3 representation of the rotation transformations $\mathscr{R}$. Such matrices are orthogonal, $\mathsf{R}^{-1} = \mathsf{R}^{\top}$, and have unit determinant, $\det \mathsf{R} = +1$. They constitute the three dimensional special orthogonal group SO(3) [9].

[3]Here V'_i are the componets of $\boldsymbol{V}'$, such that $\boldsymbol{V}' = \sum_i V'_i \underline{\boldsymbol{e}}_{(i)}$.

produces the vector $\boldsymbol{W}$ after acting on the vector $\boldsymbol{V}$, i.e. $\boldsymbol{W} = \mathscr{O}\boldsymbol{V}$, we would like to find the operator $\mathscr{O}'$ such that $\boldsymbol{W}' = \mathscr{O}'\boldsymbol{V}'$, for $\boldsymbol{W}'$ and $\boldsymbol{V}'$ as defined in Eq. (A.1). Standard manipulation of the expressions leads to the result

$$\mathscr{O}' = \mathscr{R}\mathscr{O}\mathscr{R}^{-1}, \tag{A.7}$$

for the transformation of operators under rotation. Again, this can be written in terms of the components of the operators in a given coordinate frame, or in terms of the matrix representation of the operators as

$$O'_{ij} = \sum_{kl} R_{ik} O_{kl} R^{\top}_{lj} \qquad \text{or} \qquad \mathsf{O}' = \mathsf{R}\mathsf{O}\mathsf{R}^{\top}. \tag{A.8}$$

A.1.2 Generators of infinitesimal rotations

Any sequence of rotations of the configuration space can be achieved as a single rotation by some angle ϕ about some unit vector $\underline{\boldsymbol{n}}$, where pPositive ϕ corresponds to counterclockwise rotation about $\underline{\boldsymbol{n}}$. The matrices $\mathsf{R}_{(i)}(\phi) \equiv \mathsf{R}(\phi\underline{\boldsymbol{e}}_{(i)})$, describing rotations by ϕ about the basis vectors $\underline{\boldsymbol{e}}_{(i)}$, are particularly easy to find:

$$\begin{aligned}
\mathsf{R}_{(1)} &= \begin{pmatrix} 1 & 0 & 0 \\ 0 & \cos\phi & -\sin\phi \\ 0 & \sin\phi & \cos\phi \end{pmatrix}, \quad \mathsf{R}_{(2)} = \begin{pmatrix} \cos\phi & 0 & \sin\phi \\ 0 & 1 & 0 \\ -\sin\phi & 0 & \cos\phi \end{pmatrix} \\
\mathsf{R}_{(3)} &= \begin{pmatrix} \cos\phi & -\sin\phi & 0 \\ \sin\phi & \cos\phi & 0 \\ 0 & 0 & 1 \end{pmatrix}.
\end{aligned} \tag{A.9}$$

When the rotation angle is infinitesimal, $\phi \to \delta\phi$, they deviate infinitesimally from the 3×3 identity matrix E:

$$\mathsf{R}_{(i)}(\delta\phi) = \mathsf{E} + \delta\phi \mathsf{J}_{(i)}. \tag{A.10}$$

Here the matrices

$$\mathsf{J}_{(1)} = \begin{pmatrix} 0 & 0 & 0 \\ 0 & 0 & -1 \\ 0 & 1 & 0 \end{pmatrix}, \quad \mathsf{J}_{(2)} = \begin{pmatrix} 0 & 0 & 1 \\ 0 & 0 & 0 \\ -1 & 0 & 0 \end{pmatrix}, \quad \mathsf{J}_{(3)} = \begin{pmatrix} 0 & -1 & 0 \\ 1 & 0 & 0 \\ 0 & 0 & 0 \end{pmatrix} \tag{A.11}$$

are the generators of infinitesimal rotations. Their matrix elements are given by

$$(J_{(i)})_{jk} = -\epsilon_{ijk}, \tag{A.12}$$

where ϵ_{ijk} is the Levi-Civita symbol.

The matrix $\mathsf{R}(\delta\phi\underline{\boldsymbol{n}})$ of infinitesimal rotation about an arbitrary direction $\underline{\boldsymbol{n}}$ is given by [2]

$$\mathsf{R}(\delta\phi\underline{\boldsymbol{n}}) = \mathsf{E} + \delta\phi \sum_i n_i \mathsf{J}_{(i)}, \tag{A.13}$$

where

$$\sum_i n_i \mathsf{J}_{(i)} = \begin{pmatrix} 0 & -n_3 & n_2 \\ n_3 & 0 & -n_1 \\ -n_2 & n_1 & 0 \end{pmatrix} \equiv \mathsf{N}. \tag{A.14}$$

From this, one can find the matrix for a finite rotation about $\underline{\boldsymbol{n}}$ as[4]

$$\mathsf{R}(\phi\underline{\boldsymbol{n}}) = \lim_{N\to\infty} \left(\mathsf{E} + \frac{\phi}{N} \sum_i n_i \mathsf{J}_{(i)} \right)^N = \mathrm{e}^{\phi \sum_i n_i \mathsf{J}_{(i)}} = \mathrm{e}^{\phi \mathsf{N}}. \tag{A.16}$$

In addition, expanding the exponential and using $\mathsf{N}^3 = -\mathsf{N}$, the last result can be written as

$$\mathsf{R}(\phi\underline{\boldsymbol{n}}) = \mathsf{E} + \sin\phi\,\mathsf{N} + (1 - \cos\phi)\mathsf{N}^2. \tag{A.17}$$

Acoording to this expression, when the angle and axis of the rotation are given the rotation matrix can be calculated without performing any matrix exponentiation.

[4]Occasionaly, we will denote the product $\phi\underline{\boldsymbol{n}}$ by the vector $\boldsymbol{\phi}$ which is in the direction of $\underline{\boldsymbol{n}}$ and has a magnitude ϕ. With this notation

$$\mathsf{R}(\phi\underline{\boldsymbol{n}}) = \mathsf{R}(\boldsymbol{\phi}) = \mathrm{e}^{\sum_i \phi_i \mathsf{J}_{(i)}}. \tag{A.15}$$

This property is used in the rotational diffusion integrator developed in Ch. 2. Note that the matrix N can be viewed as a representation of the operator $\mathscr{N}$ acting on vectors $\boldsymbol{V}$. Working with the matrix components of N, easily deduced from Eq. (A.12), we find [64]

$$\mathscr{N}\boldsymbol{V} = \underline{\boldsymbol{n}} \times \boldsymbol{V} \tag{A.18}$$

for an arbitrary vector $\boldsymbol{V}$. Because the generators of infinitesimal rotation are special instances of N for the cases where $\underline{\boldsymbol{n}}$ corresponds to the basis vectors, we immediately deduce that they are representations of the operators $\mathscr{J}_{(i)}$, which act on vectors as follows:

$$\mathscr{J}_{(i)}\boldsymbol{V} = \underline{\boldsymbol{e}}_{(i)} \times \boldsymbol{V}. \tag{A.19}$$

At this point we would like to find the transformation of the generators under rotation. Of course, the general result Eq. (A.7) applies to the operators $\mathscr{J}_{(i)}$ as well. Letting $\mathscr{J}'_{(i)}$ operate on a general vector $\boldsymbol{V}$ and using Eq. (A.19) yields

$$\mathscr{J}'_{(j)}\boldsymbol{V} = \mathscr{R}\,\mathscr{J}_{(j)}\mathscr{R}^{-1}\boldsymbol{V} = \mathscr{R}\left(\underline{\boldsymbol{e}}_{(j)} \times (\mathscr{R}^{-1}\boldsymbol{V})\right). \tag{A.20}$$

Since the cross product is invariant under rotations (not proven here but see [64], p.159, for a proof), we have $\mathscr{R}\left(\underline{\boldsymbol{e}}_{(j)} \times (\mathscr{R}^{-1}\boldsymbol{V})\right) = (\mathscr{R}\underline{\boldsymbol{e}}_{(j)}) \times (\mathscr{R}\mathscr{R}^{-1}\boldsymbol{V})$. Finally, from (A.5) together with (A.19), we deduce

$$\boxed{\mathscr{J}'_{(j)} = \mathscr{R}\,\mathscr{J}_{(j)}\mathscr{R}^{-1} = \sum_i \mathscr{J}_{(i)} R_{ij}.} \tag{A.21}$$

Comparing Eq. (A.21) with Eq. (A.5) we see that the generators of infinitesimal rotation transform like the basis vectors under rotation.

A.1.3 Rotational dynamics

The dynamics of a rigid body can be understood as the superposition of two types of motion: translation of the center of mass and relative rotation about the moving center of mass. The magnetization detected in ESR, assuming the sample is irradiated homogeneously, is insensitive to the translational motion. Therefore, in the following, we only consider the effect of rotational dynamics.

Let the time dependent rotation transformation $\mathscr{R}(t)$ act on the constant vector $\boldsymbol{V}$ to produce a time dependent vector $\boldsymbol{V}(t)$ such that

$$\boldsymbol{V}(t) = \mathscr{R}(t)\boldsymbol{V}, \tag{A.22}$$

for all time t. Differentiating both sides of this equation we obtain

$$\frac{\mathrm{d}}{\mathrm{d}t}\boldsymbol{V}(t) = \frac{\mathrm{d}}{\mathrm{d}t}\mathscr{R}(t)\boldsymbol{V} = \frac{\mathrm{d}\mathscr{R}(t)}{\mathrm{d}t}\mathscr{R}^{\top}(t)\boldsymbol{V}(t) = \mathscr{W}(t)\boldsymbol{V}(t). \tag{A.23}$$

The last equality defines the operator

$$\mathscr{W}(t) \equiv \frac{\mathrm{d}\mathscr{R}(t)}{\mathrm{d}t}\mathscr{R}^{\top}(t). \tag{A.24}$$

Its significance is even more transparent if both sides of Eq. (A.24) are multiplied by $\mathscr{R}(t)$ from the right to obtain

$$\frac{\mathrm{d}}{\mathrm{d}t}\mathscr{R}(t) = \mathscr{W}(t)\mathscr{R}(t), \tag{A.25}$$

which is the equation of motion for the time dependent rotational transformation $\mathscr{R}(t)$. Using the orthogonality of the matrix representation R of $\mathscr{R}$ one can write

$$\frac{\mathrm{d}}{\mathrm{d}t}\mathsf{E} = 0 = \frac{\mathrm{d}\mathsf{R}(t)}{\mathrm{d}t}\mathsf{R}^{\top}(t) + \mathsf{R}(t)\frac{\mathrm{d}\mathsf{R}^{\top}(t)}{\mathrm{d}t} = \mathsf{W}(t) + \mathsf{W}^{\top}(t), \tag{A.26}$$

and deduce that $\mathsf{W}^{\top}(t) = -\mathsf{W}(t)$, i.e $\mathsf{W}(t)$ is anti-symmetric. To determine the matrix representation of $\mathsf{W}(t)$ we refer to Eq. (A.15) and the convention discussed

in the footnote. For a time-dependent rotation both the axis and the angle of rotation, and thus the vector $\boldsymbol{\phi}$, become functions of time. Therefore, we find that

$$\mathsf{W}(t) = \sum_i \frac{\mathrm{d}\phi_i(t)}{\mathrm{d}t} \mathsf{J}_{(i)} \equiv \sum_i \omega_i(t) \mathsf{J}_{(i)}. \tag{A.27}$$

Here, we have defined the instantaneous angular velocity vector $\boldsymbol{\omega}(t)$ of the time dependent rotation. Since, as we saw above, the action of the generators of rotation on a vector is equivalent to taking a cross product with the unit vectors, one can write

$$\mathscr{W}(t)\boldsymbol{V} = \boldsymbol{\omega}(t) \times \boldsymbol{V} \tag{A.28}$$

for the action of the operator $\mathscr{W}(t)$.

A.2 Passive rotations

The rotations considered until now were viewed as active transformations of the configuration space. In other words, they rotated the vectors, leaving fixed the coordinate system $\{\underline{\boldsymbol{e}}_{(1)}, \underline{\boldsymbol{e}}_{(2)}, \underline{\boldsymbol{e}}_{(3)}\}$ with respect to which the components of the vectors were referred to. In our case the passive interpretation of rotations, to which we turn now, is more approprite. In this view, the vectors of the configuration space are fixed but their coordinates are referred to two different coordinate axes, $\{\underline{\boldsymbol{e}}_{(1)}, \underline{\boldsymbol{e}}_{(2)}, \underline{\boldsymbol{e}}_{(3)}\}$ and $\{\underline{\boldsymbol{e}}'_{(1)}, \underline{\boldsymbol{e}}'_{(2)}, \underline{\boldsymbol{e}}'_{(3)}\}$, where the basis vector $\underline{\boldsymbol{e}}'_{(j)}$ is obtained by the active rotation of the basis vector $\underline{\boldsymbol{e}}_{(j)}$ by $\mathscr{R}$ (Eq. (A.5)). An arbitrary vector $\boldsymbol{V}$ can thus be expressed in terms of two different sets of componens, one with respect to the original coordinate system and the other with respect to the rotated coordinate system:

$$\boldsymbol{V} = \sum_i V_i \underline{\boldsymbol{e}}_{(i)} = \sum_j V_{j'} \underline{\boldsymbol{e}}'_{(j)}. \tag{A.29}$$

The components in the two systems are respectively

$$V_i = \underline{\boldsymbol{e}}_{(i)} \cdot \boldsymbol{V} \qquad \text{and} \qquad V_{j'} = \underline{\boldsymbol{e}}'_{(j)} \cdot \boldsymbol{V}. \tag{A.30}$$

Starting from the second of these expressions, and using Eq. (A.5), we can determine the relation between the two sets of components:

$$V_{j'} = \underline{\boldsymbol{e}}'_{(j)} \cdot \boldsymbol{V} = \left(\sum_i \underline{\boldsymbol{e}}_{(i)} R_{ij} \right) \cdot \boldsymbol{V} = \sum_i V_i R_{ij}. \tag{A.31}$$

The result can be written either in component or in matrix form,

$$V_{j'} = \sum_i V_i R_{ij} \qquad \text{or} \qquad [V\prime] = \mathsf{R}^\top [V]. \tag{A.32}$$

This passive transformation rule should be compared with the active transformation (Eq. (A.6)).

Similarly, one can find the relation between the components $O_{i'j'}$ and O_{kl} of a constant operator $\mathscr{O}$ with respect to the rotated and initial coordinate systems, [64] p.193. The result, written in component and in matrix form, is

$$O_{i'j'} = \sum_{kl} R^\top_{ik} O_{kl} R_{lj} \qquad \text{and} \qquad \mathsf{O}\prime = \mathsf{R}^\top \mathsf{O} \mathsf{R}. \tag{A.33}$$

Using it one calculates

$$\mathsf{W}\prime = \mathsf{R}^\top \mathsf{W} \mathsf{R} = \sum_i \omega_i \mathsf{R}^\top \mathsf{J}_{(i)} \mathsf{R} = \sum_{ij} \omega_i R_{ij} \mathsf{J}_{(j)} = \sum_j \omega_{j'}(t) \mathsf{J}_{(j)}, \tag{A.34}$$

for the angular velocity. Here, the second equality follows from Eq. (A.27), the third from Eq. (A.21), after the appropriate replacement of R with $\mathsf{R}^\top$, and the fourth from Eq. (A.32). With this, we can write the equation of motion of $\mathsf{R}(t)$ using the angular velocity components either with respect to the stationary or the moving coordinate system:

$$\frac{\mathrm{d}}{\mathrm{d}t}\mathsf{R}(t) = \mathsf{W}(t)\mathsf{R}(t) \qquad \text{or} \qquad \frac{\mathrm{d}}{\mathrm{d}t}\mathsf{R}(t) = \mathsf{R}(t)\mathsf{W}\prime(t). \tag{A.35}$$

The latter equality follows from introducing $\mathsf{R}\mathsf{R}^\top$ on the left side of W in the first. When numerically propagating $\mathsf{R}(t)$ over a time step Δt, these equations suggest the integration schemes

$$\mathsf{R}(t+\Delta t) = \mathrm{e}^{\Delta t \mathsf{W}(t)}\mathsf{R}(t) \qquad \text{or} \qquad \mathsf{R}(t+\Delta t) = \mathsf{R}(t)\mathrm{e}^{\Delta t \mathsf{W}\prime(t)}. \tag{A.36}$$

A.3 Describing rotations with complex matrices

A.3.1 Quaternions

Another more convenient way of parameterizing rotations is to use quaterions. These can be introduced exploiting the relation between the special orthogonal matrices in three dimensions, forming the group SO(3), and the special unitary matrices in two complex dimensions, with the corresponding group SU(2). Using the three Pauli matrices

$$\sigma_{(1)} = \begin{pmatrix} 0 & 1 \\ 1 & 0 \end{pmatrix}, \qquad \sigma_{(2)} = \begin{pmatrix} 0 & -\mathrm{i} \\ \mathrm{i} & 0 \end{pmatrix}, \qquad \sigma_{(3)} = \begin{pmatrix} 1 & 0 \\ 0 & -1 \end{pmatrix} \tag{A.37}$$

we associate the 2×2 complex matrix

$$\mathcal{V} \equiv \sum_i V_i \sigma_{(i)} = \begin{pmatrix} V_3 & V_1 - \mathrm{i}V_2 \\ V_1 + \mathrm{i}V_2 & -V_3 \end{pmatrix} \tag{A.38}$$

with the vector $\boldsymbol{V}$. The components of the vector can be calculated from the matrix $\mathcal{V}$ as

$$V_i = \frac{1}{2}\mathrm{Tr}\left\{\sigma_{(i)}\mathcal{V}\right\}. \tag{A.39}$$

For real $\boldsymbol{V}$ the matrix $\mathcal{V}$ is Hermitian and traceless. These properties should be preserved under rotation.

Since in this case a vector is represented with a matrix, it is natural to seek a rotation transformation in the form of a similarity transformation. In other words, we would like to have

$$\mathcal{V}' = \mathcal{Q}\mathcal{V}\mathcal{Q}^{-1}, \tag{A.40}$$

where $\mathcal{V}'$ is the matrix corresponding to the rotated vector $\boldsymbol{V}'$. A similarity transformation, preserving the Hermiticity and tracelessness of $\mathcal{V}$, would be achieved by a general unitary matrix with unit determinant of the form

$$\mathcal{Q} = \begin{pmatrix} A & B \\ -B^* & A^* \end{pmatrix} = \begin{pmatrix} q_0 - iq_3 & -q_2 - iq_1 \\ q_2 - iq_1 & q_0 + iq_3 \end{pmatrix} = q_0\mathcal{E} - \mathrm{i}\sum_i q_i\sigma_{(i)}, \tag{A.41}$$

with the constraint

$$AA^* + BB^* = q_0^2 + q_1^2 + q_2^2 + q_3^2 = 1. \tag{A.42}$$

Here the matrix $\mathcal{E}$ is the identity 2×2 matrix. At his point the real numbers q_i do not have any significance beyond the fact that they correspond to the real and imaginary parts of A and B in the way specified in Eq. (A.41). As a result of the identification (A.40), using the unitarity of $\mathcal{Q}$, one finds

$$\begin{aligned} V_i' &= \frac{1}{2}\mathrm{Tr}\left\{\sigma_{(i)}\mathcal{V}'\right\} = \frac{1}{2}\mathrm{Tr}\left\{\sigma_{(i)}\mathcal{Q}\mathcal{V}\mathcal{Q}^\dagger\right\} \\ &= \sum_j \frac{1}{2}\mathrm{Tr}\left\{\sigma_{(i)}\mathcal{Q}\sigma_{(j)}\mathcal{Q}^\dagger\right\} V_j, \end{aligned} \tag{A.43}$$

which, after comparison with Eq. (A.6), leads to

$$R_{ij} = \frac{1}{2}\mathrm{Tr}\left\{\sigma_i\mathcal{Q}\sigma_j\mathcal{Q}^\dagger\right\}. \tag{A.44}$$

Thus, associated with each 2×2 matrix $\mathcal{Q}$ there is a 3×3 matrix $\mathsf{R}(\mathcal{Q})$ which transforms $\boldsymbol{V}$ into $\boldsymbol{V}'$. Note that the same matrix R corresponds to both $\mathcal{Q}$ and $-\mathcal{Q}$.

Substituting the form of $\mathcal{Q}$ from Eq. (A.41) into Eq. (A.44) allows us to express the matrix elements of R in terms of the four real numbers q_i:

$$\mathsf{R} = \begin{pmatrix} q_0^2 + q_1^2 - q_2^2 - q_3^2 & 2q_1q_2 - 2q_0q_3 & 2q_1q_3 + 2q_0q_2 \\ 2q_1q_2 + 2q_0q_3 & q_0^2 - q_1^2 + q_2^2 - q_3^2 & 2q_2q_3 - 2q_0q_1 \\ 2q_1q_3 - 2q_0q_2 & 2q_2q_3 + 2q_0q_1 & q_0^2 - q_1^2 - q_2^2 + q_3^2 \end{pmatrix}. \tag{A.45}$$

The numbers q_i, which satisfy the normalization constraint, Eq. (A.42), are the components of the quaternion $\mathfrak{q} = (q_0, q_1, q_2, q_3) \equiv (q_0, \boldsymbol{q})$ corresponding to the rotation $\mathscr{R}$. The inverse problem of calculating the components of the quaternion from a given rotation matrix is solved using the combinations of the diagonal terms

$$1 + R_{11} + R_{22} + R_{33} = 4q_0^2 \qquad 1 + R_{11} - R_{22} - R_{33} = 4q_1^2$$
$$1 - R_{11} + R_{22} - R_{33} = 4q_2^2 \qquad 1 - R_{11} - R_{22} + R_{33} = 4q_3^2$$

together with the differences and sums

$$R_{32} - R_{23} = 4q_0q_1 \qquad R_{13} - R_{31} = 4q_0q_2 \qquad R_{21} - R_{12} = 4q_0q_3$$
$$R_{21} + R_{12} = 4q_1q_2 \qquad R_{32} + R_{23} = 4q_2q_3 \qquad R_{13} + R_{31} = 4q_3q_1$$

of the off-diagonal terms of R. For higher numerical accuracy the largest of the diagonal combinations can be identified and used to calculate the respective quaternion component q_i. Once this component is known the remaining three components can be evaluated using three of the relevant off-diagonal combinations.

A.3.2 Generators and dynamics

Now let us look at the special cases when only q_0 and one of the q_is are different from zero. The rotation matrices corresponding to the matrices $\mathcal{Q}_{(i)} = q_0\mathcal{E} - \mathrm{i}q_i\sigma_{(i)}$

are easy to calculate using Eq. (A.45). Remembering the normalization condition, we find

$$\mathsf{R}_{(1)} = \begin{pmatrix} 1 & 0 & 0 \\ 0 & q_0^2 - q_1^2 & -2q_0q_1 \\ 0 & 2q_0q_1 & q_0^2 - q_1^2 \end{pmatrix}, \quad \mathsf{R}_{(2)} = \begin{pmatrix} q_0^2 - q_2^2 & 0 & 2q_0q_2 \\ 0 & 1 & 0 \\ -2q_0q_2 & 0 & q_0^2 - q_2^2 \end{pmatrix}$$
$$\mathsf{R}_{(3)} = \begin{pmatrix} q_0^2 - q_3^2 & -2q_0q_3 & 0 \\ 2q_0q_3 & q_0^2 - q_3^2 & 0 \\ 0 & 0 & 1 \end{pmatrix}. \tag{A.46}$$

These are strikingly similar to the matrices (A.9), which is why we have given them the same name. The correspondence is exact if $q_0 = \cos(\phi/2)$ and $q_i = \sin(\phi/2)$, for $i = 1, 2, 3$. From this it becomes clear that the parametrization of a rotation in terms of quaterions is intimately related to the parametrization in terms of the axis and angle of rotation. Thus one has

$$\big(q_0, \boldsymbol{q}\big) = \big(\cos(\phi/2), \underline{\boldsymbol{n}}\sin(\phi/2)\big), \tag{A.47}$$

from which it follows that

$$\begin{aligned} \mathcal{Q}(\boldsymbol{\phi}) = \mathcal{Q}(\phi\underline{\boldsymbol{n}}) &= \cos(\phi/2)\mathcal{E} - \mathrm{i}\sin(\phi/2)\sum_i n_i\sigma_{(i)} \\ &= \mathrm{e}^{-\mathrm{i}\frac{1}{2}\phi\sum_i n_i\sigma_{(i)}} = \mathrm{e}^{-\mathrm{i}\frac{1}{2}\sum_i \phi_i\sigma_{(i)}}. \end{aligned} \tag{A.48}$$

Similarly to the real case, one can use the matrices

$$\mathcal{Q}_{(i)}(\phi) \equiv \mathcal{Q}(\phi\underline{\boldsymbol{e}}_{(i)}) = \cos(\phi/2)\mathcal{E} - \mathrm{i}\sin(\phi/2)\sigma_{(i)} \tag{A.49}$$

in the limit $\phi \to \delta\phi$ to identify the generators of infinitesimal rotation as

$$\mathcal{J}_{(i)} = -\mathrm{i}\frac{1}{2}\sigma_{(i)}. \tag{A.50}$$

Again, to address the issue of dynamics, we differentiate both sides of

$$\mathcal{V}(t) = \mathcal{Q}(t)\mathcal{V}\mathcal{Q}^\dagger(t) \tag{A.51}$$

to obtain

$$\frac{\mathrm{d}}{\mathrm{d}t}\mathcal{V}(t) = \frac{\mathrm{d}\mathcal{Q}(t)}{\mathrm{d}t}\mathcal{V}\mathcal{Q}^{\dagger}(t) + \mathcal{Q}(t)\mathcal{V}\frac{\mathrm{d}\mathcal{Q}^{\dagger}(t)}{\mathrm{d}t} = [\mathcal{W}(t), \mathcal{V}(t)]. \tag{A.52}$$

Here, as before, we have defined

$$\mathcal{W}(t) \equiv \frac{\mathrm{d}\mathcal{Q}(t)}{\mathrm{d}t}\mathcal{Q}^{\dagger}(t) = -\mathrm{i}\frac{1}{2}\sum_i \omega_i(t)\sigma_{(i)}, \tag{A.53}$$

and used the fact that it is anti-unitary, $\mathcal{W}^{\dagger}(t) = -\mathcal{W}(t)$, to write the commutator in the last expression. The definition of $\mathcal{W}(t)$ provides the equation of motion for $\mathcal{Q}(t)$:

$$\frac{\mathrm{d}}{\mathrm{d}t}\mathcal{Q}(t) = \mathcal{W}(t)\mathcal{Q}(t) \qquad \text{or} \qquad \frac{\mathrm{d}}{\mathrm{d}t}\mathcal{Q}(t) = \mathcal{Q}(t)\mathcal{W}_{\prime}(t). \tag{A.54}$$

These imply

$$\mathcal{Q}(t+\Delta t) = \mathrm{e}^{\Delta t\mathcal{W}(t)}\mathcal{Q}(t) \qquad \text{or} \qquad \mathcal{Q}(t+\Delta t) = \mathcal{Q}(t)\mathrm{e}^{\Delta t\mathcal{W}_{\prime}(t)} \tag{A.55}$$

for the numerical propagation. This form, used in the integrator of Ch. 2, is very attractive because the exponentiation of $\mathcal{W}$ leads to a unitary matrix and thus preserves the normalization of the quaternion (Eq. (A.42)).

The transformation achived by R_A followed by R_B is $R = R_B R_A$. Similarly, the corresponding quaternioins are related via $\mathfrak{q} = \mathfrak{q}_B\mathfrak{q}_A$. In component form this reads

$$\begin{aligned}
q_0 &= q_0^B q_0^A - q_1^B q_1^A - q_2^B q_2^A - q_3^B q_3^A \\
q_1 &= q_0^B q_1^A + q_1^B q_0^A + q_2^B q_3^A - q_3^B q_2^A \\
q_2 &= q_0^B q_2^A - q_1^B q_3^A + q_2^B q_0^A + q_3^B q_1^A \\
q_3 &= q_0^B q_3^A + q_1^B q_2^A - q_2^B q_1^A + q_3^B q_0^A .
\end{aligned}$$

Such consecutive rotations are at the basis of our calculation of ESR spectra from motional models like (4.58) or (4.59).

BIBLIOGRAPHY

[1] A. Abragam. *Principles of Nuclear Magnetism.* Oxford University Press, 1961.

[2] Simon L. Altmann. *Rotations, Quaternions and Double Groups.* Dover Publications, Inc., 2005.

[3] Victor M. Anisimov, Guillaume Lamoureux, Igor V. Vorobyov, Niu Huang, Benoit Roux, and Alexander D. MacKerell. Determination of electrostatic parameters for a polarizable force field based on the classical drude oscillator. *Journal of Chemical Theory and Computation*, 1:153–168, 2005.

[4] Jeff P. Barnes, Zhichun Liang, Hassane S. Mchaourab, Jack H. Freed, and Wayne L. Hubbell. A multifrequency electron spin resonance study of T4 Lysozyme dynamics. *Biophysical Journal*, 76:23298–3306, 1999.

[5] V. Barone, A. Bencini, M. Cossi, A. D. Matteo, M. Mattesini, and F. Totti. Assessment of a combined qm/mm approach for the study of large nitroxide systems in vacuo and in condensed phases. *Journal of the American Chemical Society*, 120:7069–7078, 1998.

[6] Vincenzo Barone and Antonino Polimeno. Toward an integrated computational approach to cw-ESR spectra of free radicals. *Physical Chemistry Chemical Physics*, 8:4609–4629, 2006.

[7] Christian Beier and Heinz-Jurgen Steinhoff. A structure-based simulation approach for electron paramagnetic resonance spectra using molecular and stochastic dynamics simulations. *Biophysical Journal*, 91:2647–2664, 2006.

[8] W. S. Benedict, N. Gailar, and Earle K. Plyler. Rotation-vibration spectra of deuterated water vapor. *Journal of Chemical Physics*, 24:1139–1165, 1956.

[9] L. C. Biedenharn and J. D. Louck. *Angular Momentum in Quantum Physics: Theory and Application.* Addison-Wesley Publishing Company, Inc., 1981.

[10] Jeff A. Bilmes. A gentle tutorial of the em algorithm and its application to parameter estimation for Gaussian mixture and hidden Markov models. Technical report, International Computer Science Institute, Berkeley, April 1998.

[11] Mogens Bladt and Michael Sorensen. Statistical inference for discretely observed Markov jump processes. *Journal of the Royal Statistical Society B*, 67:395–410, 2005.

[12] P. Borbat, T.F. Ramlall, J.H. Freed, and D. Eliezer. Inter-helix distances in lysophospholipid micelle-bound α-synuclein from pulsed esr measurements. *Journal of the American Chemical Society*, 128(31):10004–10005, 2006.

[13] P. P. Borbat, A. J. Costa-Filho, K. A. Earle, J. K. Moscicki, and J. H. Freed. Electron spin resonance in studies of membranes and proteins. *Science*, 291:266–269, 2001.

[14] P. P. Borbat and J. H. Freed. Measuring distances by pulsed dipolar ESR spectroscopy: Spin-labeled histidine kinases. *Methods in Enzymology*, 423:52–116, 2007.

[15] Peter P. Borbat, J. H. Davis, S. E. Butcher, and Jack H. Freed. Measurement of large distances in biomolecules using double-quantum-filtered refocused electron-spin-echoes. *Journal of the American Chemical Society*, 126:7746–7747, 2004.

[16] Peter P. Borbat, Kavitha Surendhran, Marco Bortolus, Ping Zou, Jack H. Freed, and Hassane S. Mchaourab. Conformational motion of the ABC transporter MsbA induced by ATP hydrolysis. *PLOS Biology*, 5(10):2211–2219, 2007.

[17] P.P. Borbat, H.S. Mchaourab, and J.H. Freed. Protein structure determination using long-distance constraints from double-quantum coherence esr: Study of t4 lysozyme. *Journal of the American Chemical Society*, 124(19):5304–5314, 2002.

[18] David E. Budil, Sanghyuk Lee, Sunil Saxena, and Jack H. Freed. Nonlinear-least-squares analysis of slow-motion epr spectra in one and two dimensions using a modified Levenberg-Marquardt algorithm. *Journal of Magnetic Resonance A*, 120:155–189, 1996.

[19] David E. Budil, Kenneth L. Sale, Khaled A. Khairy, and Peter G. Fajer. Calculating slow-motional electron paramagnetic resonance spectra from molecular dynamics using a diffusion operator approach. *Journal of Physical Chemistry A*, 110:3703–3713, 2006.

[20] Roberta Cassol, Alberta Ferrarini, and Pier Luigi Nordio. Dynamics of

nitroxide probes linked to flexible chains. *Journal of Physical Chemistry*, 97:2933–2940, 1993.

[21] Roberta Cassol, Ming-Tao Ge, Alberta Ferrarini, and Jack H. Freed. Chain dynamics and the simulaton of electron spin resonance spectra from oriented phospholipid membranes. *Journal of Physical Chemistry B*, 101:8782–8789, 1997.

[22] David Chandler. Statistical machanics of isomerization dynamics in liquids and the transition state approximation. *Journal of Chemical Physics*, 68:2959–2970, 1978.

[23] David Chandler. *Introduction to Modern Statistical Mechanics*. Oxford University Press, 1987.

[24] John D. Chodera, Nina Singhal, Vijay S. Pande, Ken A. Dill, and William C. Swope. Automatic discovery of metastable states for the construction of Markov models of macromolecular conformational dynamics. *Journal of Chemical Physics*, 126:155101, 2007.

[25] W. T. Coffey, Yu. P. Kalmykov, and J. T. Waldron. *The Langevin Equation with Applications to Stochastic Problems in Physics, Chemistry and Electrical Engineering*. World Scientific Publishing, 2nd edition, 2004.

[26] Linda Columbus and Wayne L. Hubbell. A new spin on protein dynamics. *Trends in Biochemical Sciences*, 27:288–295, 2002.

[27] Linda Columbus, Tamas Kalai, Jozsef Jeko, Kalman Hideg, and Wayne L. Hubbell. Molecular motion of spin labeled side chains in α-helices: Analysis by variation of side chain structure. *Biochemistry*, 40:3828–3846, 2001.

[28] Linda Marie Columbus. *Investigating Backbone and Side Chain Dynamics of α-Helices in the Nanosecond Regime with Site-Directed Spin Labeling*. PhD thesis, University of California, Los Angeles, 2001.

[29] Luis G. Cuello, D. Marien Cortes, and Eduardo Perozo. Molecular architecture of the KvAP voltage-dependent K+ channel in a lipid bilayer. *Science*, 306:491–495, 2004.

[30] Peter Deuflhard. From molecular dynamics to conformational dynamics in drug design. Technical report, Konrad-Zuse-Zentrum für Informationstechnik Berlin, April 2002.

[31] Peter Deuflhard, W. Huisinga, A. Fischer, and Christof Schütte. Identification of almost invariant aggregates in reversible nearly uncoupled Markov chains. *Linear Algebra and its Applications*, 315:39–59, 2000.

[32] Peter Deuflhard and Marcus Weber. Robust Perron cluster analysis in conformation dynamics. *Linear Algebra and its Applications*, 398:161–184, 2005.

[33] Jinhui Dong, Yang Guangyong, and Hassane S. Mchaourab. Structural basis of energy transduction in the transport cycle of MsbA. *Science*, 308:1023–1028, 2005.

[34] Weinan E, Di Liu, and Eric Vanden-Eijnden. Analysis of multiscale methods for stochastic differential equations. *Communications on Pure and Applied Mathematics*, 53:1544–1585, 2005.

[35] Keith A. Earle, Boris Dzikovski, Wulf Hofbauer, Jozef K. Moscicki, and Jack H. Freed. High-frequency ESR an ACERT. *Magnetic Resonance in Chemistry*, 43:S256–S266, 2005.

[36] Sidney P. Elmer, Sanghyun Park, and Vijay S. Pande. Foldamer dynamics expressed via Markov state models. i. explicit solvent molecular-dynamics simulations in acetonitrile, chloroform, methanol, and water. *Journal of Chemical Physics*, 123:114902, 2005.

[37] R. R. Ernst, G. Bodenhausen, and A. Wokaun. *Principles of Nuclear Magnetic Resonance in One and Two Dimensions*. Oxford University Press, 1987.

[38] H. Eviatar, Yehudi K. Levine, and D. I. Hoult. The simulation of two-dimensional electron-spin-echo experiments on liquid-crystalline systems using stochastic trajectories of motion motion. *Journal of Magnetic Resonance A*, 117:41–52, 1995.

[39] H. Eviatar, Uulke van der Heide, and Yehudi K. Levine. Computer simulations of the electron spin resonance spectra of steroid and fatty acid nitroxide probes in bilayer systems. *Journal of Chemical Physics*, 102:3135–3145, 1995.

[40] H. Eviatar, E.E. van Faassen, Y.K. Levine, and D.I. Hoult. Time-domain simulation of ESR spectra of nitroxide spin probes. *Chemical Physics*, 181:369–376, 1994.

[41] Gail E. Fanucci and David S. Cafiso. Recent advances and applications of

site-directed spin labeling. *Current Opinion in Structural Biology*, 16:644–653, 2006.

[42] I. I. Fedchenia, P.-O. Westlund, and U. Cegrell. Brownian dynamics simulation of restricted molecular diffusion. the symmetric and deformed cone models. *Molecular Simulation*, 11:373–393, 1993.

[43] Scott E. Feller, Richard W. Pastor, Atipat Rojnuckarin, Stephan Bogusz, and Bernard R. Brooks. Effect of electrostatic force truncation on interfacial and transport properties of water. *Journal of Physical Chemistry*, 100:17011–17020, 1996.

[44] Mark Raymond Fleissner. *X-ray Structures of Nitroxide Side Chains in Proteins: A Basis for Interpreting Distance Measurements and Dynamic Studies by Electron Paramagnetic Resonance*. PhD thesis, University of California, Los Angeles, 2007.

[45] Jack H. Freed. New technologies in electron spin resonance. *Annual Reviews of Physical Chemistry*, 51:655–689, 2000.

[46] Jack H. Freed, G. V. Bruno, and C. F. Polnaszek. Electron spin resonance line shapes and saturation in the slow motional region. *Journal of Physical Chemistry*, 75:3385, 1971.

[47] M. J. Frisch, G. W. Trucks, H. B. Schlegel, G. E. Scuseria, M. A. Robb, J. R. Cheeseman, J. A. Montgomery, Jr., T. Vreven, K. N. Kudin, J. C. Burant, J. M. Millam, S. S. Iyengar, J. Tomasi, V. Barone, B. Mennucci, M. Cossi, G. Scalmani, N. Rega, G. A. Petersson, H. Nakatsuji, M. Hada, M. Ehara, K. Toyota, R. Fukuda, J. Hasegawa, M. Ishida, T. Nakajima, Y. Honda, O. Kitao, H. Nakai, M. Klene, X. Li, J. E. Knox, H. P. Hratchian, J. B. Cross, V. Bakken, C. Adamo, J. Jaramillo, R. Gomperts, R. E. Stratmann, O. Yazyev, A. J. Austin, R. Cammi, C. Pomelli, J. W. Ochterski, P. Y. Ayala, K. Morokuma, G. A. Voth, P. Salvador, J. J. Dannenberg, V. G. Zakrzewski, S. Dapprich, A. D. Daniels, M. C. Strain, O. Farkas, D. K. Malick, A. D. Rabuck, K. Raghavachari, J. B. Foresman, J. V. Ortiz, Q. Cui, A. G. Baboul, S. Clifford, J. Cioslowski, B. B. Stefanov, G. Liu, A. Liashenko, P. Piskorz, I. Komaromi, R. L. Martin, D. J. Fox, T. Keith, M. A. Al-Laham, C. Y. Peng, A. Nanayakkara, M. Challacombe, P. M. W. Gill, B. Johnson, W. Chen, M. W. Wong, C. Gonzalez, and J. A. Pople. Gaussian 03, Revision C.02. Gaussian, Inc., Wallingford, CT, 2004.

[48] David Fritzsche, Volker Mehrmann, Daniel B. Szyld, and Elena Virnik. An SVD approach to identifying meta-stable states of Markov chains. Technical

Report 06-08-04, Department of Mathematics, Temple University, August 2006.

[49] Dror Givon, Raz Kupferman, and Andrew Stuart. Extracting macroscopic dynamics: Model problems and algorithms. *Nonlinearity*, 17:R55–R127, 2004.

[50] Zhefeng Guo. *Correlation of Spin Label Side-Chain Dynamics with Protein Structure: Studies of T4 Lysozyme with Site-Directed Mutagenesis and X-ray Crystallography*. PhD thesis, University of California, Los Angeles, 2003.

[51] Zhefeng Guo, Dulio Cascio, Kalman Hideg, Tamas Kalai, and Wayne L. Hubbell. Structural determination of nitroxide motion in spin-labeled proteins: Tertiary contact and solvent-inaccessible sites in helix G of T4 Lysozyme. *Protein Science*, 16:1069–1086, 2007.

[52] Risken. H. *The Fokker-Planck Equation*. Springer-Verlag, 1984.

[53] P. Hakansson, L. Persson, and Per-Olof Westlund. Itô diffusions on hypersurfaces with application to the Schwarz-P surface and nuclear magnetic resoanance theory. *Journal of Chemical Physics*, 117:8634–8643, 2002.

[54] P. Hakansson, Per-Olof Westlund, E. Lindahl, and O. Edholm. A direct simulation of EPR slow-motion spectra of spin labelled phospholipids in liquid crystalline bilayers based on a molecular dynamics simulation of the lipid dynamics. *Physical Chemistry Chemical Physics*, 3:5311–5319, 2001.

[55] Illia Horenko, Evelyn Dittmer, Alexander Fischer, and Christof Schütte. Automated model reduction for complex systems exhibiting metastability. *Multiscale Modeling and Simulation*, 5(3):802–827, 2006.

[56] Illia Horenko, Evelyn Dittmer, and Christof Schütte. Reduced stochastic models for complex molecular systems. *Computing and Visualization in Science*, 9:89–102, 2006.

[57] Wayne L. Hubbell, David S. Cafiso, and Christian Altenbach. Identifyaing conformational changes with site-directed spin labeling. *Nature Structural Biology*, 7:735–739, 2000.

[58] Wayne L. Hubbell, Adrian Gross, Ralf Langen, and Michael A. Lietzow. Recent advances in site-directed spin labeling of proteins. *Current Opinion in Structural Biology*, 8:649–656, 1998.

[59] William Humphrey, Andrew Dalke, and Klaus Schulten. VMD – Visual Molecular Dynamics. *Journal of Molecular Graphics*, 14:33–38, 1996.

[60] Eric J. Hustedt and Albert H. Beth. Nitroxide spin-spin interactions: Applications to protein structure and dynamics. *Annual Reviews of Biophysics and Biomolecular Structure*, 28:129–153, 1999.

[61] Rikki N. Hvorup, Birke A. Goetz, Martina Niederer, Kaspar Hollenstein, Eduardo Perozo, and Kaspar P. Locher. Asymmetry in the structure of the ABC transporter-binding protein complex BtuCD-BtuF. *Science*, 317:1387–1390, 2007.

[62] Robert B. Israel, Jeffrey S. Rosenthal, and Jason Z. Wei. Finiding generators for Markov chains via empirical transition matrices, with applications to credit ratings. *Mathematical Finance*, 11:245–265, 2001.

[63] Ding Jiao, Michael Barfield, Jaime E. Combarzia, and Victor J. Hruby. Ab initio molecular orbital studies of the rotational barriers and the ^{33}S and ^{13}C chemical shieldings for dimethyl disulfide. *Journal of the American Chemical Society*, 114:3639–3643, 1992.

[64] Oliver Davis Johns. *Analytical Mechanics for Relativity and Quantum Mechanics*. Oxford University Press, 2005.

[65] W. L. Jorgensen, J. Chandrasekhar, J. D. Madura, R. W. Impey, and M. L. Klein. Comparison of simple potential functions for simulating liquid water. *Journal of Chemical Physics*, 79:926–935, 1983.

[66] W. L. Jorgensen, D. S. Maxwell, and J. Tirado-Rives. Development and testing of the OPLS all-atom force field on conformational energetics and properties of organic liquids. *Journal of the American Chemical Society*, 118:11225–11236, 1996.

[67] W. L. Jorgensen and J. Tirado-Rives. The OPLS potential functions for proteins. energy minimization for crystals of cyclic peptides and crambin. *Journal of the American Chemical Society*, 110:1657–1666, 1988.

[68] Wolfram Just, Katrin Gelfert, Nilufer Baba, Anja Riegert, and Holger Kantz. Elimination of fast chaotic degrees of freedom: On the accuracy of the Born approximation. *Journal of Statistical Physics*, 112:277–292, 2003.

[69] Wolfram Just, Holger Kantz, Christian Rodenbeck, and Mario Helm.

Stochastic modeling: Replacing fast degrees of freedom by noise. *Journal of Physics A: Mathematical and General*, 34:3199–3213, 2001.

[70] Y. P. Kalmykov. Rotational brownian motion and nonlinear dielectric relaxation of asymetric top molecules in strong electric fields. *Physical Review E*, 65:021101, 2001.

[71] Wolfram Koch and Max C. Holthausen. *A Chemist's Guide to Density Functional Theory*. Wiley-VCH Verlag GmbH, 2000.

[72] Susanna Kube and Marcus Weber. A coarse graining method for the identification of transition rates between molecular conformations. *Journal of Chemical Physics*, 126:024103, 2007.

[73] Susanna Kube and Marcus Weber. Coarse graining molecular kinetics. Technical report, Konrad-Zuse-Zentrum für Informationstechnik Berlin, June 2007.

[74] Ryogo Kubo. Note on the stochastic theory of resonance absorption. *Journal of the Physical Society of Japan*, 9:935–944, 1954.

[75] Ryogo Kubo. Stochastic theories of randomly modulated systems. *Journal of the Physical Society of Japan, Supplement*, 26:1–5, 1969.

[76] Ryogo Kubo. A stochastic theory of line shape. *Advances in Chemical Physics*, 15:101–127, 1969.

[77] James J. Kuffner. Effective sampling and distance metrics for 3D rigid body path planning. *Proc. IEEE Int'l Conf. on Robotics and Automation (ICRA 2004)*, pages 1–6, 2004.

[78] Ralf Langen, Kyoung Joon Oh, Duilio Cascio, and Wayne L. Hubbell. Crystal structures of spin labeled T4 Lysozyme mutants: Implications for the interpretation of epr spectra in terms of structure. *Biochemistry*, 39:8396–8405, 2000.

[79] Y. K. Levine, N. J. M. Birdsall, Lee A. G., J. C. Metcalfe, P. Partington, and G. C. K Roberts. Calculation of dipolar numclear magnetic relaxation times in molecules with multiple internal rotations. II Theoretical results for anisotropic over-all motion of the molecule, and comparison with ^{13}C relaxation times in n-alkanes and n-alkyl bromides. *Journal of Chemical Physics*, 60:2890–2899, 1974.

[80] Zhichun Liang and Jack H. Freed. An assessment of the applicability of multifrequency ESR to study the complex dynamics of biomolecules. *Journal of Physical Chemistry B*, 103:6384–6396, 1999.

[81] Zhichun Liang, Yan Lou, Jack H. Freed, Linda Columbus, and Wayne L. Hubbell. A multifrequency electron spin resonance study of T4 Lysozyme dynamics using the slowly relaxing local structure model. *Journal of Physical Chemistry B*, 108:17649–17659, 2004.

[82] Michael Lietzow and Wayne L. Hubbell. Motion of spin label side chains in cellular retinol-binding protein: correlation with structure and nearest-neighbor interactions in an antiparallel β-sheet. *Biochemistry*, 43:3137–3151, 2004.

[83] Louis A. Liporace. Maximum likelihood estimation for multivariate observations of Markov sources. *IEEE Trans. Inform. Theory*, IT-28:729–734, 1982.

[84] Simon C. Lovell, J. Michael Word, Jane S. Richardson, and David C. Richardson. The penultimate rotamer library. *Proteins*, 40:389–408, 2000.

[85] R. M. Lynden-Bell and A. J. Stone. Reorientational correlation functions, quaternions and Wigner rotation matrices. *Molecular Simulation*, 3:271–281, 1989.

[86] Ao Ma and Aaron R. Dinner. An automatic method for identifying reaction coordinates in complex systems. *Journal of Physical Chemistry B*, 109:6769–6779, 2005.

[87] A. D. MacKerell, Jr., D. Bashford, M. Bellott, R.L. Dunbrack Jr., J.D. Evanseck, M.J. Field, S. Fischer, J. Gao, H. Guo, S. Ha, D. Joseph-McCarthy, L. Kuchnir, K. Kuczera, F.T.K. Lau, C. Mattos, S. Michnick, T. Ngo, D.T. Nguyen, B. Prodhom, W.E. Reiher, III, B. Roux, M. Schlenkrich, J.C. Smith, R. Stote, J. Straub, M. Watanabe, J. Wiorkiewicz-Kuczera, D. Yin, and M. Karplus. All-atom empirical potential for molecular modeling and dynamics studies of proteins. *Journal of Physical Chemistry B*, 102:3586–3616, 1998.

[88] Alexender D. MacKerell, Jr., Mivhael Feig, and Charles L. Brooks III. Extending the treatment of backbone energetics in protein force fields: Limitations of gas-phase quantum mechanics in reproducing protein conformational distributions in molecular dynamics simulations. *Journal of Computational Chemistry*, 25:1400–1415, 2004.

[89] Harden M. McConnell and Wayne L. Hubbell. Molecular motion in spin-labeled phospholipids and membranes. *Journal of the American Chemical Society*, 93(2):314–326, 1971.

[90] Hassane S. Mchaourab, Tamas Kalai, Kalman Hideg, and Wayne L. Hubbell. Motion of spin-labeled side chains in T4 Lysozyme: Effect of side chain structure. *Biochemistry*, 38:2947–2955, 1999.

[91] Hassane S. Mchaourab, Michael A. Lietzow, Kalman Hideg, and Wayne L. Hubbell. Motion of spin-labeled side chains in T4 Lysozyme. Correlation with protein structure and dynamics. *Biochemistry*, 35:7692–7704, 1996.

[92] Sean A. McKinney, Chirlmin Joo, and Taekjip Ha. Analysis of Single-Molecule FRET Trajectories Using Hidden Markov Modeling. *Biophysical Journal*, 91(5):1941–1951, 2006.

[93] Eike Meerbach, Christof Schütte, Illia Horenko, and Burkhard Schmidt. Metastable conformational structure and dynamics: Peptides between gas phase and aqueous solution. In O. Kühn and L. Wöste, editors, *Analysis and control of ultrafast photoinduced reactions*, volume 87, pages 798–808. Springer, 2007.

[94] Eva Meirovitch, Akbar Nayeem, and Jack H. Freed. Analysis of protein-lipid interactions based on model simulations of electron spin resonance spectra. *Journal of Physical Chemistry*, 88:3454–3465, 1984.

[95] Shaul Mukamel. *Principles of Nonlinear Optical Spectroscopy*. Oxford University Press, 1995.

[96] Krzystof Murzyn, Tomasz Róg, Wojciech Blicharski, Malgorzata Dutka, Janusz Pyka, Sebastian Szytula, and Wojciech Froncisz. Influence of the disulfide bond configuration on the dynamics of the spin label attached to Cytochrome *c*. *Proteins*, 62:1088–1100, 2006.

[97] Frank Noe, Illia Horenko, Christof Schütte, and Jeremy C. Smith. Hierarchical analysis of conformational dynamics in biomolecules: Transition networks of metastable states. *Journal of Chemical Physics*, 126:155102, 2007.

[98] James R. Norris. *Markov Chains*. Cambridge University Press, 1997.

[99] Sang-Youn Park, Peter P. Borbat, Gabriela Gonzalez-Bonet, Jaya Bhatnagar, Abiola M. Pollard, Jack H. Freed, Alexandrine M. Bilwes, and Brian R.

Crane. Reconstruction of the chemotaxis receptor-kinase assembly. *Nature Structural Biology*, 13(5):400–407, 2006.

[100] Sanghyun Park and Vijay S. Pande. Validation of Markov state models using Shannon's entropy. *Journal of Chemical Physics*, 124:054118, 2006.

[101] J. B. Pedersen. Monte Carlo calculation of ESR line shapes in the slow motional region. *Journal of Chemical Physics*, 57:2680–2683, 1972.

[102] Eduardo Perozo, D. Marien Cortes, and Luis G. Cuello. Three-dimensional architecture and gating mechanism of a K^+ channel studied by epr spectroscopy. *Nature Structural Biology*, 5:459–469, 1998.

[103] Eduardo Perozo, D. Marien Cortes, and Luis G. Cuello. Structural rearrangements underlying K^+-channel activation gating. *Science*, 285:73–78, 1999.

[104] Eduardo Perozo, D. Marien Cortes, Pornthep Sompornpisut, Anna Kloda, and Boris Martinac. Open channel structure of MscL and the gating mechanism of mechanosensitive channels. *Nature*, 418:942–948, 2002.

[105] L. Persson, U. Cegrell, Natalia Usova, and Per-Olof Westlund. The mathematical theory of Itô diffusions on hypersurfaces, with application to NMR relaxation problems. *Journal of Mathematical Chemistry*, 31:65–89, 2002.

[106] Antonino Polimeno and Jack H. Freed. A many-body stochastic approach to rotational motions in liquids. *Advances in Chemical Physics*, 83:89–210, 1993.

[107] Antonino Polimeno and Jack H. Freed. Slow motional ESR in complex fluids: The slowly relaxing local structure model of solvent cage effects. *Journal of Physical Chemistry*, 99:10995–11006, 1995.

[108] C. F. Polnaszek, G. V. Bruno, and Jack H. Freed. ESR line shapes in the slow-motional region: Anisotropic liquids. *Journal of Chemical Physics*, 58:3185–3199, 1973.

[109] Oleg L. Polyansky, Per Jensen, and Jonathan Tennyson. A spectroscopically determined potential energy surface for the ground state of $H_2{}^{16}O$: A new level of accuracy. *Journal of Chemical Physics*, 101:7651–7657, 1994.

[110] Alessandro Ponti. Simulation of magnetic resonance static powder lineshapes: A quantitative assessment of spherical codes. *Journal of Magnetic Resonance*, 138:288–297, 1999.

[111] Feng Qin, Anthony Auerbach, and Frederick Sachs. A Direct Optimization Approach to Hidden Markov Modeling for Single Channel Kinetics. *Biophysical Journal*, 79(4):1915–1927, 2000.

[112] Lawrence R. Rabiner. A tutorial on hidden Markov models and selected applications in speech recognition. *Proc. IEEE*, 77:257–286, 1989.

[113] Paul R. Rablen, Jeffrey W. Lockman, and William L. Jorgensen. Ab initio study of hydrogen-bonded complexes of small organic molecules with water. *Journal of Physical Chemistry A*, 102:3782–3797, 1998.

[114] A. G. Redfield. On the theory of relaxation processes. *IBM Journal of Research and Development*, 1:19–31, 1957.

[115] A. G. Redfield. The theory of relaxation processes. *Advances in Magnetic Resonance*, 1:1–32, 1965.

[116] B. H. Robinson, C. Mailer, and G. Drobny. Site-specific dynamics in DNA: Experiments. *Annual Reviews of Biophysics and Biomolecular Structure*, 26:629–658, 1997.

[117] B. H. Robinson, L. J. Slutsky, and F. P. Auteri. Direct simulation of continuous wave electron paramagnetic resonance spectra from Brownian dynamics trajectories. *Journal of Chemical Physics*, 96:2609–2616, 1992.

[118] Kenneth L. Sale, Cecília Sár, Kim A. Sharp, Kálmán Hideg, and Peter G. Fajer. Structural determination of spin label immobilization and orientation: A Monte Carlo minimization approach. *Journal of Magnetic Resonance*, 156:104–112, 2002.

[119] Kenneth Louis Sale. *Molecular Modeling of Nitroxide Spin Labels: Methods Development and Application*. PhD thesis, The Florida State University, 2002.

[120] Martin Saunders and Charles S. Johnson, Jr. Monte Carlo calculation of magnetic resonance spectra for spins in motion. *Journal of Chemical Physics*, 48:534–536, 1968.

[121] M. Schlenkrich, J. Brickmann, A.D. MacKerell, Jr., and M. Karplus. An empirical potential energy function for phospholipids: Criteria for parameter optimization and applications. In *Biological Membranes: A Molecular Perspective from Computation and Experiment*, pages 31–81. Birkhauser, Boston, 1996.

[122] David J. Schneider and Jack H. Freed. Spin relaxation and motional dynamics. *Advances in Chemical Physics*, 73:387–527, 1989.

[123] Christof Schütte, A. Fischer, W. Huisinga, and Peter Deuflhard. A direct approach to conformational dynamics based on hybrid Monte Carlo. *Journal of Computational Physics*, 151:146–168, 1999.

[124] Anthony P. Scott and Leo Radom. Harmonic vibrational frequencies: An evaluation of hartree-fock, mller-plesset, quadratic configuration interaction, density functional theory, and semiempirical scale factors. *Journal of Physical Chemistry*, 100:16502–16513, 1996.

[125] David Shalloway. Macrostates of classical stochastic systems. *Journal of Chemical Physics*, 105:9986–10007, 1996.

[126] Ken Shoemake. Animating rotations with quaternion curves. *Proc. of SIGGRAPH '85*, pages 245–254, 1985.

[127] Nina Singhal and Vijay S. Pande. Error analysis and efficient sampling in Markovian state models for molecular dynamics. *Journal of Chemical Physics*, 123:204909, 2005.

[128] Nina Singhal, Christopher D. Snow, and Vijay S. Pande. Using path sampling to build better Markovian state models: Predicting the folding rate and mechanism of a tryptophan zipper beta hairpin. *Journal of Chemical Physics*, 121:415–425, 2004.

[129] Nina Singhal Hinrichs and Vijay S. Pande. Calculation of the distribution of eigenvalues and eigenvectors in Markovian state models for molecular dynamics. *Journal of Chemical Physics*, 126:244101, 2007.

[130] Charles P. Slichter. *Principles of Magnetic Resonance*. Springer Verlag, 3nd edition, 1990.

[131] Irina Smirnova, Vladimir Kasho, Jun-Yong Choe, Christian Altenbach, Wayne L. Hubbell, and H. Ronald Kaback. Sugar binding induces an out-

ward facing conformation of LacY. *Proceedings of the National Academy of Sciences*, 104(42):16504–16509, 2007.

[132] Pornthep Sompornpisut, Yi-Shiuan Liu, and Eduardo Perozo. Structure of the KcsA channel intracellular gate in the open state. *Nature Structural Biology*, 8:883–887, 2001.

[133] Heinz-Jurgen Steinhoff and Wayne Hubbell. Calculation of electron paramagnetic resonance spectra from Brownian dynamics trajectories: Application to nitroxide side chains in proteins. *Biophysical Journal*, 71:2201–2212, 1996.

[134] Ileana Stoica. Using molecular dynamics to simulate ESR spectra of T4 Lysozyme. *Journal of Physical Chemistry B*, 108:1771–1782, 2004.

[135] William C. Swope, Jed W. Pitera, and Frank Suits. Describing protein folding kinetics by molecular dynamics simulations. 1. Theory. *Journal of Physical Chemistry B*, 108:6571–6581, 2004.

[136] William C. Swope, Jed W. Pitera, Frank Suits, Mike Pitman, Maria Eleftheriou, Blake G. Fitch, Robert S. Germain, Aleksandr Rayshubski, T. J. C. Ward, Yuriy Zhestkov, and Ruhong Zhou. Describing protein folding kinetics by molecular dynamics simulations. 2. Example applications to alanine dipeptide and a β-hairpin peptide. *Journal of Physical Chemistry B*, 108:6582–6594, 2004.

[137] Fabio Tombolato, Alberta Ferrarini, and Jack H. Freed. Dynamics of nitroxide side chain in spin-labeled proteins. *Journal of Physical Chemistry B*, 110:26248–26259, 2006.

[138] Fabio Tombolato, Alberta Ferrarini, and Jack H. Freed. Modeling the effects of structure and dynamics of the nitroxide side chain on the ESR spectra of spin-labeled proteins. *Journal of Physical Chemistry B*, 110:26260–26271, 2006.

[139] Natalia Usova, Per-Olof Westlund, and Igor Fedchenia. Direct simulation of slow-motion electron spin resonance spectra by solving the stochastic Liouville equation in time domain with stochastic dynamics in the form of trajectories. *Journal of Chemical Physics*, 103:96–103, 1995.

[140] Stijn van Dongen. *Graph Clustering by Flow Simulation*. PhD thesis, University of Utrecht, 2000.

[141] N. G. Van Kampen. Elimination of fast variables. *Physics Reports*, 124:69–160, 1985.

[142] Eric Vanden-Eijnden. Numerical techniques for multi-scale dynamical systems with stochastic effects. *Communications in Mathematical Sciences*, 1:385–391, 2003.

[143] L. Venkataramanan and F. J. Sigworth. Applying Hidden Markov Models to the Analysis of Single Ion Channel Activity. *Biophysical Journal*, 82(4):1930–1942, 2002.

[144] Daniel Wallach. Effect of internal rotation on angular correlation functions. *Journal of Chemical Physics*, 47:5258–5268, 1967.

[145] Marcus Weber. Improved Perron cluster analysis. Technical report, Konrad-Zuse-Zentrum für Informationstechnik Berlin, April 2003.

[146] R. J. Wittebort and Attila Szabo. Theory of NMR relaxation in macromolecules: Restricted diffusion and jump models for multiple internal rotations in amino acid side chains. *Journal of Chemical Physics*, 69:1722–1736, 1978.

[147] R. J. Wittebort, Attila Szabo, and Frank R. N. Gurd. Rotational motions of side chains of poly-L-lysine. *Journal of the American Chemical Society*, 102:5723–5728, 1980.

[148] In-Chul Yeh and Gerhard Hummer. Diffusion and electrophoretic mobility of single-stranded RNA from molecular dynamics simulations. *Biophysical Journal*, 86:681–689, 2004.

[149] Z. Zhang, D. Tipikin, M. R. Fleissner, W. L. Hubbell, and Jack H. Freed. to be published.